MULTIFUNCTIONAL NANOPLATFORMS FOR BIOMEDICAL IMAGING AND PHOTODYNAMIC THERAPY

By

Hyung Ki Yoon

A dissertation submitted in partial fulfillment
of the requirements for the degree of
Doctor of Philosophy
(Chemistry)
in The University of Michigan
2014

Doctoral Committee:

Professor Raoul Kopelman, Chair
Associate Professor Jinsang Kim
Associate Professor Mi Hee Lim, Ulsan National Institute of Science and Technology
Professor Adam J. Matzger

To my lovely family and friends

ACKNOWLEDGMENTS

animal test. Our previous group members, Dr. Teayuana Curry and Dr. Ron Smith also guided me as senior graduate students when I first joined the Kopelman lab. Because of my Korean brothers, Byungchul Kim and Janghyun Lee, I was not lonely at all and it was really lucky that I was able to share all of the happiness and sadness with them. Also, I want to say "thank you" to the undergraduates under my supervision, Heeju Ryu and Wyatt Kuhlman, who worked with me in the lab for a long time.

It was my great fortune to meet such wonderful collaborators for several projects. Professor Euisik Yoon in the electrical engineering and computer science department and his group members, Dr. Xia Lou and Yu-Chih Chen, enabled me to start research regarding a microfluidic chip and their wonderful and fast progress let me finish my second project. Additionally, collaborators Professor Jérôme Kalifa and M.D. Uma Avula let me experience a new research field; they were also really good teachers of biomedical science.

Last, I want to express my heartfelt gratitude to my lovely parents. In Korea, they have always believed and supported me even when I experienced a slump. Furthermore, it was heartening to have the support of sisters, brothers in law and pretty nieces, Jooeun and Seoeun.

I have no doubt that I am a lucky guy to join the Kopelman group and have a relationship with such unforgettable people during my fantastic Ph.D. voyage, and thanks again to everyone.

TABLE OF CONTENTS

LIST OF FIGURES

LIST OF TABLES

ABSTRACT

Nanoplatforms have considerable potential for delivery of biomedical agents, so as to overcome inherent limitations of small molecule drugs or contrast agents, such as fast degradation, aggregation and lack of targeting ability. In this dissertation, we demonstrate improved imaging and therapy techniques using polyacrylamide (PAA) based nanoparticles (NPs) and star-shaped polyethylene glycol (PEG) platforms for cancer and cardiac arrhythmia treatment. The proposed albumin conjugated PAA NPs provided strong fluorescence and photoacoustic intensities for the Indocyanine Green (ICG) contrast agent for use in cancer imaging. These protein hybrid NPs not only enhanced the chemical stability of ICG but also showed *in vitro* cancer cell specificity, with the help of targeting moieties. We also developed methylene blue (MB) conjugated PAA NPs for photodynamic therapy (PDT). Its reactive oxygen species (ROS) productivity was enhanced by utilizing longer cross-linker than in previous PAA NPs and a newly designed microfluidic device contributes to faster tests on the cell killing efficacy of photo-drug NPs. Lastly, Chlorin e6 (Ce6) and cardiac targeting peptide (CTP) were conjugated to 8-arm PEG for extremely small sized nanoplatforms (CTP–Ce6–PEG); it showed great potential for treating cardiac arrhythmia by PDT, demonstrating selective ablation of arrhythmia causing myocyte cells. Overall, this dissertation, reporting on biomedical imaging and therapy based on nanotechnology, shows their potentialities towards further modifications for clinical usage and commercialization, not only for cancer but also for heart disease.

CHAPTER 1
INTRODUCTION

1.1 Nanoplatforms for Biomedical Applications

Heart disease and cancer are the first and second most common causes of death in the United States. [1] To save the lives of patients, accurate diagnosis, based on suitable analyzing methods, and corresponding appropriate treatments are required. Every year, new drugs and detection methods are developed to manage these diseases, but many people are still afflicted. For better analysis and treatment of diseases, many biomedical scientists seek to improve the precision of drug delivery, targeting specific areas and precise time. [2] Nanotechnology (an interdisciplinary research regarding fabrication of nano-scaled substances, based on chemistry, physics, biology, medicine, engineering, etc.) has recently been extensively utilized to develop purposeful designs of nano-sized platforms (nanoplatforms) for the precise delivery of biomedical agents. [3,4] The nanoplatform is a nano-sized particle, supramolecule, or combination thereof, that delivers drugs, contrast agents or itself as a therapeutic/imaging agent to a targeted biological domain. It may have a variety of shapes, as long as all dimensions are at least in the nanometer size. Until now, the nanoplatforms, such as organic nanoparticles (NPs), inorganic NPs, and single-walled carbon nanotubes (SWNTs), etc., have been studied so as to enhance efficiency, efficacy, sensitivity and selectivity for diagnostic, sensing, imaging and therapeutic applications, especially in the case of cancer. [5-7]

To be a successful nanoplatform for biomedical applications, there are several specific requirements. [8] First, the size of the nanoplatform should be adjustable, depending on the purpose and targeted organ. Second, the surface of the nanoplatform should be versatile enough to modify drugs or imaging contrast agents with targeting moieties for selective targeting. Third, the nanoplatform should be able to be easily controlled with regard to both the initial drug loading amount and the subsequent release rate of the loaded drug into the target area. Fourth, the nanoplatforms must be nontoxic and biocompatible in order to decrease potential side effects and increase tolerance for varying dosages of the drug. Lastly, the synthetic method of preparation should be simple and amenable for mass production with good quality control and low cost.

During the last two decades, the Kopelman group has investigated mainly two different types of nanoplatforms, including polyacrylamide (PAA) hydrogel NPs, silica/organically modified silica (Ormosil) NPs which are a frequently used as promising nanoplatforms for biomedical sensing, imaging and therapeutic purposes. [9-16] PAA NPs are nano-sized 3-dimensionally cross-linked polyacrylamide networks containing a large amount of water and are synthesized by the reverse micelle polymerization of an acrylamide monomer with other functional monomers and cross-linkers. [8] During the radical polymerization, the acrylamide, other monomers and cross-linkers are polymerized by a water soluble initiator. The size of these NPs is determined by the size of the micelle (water-in-oil). The appropriate kind and amount of biocompatible surfactant mixture (Brij 30 and AOT), which have both hydrophilic and hydrophobic groups at each end of the molecular chain, form a nano-sized aqueous micelle structure in the hexane solvent. [8,17] While acrylamide is known as a cariogenic chemical,

following polymerization, the polyacrylamide is not toxic anymore, and non-polymerized acrylamides are washed out with surfactants during multiple washing steps. [15,18] The PAA NPs are very versatile and can be easily engineered to meet various purposes of the application. For example, through copolymerization with a pH or temperature sensitive monomer, the swelling ratio of the NPs is optimized for specific pH and temperature conditions; also the degradation rate of the NPs can be controlled using a biodegradable cross-linker. [8,19,20] Furthermore, the PAA NPs can be modified with various drugs or dyes through three facile modification methods: a) pre-conjugation, b) encapsulation and c) post-loading or post-conjugation (Scheme 1-1). Due to their above advantages, the PAA NPs have been used for many purposes, for example, for intracellular calcium ion or oxygen chemical sensing, as chemo-drug delivery carriers for ovarian cancer and as hydrophobic photosensitizer delivery carriers for photodynamic therapy (PDT), and for tumor delineation applications. [10-14,21]
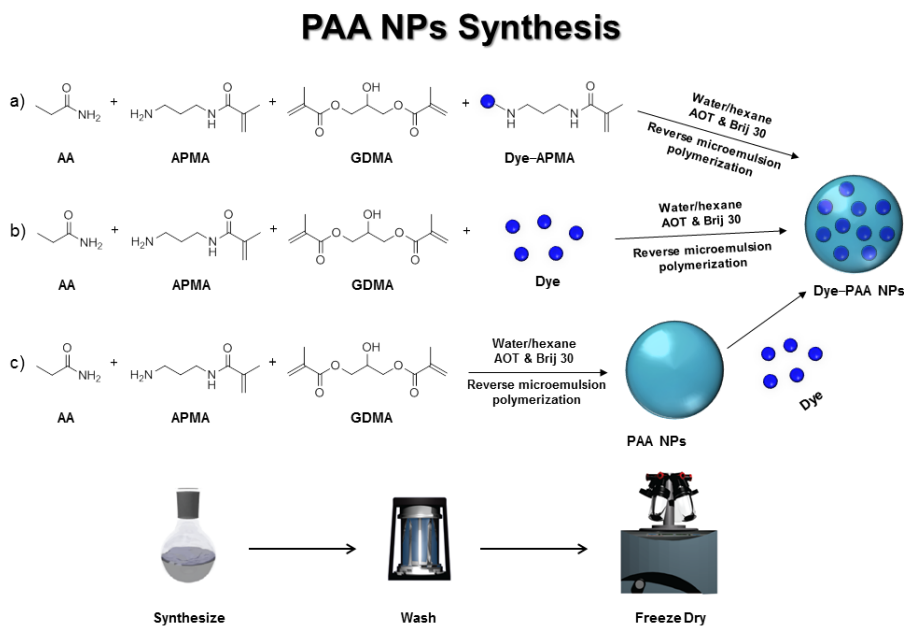
Scheme 1-1 Synthetic schemes of PAA NPs modifications.

3

Silica/ormosil NPs are the nanoplatform synthesized by organic functionalized silane, based on the sol-gel process. In contrast with traditional silica NPs, the ormosil NPs are synthesized in two steps: 1) hydrolysis of organic modified silane and 2) condensation of the silane. [22,23] The hydrophobic precursor, phenyhltrimethoxysilane (PTMS), is hydrolyzed under acidic conditions and then forms a 3-dimentional network for the NPs by condensation under basic conditions. [12,22] The size of ormosil NPs ranges from 300 – 800 nm but this size could be adjusted by control of the hydrolysis time and the concentration of PTMS. After such adjustment, the size of ormosil NPs was 100 – 800 nm, which is an appropriate size for use as an intracellular nanosensor. [23] The ormosil is hydrophobic, thus the NPs are poorly dispersed in aqueous media. Through surface modifications of ormosil NPs, coating with a relatively less hydrophobic precursor, methyltrimethyoxy silane (MTMS), helps to increase the suspension of ormosil NPs. Furthermore, using amine functionalized (3-aminopropyl)trimethoxysilane (APTMS), provides primary amines, which enables further modification with drugs, dyes or targeting moieties. [12] A subshell coating helps to load hydrophobic dyes inside the ormosil NPs without interference with the initial particle formation by adding the dye before the MTMS condensation. [23] In addition to hydrophobic dyes, hydrophilic dyes can be easily loaded into ormosil NPs by adding an initial acidic reaction mixture. Silica/ormosil NP is inert and biocompatible (but not biodegradable), thus this NP has been successfully used as nanocarrier to deliver a hydrophobic photosensitizer (PS) including, 2-(1-hexyloxyethyl)-2-devinyl pyropheophorbide-alpha (HPPH), meta-tetra(hydroxyphenyl)chlorin (mTHPC) and Methylene Blue (MB), or the contrast agent, Indocyanine Green (ICG) dye for photoacoustic imaging. [12,24-26] Furthermore, it has

been used as a nanosensor platform for Photonic Explorers for Biomedical uses with Biologically Localized Embedding (PEBBLE) nanosensor platforms, for the highly selective sensing of ions, hydrogen peroxide or for real-time measurement of O_2 in live cells. [23,27-29]

Kopelman group has also researched extremely small sized polymer nanoplatforms, in addition to their work on 3-dimentionally cross-linked PAA and silica/ormosil NPs. Most drug delivery NPs are optimized for cancer therapy, but sometimes it is necessary to deliver the drug to a normal organ which has a much smaller penetration widow than cancer tissue. [30] Thus, a very small sized ($\leq$ 10 nm) polymer nanoplatform can be more useful than conventional cross-linked sphere shape NPs to specific organ, such as heart. Among the biocompatible materials for polymer nanoplatform, polyethylene glycol (PEG) is one of the promising polymers for biomedical applications. [31] The FDA approved standard PEG compound is a non-ionic hydrophilic polymer with a structure of "HO–$(CH_2–CH_2–O)_n$–H" and was commercialized already 20 years ago. [32-34] PEG is frequently used in biomedical applications, especially as a drug delivery system, since it has low toxicity and helps to prevent biofouling, enhances plasma circulation time, reduces aggregation of drugs, proteins or NPs, and increases the solubility of hydrophobic drugs in the physiological medium. [32,34-36] Also, there are several functionalized and specially shaped PEG polymers, making possible further modifications, depending on the purpose/use. [37,38] Such drug loaded PEG polymers have been used for chromic hepatitis C, febril neutropenia, acromegaly and several cancer forms, including myeloma. [34]

There are several other promising, frequently used, nanoplatforms studied in other groups for biomedical applications, such as gold NPs, natural polymers and single-walled carbon nanotubes (SWNTs). The gold NPs, which are nano-sized, sphere shapes of gold, are used as immunostaining, single particle tracking, contrast agents for X-rays or photoacoustic imaing, and as a photo-drug for photothermal therapy (PTT), through easy modification of its surface by conjugation with thiol group fucntionalized drugs or targeting moieties. [39,40] The natual polymers are mainly classified as protein/polypeptides (e.g. collagen, gelatin, albumin, polylysine, elastin-like polypepetide (ELP)) and polysaccharides. The polysaccharides are further categorized as anionic (alginate, hyaluroanan), cationic (chitosan) and neutral (pullulan, agarose, dextran, cellulose) polymers. [8] These natural polymers are inherently biodegradable under bio-enzymatic conditions and have abundant functional groups (-OH, -NH$_2$, and -COOH) for modification with drug, dye or targeting moieties towards drug delivery or other therapeutic purposes. The SWNTs are nano-sized SP$_2$ hybridized carbon materials, frequenlty used as Raman and photoacoustic imaging contrast agent or as a delivery system for drugs, genes, and small molecules, due to its unique physical properties. [3,41,42] In addition to the above mentioned nanoplatforms, dendrimers, magnetic NPs, quauntum dots, and liposomes are frequenlty studied as carriers for biomedical imaging and therapeutic purposes. [3,4,43]

1.2 Biomedical Optical Imaging with Nanoplatforms

The lack of a suitable biomedical analyzing technique made it difficult to diagnose diseases appropriately. Detecting and diagnosing disease at an early stage is very critical because it increases the likelihood of success of any therapy. [3,5] The biomedical

imaging technology plays a very important role in accurate diagnosis using cellular and molecular level visualization. [4,5] There are several biomedical imaging modalities, such as magnetic resonance (MR), single photon emission computed tomography (SPECT), ultrasound (US), computed tomography (CT), positron emission tomography (PET), single photon emission computed tomography (SPECT) and optical imaging. [6] Among these, optical imaging technology has been the focus, due to its versatility, low cost, low hazard, and its high spatial resolution and sensitivity; examples include fluorescence, Raman and photoacoustic imaging, and optical coherence tomography (OCT). [4,5,44,45]

Fluorescence imaging (FI) is one of the frequently used optical imaging modalities that enable both *in vitro* and *in vivo* level analysis for several diseases (*e.g.* hepatic excretory function, uterine blood flow, lymph nodes in breast cancer, atherosclerotic plaques, and retinal angiography). [46-52] The fluorescence imaging technique has the following advantages; 1) high signal to noise ratio (SNR); 2) simplicity, 3) high sensitivity, 4) ease of operation, 5) fast imaging speed, 6) capability to provide molecular level information, 7) low cost. [46] FI is based on the emission light of the image contrast agents, fluorophores. The ground state of the fluorophore is excited by absorbing light energy (photons) transition to an excited state (in femtoseconds) and then returns to the ground state by emitting fluorescence light (in nanoseconds). [53] This fluorescence emission is usually at a longer wavelength compared to absorption, so the exciting light can be filtered perfectly without interfering with the emission light. The fluorescence optical imaging technique has great sensitivity and selectivity for *in vitro* study but has limitations for *in vivo* study, due to autofluorescence from the living tissue and light

7

attenuation. [5] As advanced techniques for *in vivo* fluorescence microscopy, several new microscope modalities are emerging, such as intravital confocal, two-photon, and multi-photon microscopies, which enable better resolution and light penetration depth. [44]

In company with fluorescence imaging, photoacoustic imaging (sometimes called optoacoustic or thermoacoustic imaging) is also a promising noninvasive optical imaging modality for human organs like breast or brain, due to its combination of light and ultrasound use advantages. [3,54-56] In the photoacoustic phenomenon, the acoustic waves are created by the instantaneous thermal-elastic expansion in the tissues because the absorbed light energy is converted into heat. [54,57,58] Due to the combination of light and ultrasound, the photoacoustic imaging modality has fine spatial resolution combined with good depth of imaging, because of the weak scattering of ultrasonic waves in living tissue. It also has high contrast in tissue, due to strongly optical absorbing contrast agents. [56] For the high penetration depth, longer optical waves, especially in the near-infrared (NIR) range (700 – 900 nm), are used in photoacoustic imaging, so as to avoid light absorption by hemoglobin in the blood (400 – 600 nm) and by water ($\geq$ 900 nm). [54,56,59] Thus, the contrast dye with high absorbance at a proper NIR frequency used, such as the Indocyanine Green (ICG) and Coomassie Blue, are usually used. [55,59]

However, most of the image contrast agents have their own limitations, such as fast degradation, aggregation, toxicity and lack of targeting. [60,61] For enhanced sensitivity and selectivity of the optical imaging quality *in vivo,* as well as *in vitro,* nanotechnology has been applied to these optical imaging techniques. For instance, fluorescence dye doped functionalized silica NPs increase the sensitivity by amplifying the optical signal and also enhance the stability by preventing photobleaching and photodegradation. [62]

8

Quantum Dots which are fluorescence semiconductor nanocrystals have advantages over free dye due to higher quantum yield, higher chemical stability, and long fluorescence life time with narrow fluorescence emission spectra. [63-65] In addition, gold NPs and SWNTs are good contrast agents for photoacoustic imaging; also targeting moiety (RGD) loaded SWNT (SWNT–RGD) increase the selectivity of the photoacoustic signal. [5,66]

The multipurpose designed nanoplatform (multifunctional nanoplatform) allows for multimodal biomedical imaging by a combination of several imaging techniques. [6,67] Because of the heterogeneity of diseases and patient, one imaging technique provides limited information but a hybrid of several imaging modalities helps to make a more accurate diagnosis. [3,6] Furthermore, due to the advantages of carrying various imaging contrast agents and chemo-drugs simultaneously, the multifunctional nanoplatforms are also used for a theranostic (therapeutics + diagnostics) purpose, which enables both diagnosing and treating the disease at the same time. [3,4,68]

1.3 Photodynamic Therapy (PDT) with Nanoplatforms

The biomedical applications of nanoplatforms are not limited to diagnostics, but can be extended to the treatment of diseases. Among the treatment methods, there have occurred in history a lot of efforts to apply the properties of light to therapeutic purposes dating back for thousands of years ago. [69] Ancient people in Egypt, China and India cured psoriasis, rickets and skin cancer and in the 19th century, Finsen used red light and ultraviolet (UV) light to treat smallpox pustules and cutaneous tuberculosis. [69] Nowadays, PDT is an FDA approved therapeutic modality used to treat various localized diseases (cancer, cardiovascular, ophthalmic, dermatological and dental diseases) due to the following advantages: 1) minimal long-term toxicity effects, precise localized

treatment, ability of repeated treatment at the same site, and suitability for patients too old or sick for conventional surgery. [24,70,71]

PDT is achieved by the combination of three important components: photosensitizer, O_2 and appropriate light source. [24,72] The photosensitizer is a light sensitive molecule that absorbs a specific wavelength of light and this absorbed light energy activates the photosensitizer. [69] Following absorption of the light (photon) energy, the photosensitizer is excited from the ground state to an excited singlet state (life time = 10^{-9} – 10^{-6} s). Then, the photosensitizer emits the photon as light energy returning to the ground state (fluorescence) or transforms to an excited triplet state, which has a much longer life time (10^{-3} – 10 s) through intersystem crossing. [73] Through two different pathways, the excited triplet state PS can produce several highly oxidative molecules and radicals called reactive oxygen species (ROS): (1) The excited triplet state PS reacts with substrates like cell membrane or other molecules to directly produce radicals or radical ions through electron and hydrogen transfer (Type I). (2) The excited triplet state PS transfers its energy to a ground triplet state O_2 molecule, producing the highly reactive singlet oxygen ($^1O_2$) (type II) (Scheme 1-2). [24,69,74,75] These two different types of ROS production occur at the same time, and the ratio of type I and type II depends on the type of PS and the environmental condition, such as the concentration of O_2 or substrate. Because of their high reactivity, ROS not only function as physiological regulators of intercellular signal pathways but are also cytotoxic, whereby they induce cell death, either by apoptosis or necrosis, through oxidation. [74,76-78] However, the PDT effect is very limited in range and localized to the PS loaded and/or light illuminated area. This is true for the commonly utilized Type II PDT since the life time of the singlet oxygen in *in*

vivo is around 0.03 – 0.18 µs and the diffusion distance is 11 – 27 nm. [24,69] Similarly, in Type I PDT, the life time of the free radicals is also short (≤ 1 ms), as is their diffusion distance. [79]
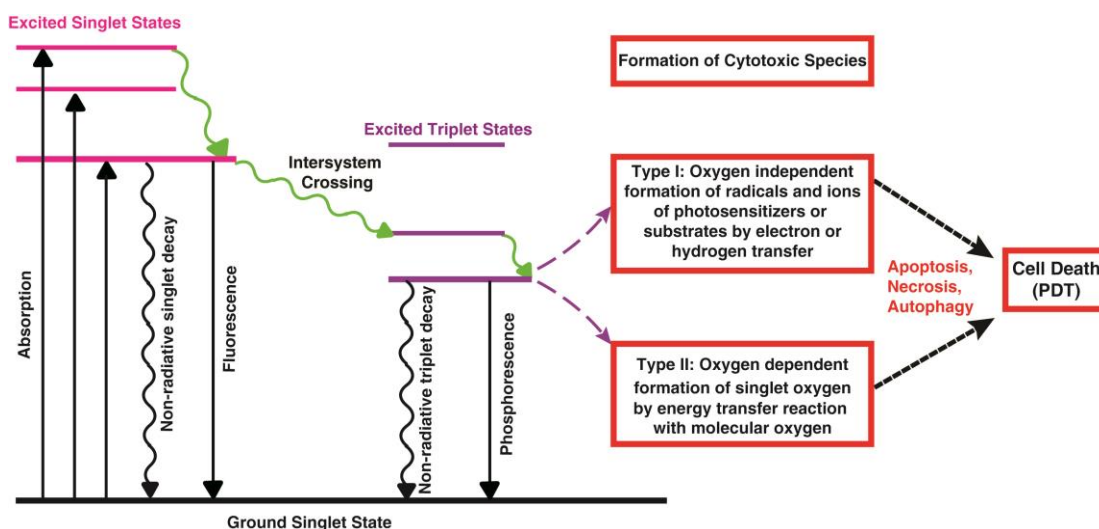
Scheme 1-2 Reaction kinetics of photosensitizaton leading to PDT (Types I and II). [24]

There are several already developed and approved PSs (Table 1-1), which are designed based on the following factors: [69,73]

1) Strong absorption in near infrared (NIR) range (600 – 850 nm) with a high extinction coefficient;

2) High quantum yield of triplet formation to generate ROS;

3) Negligible cytotoxicity in absence of light (low dark toxicity);

4) Higher targetability in diseased area;

5) Rapid clearance (excretion) from body after PDT, to avoid prolonged photosensitivity;

6) Single and well characterized stable compound with high-yield synthetic route;

7) High solubility in biological media;

Table 1-1 Type of cancer and approved drugs (2003). [69]

Disease	Drug	Country
Pre-cancer		
Actinic Keratosis	Levulan, Metvix	EU
Barrett's oesophagus	Photofrin	EU, USA
Cevical dysplasia	Photofrin	Japan
Cancer		
Basal-cell Carcinoma	Metvix	EU
Cervical cancer	Photofrin	Japan
Endobroncheal cancer	Photofrin	Canada, Denmark, Finland, France, Germany, Ireland, Japan, The Netherlands, UK, USA
Oesophageal cancer	Photofrin	Canada, Denmark, Finland, France, Ireland, Japan, The Netherlands, UK, USA
Gastric cancer	Photofrin	Japan
Head and neck cancer	Foscan	EU
Papillary bladder cancer	Photofrin	Canada

Photodynamic therapy has also been undertaken in other countries with haematoporphyrin derivative and porphtin mixtures (China and India), and phthalocyanines (Russia and India). EU, European Union; UK, United Kingom; USA, The United States.

However, these PS do not perfectly satisfy all the above criteria. For example, the most common PS, Photofrin®, is not an ultimate PS due to its rapid photobleaching, long term skin phososensitivity, difficulty of chemical modification and being a mixture of dimers or oligomers. [73] Thus, there are many efforts to develop a new PS or to use a nanocarrier to better satisfy the above criteria, in the interest of increasing PDT efficacy and decreasing inherent limitations of PDT. Because of superiority of NP agents, there are already many PS mediated NPs, based on PAA, Poly (D,L-lactide-co-glycolide) (PLGA), ormosil, dendrimer and natural polymers for cancer. [24] The relatively hydrophilic nanocarriers, compared to hydrophobic PDT drugs, encapsulate the PS inside the platform and increase drug solubility. [24] To avoid unwanted cytotoxicity of

different organs and maximize efficiency of treatment, PDT drug loaded nanoplatforms are modified with a targeting moiety specific to a cancer cell line. [15,80] Also, the nanoplatform protects PDT drugs from bio-enzymes in the blood-stream and increases targeting efficiency by adding targeting peptides onto the NP surface. [80,81] These efficient PDT drug loaded nanoplatforms may eventually be applied to other diseases than cancer, such as heart arrhythmia. [82]

1.4 Overview of Dissertation

In this dissertation, engineering of nanoplatforms, PAA NPs and 8-armed PEG, is reported for optical imaging purposes and for use in PDT of cancer and cardiac arrhythmia diseases. For treating cancer, a correct diagnosis should, ideally, always precede the selection of appropriate treatment. Thus, we first focus our efforts to detect the disease by improved optical imaging contrast agents. In Chapter 2, it was attempted to prepare NPs which enable not only enhancement of the chemical stability of the contrast agent, based on the advantages of human serum albumin (HSA), but also on operating multifunctional imaging techniques. HSA conjugated PAA NPs were used to deliver a contrast agent, the FDA approved ICG, with enhanced thermal- and photo-stability. After optimizing the ICG loading, these NPs were tested for their photoacoustic signal intensity at varied wavelengths and modified with F3 targeting moieties to provide selective fluorescence intensity in different cancer cell lines.

In the next step towards managing cancer, research on cancer treatment is carried out. Among the therapeutic methods, in Chapter 3, we focus on PDT as a therapeutic modality, so as to remove the tumor without traditional surgery. As a new photo-drug, MB conjugated PAA NPs were prepared with a longer cross-linker, poly(ethylene glycol)

dimethacrylate (PEGDMA, M_n = 550) in order to overcome previously reported limitations. [15] Furthermore, their ROS productivity was analyzed and qualified by utilizing two different dyes, anthracence-9,10-dipropionic acid (ADPA) and Singlet Oxygen Sensor Green (SOSG). With the help of a new microfluidic device, a new PDT efficacy test is introduced which is capable of simultaneous testing of several NP samples under identical conditions.

In Chapter 4, we demonstrate a new approach of using PDT to treat cardiac arrhythmia. Up to date, cardiac arrhythmia is usually treated by anti-arrhythmic drugs, surgery and/or catheter ablation, methods which carry a high risk of surgical complications, unwanted cellular damage or serious drug side effects. [82] Thus, it was planned to selectively ablate only myocytes, the cells which cause arrhythmia, by using a targeted and photosensitizer embedded nanopatform. For an *in vivo* experiments, an extremely small sized nanoplatform, 8-armed polytheylene glycol (8-arm PEG) was conjugated with the photosensitizer Chlorin e6 (Ce6) and the cardiac targeting peptide (CTP) to provide new nanoplatform (CTP–Ce6–PEG) due to the limited size of the cardiac capillary vessels' fenestrations (pores), which is much smaller than for cancer. The new photo-drug, CTP–Ce6–PEG, was used to demonstrate selective myocyte killing by *in vitro* PDT as well as to explore *in vivo* targeting ability leading to selective cardiac ablation for arrhythmia using PDT ablation in the live heart of a rat.

Lastly, in Chapter 5, a summary of the thesis is given with a discussion of future directions for each project, including 1) *in vivo* toxicity test on the nanoplatform, 2) theranostic modification of the nanoplatform, and 3) a new type of photosensitizer–nanoplatform for cardiac ablation with rapid bioelimination.

1.5 References

(1)   Murphy, S. L.; Xu, J.; Kochanek, K. D. *National vital statistics reports : from the Centers for Disease Control and Prevention, National Center for Health Statistics, National Vital Statistics System* **2013**, *61*, 1.

(2)   Mishra, B.; Patel, B. B.; Tiwari, S. *Nanomed. Nanotechnol.* **2010**, *6*, 9.

(3)   Choi, K. Y.; Liu, G.; Lee, S.; Chen, X. *Nanoscale* **2012**, *4*, 330

(4)   Cai, W.; Chen, X. *Small* **2007**, *3*, 1840.

(5)   Bao, G.; Mitragotri, S.; Tong, S. *Annu. Rev. Biomed. Eng.* **2013**, *15*, 253.

(6)   Lee, D. E.; Koo, H.; Sun, I. C.; Ryu, J. H.; Kim, K.; Kwon, I. C. *Chem. Soc. Rev.* **2012**, *41*, 2656.

(7)   Wang, A. Z.; Langer, R.; Farokhzad, O. C. *Annu. Rev. Med.* **2012**, *63*, 185.

(8)   Koo Lee, Y.E.; Kopelman, R. *Multifunctional Nanoparticles for Drug Delivery Applications: Imaging, Targeting, and Delivery*; Nanostruture Science and Technology; Springer, 2012, P225.

(9)   Buck, S. M.; Xu, H.; Brasuel, M.; Philbert, M. A.; Kopelman, R. *Talanta* **2004**, *63*, 41.

(10)   Si, D.; Epstein, T.; Lee, Y. E.; Kopelman, R. *Anal. Chem.* **2012**, *84*, 978.

(11)   Koo Lee, Y. E.; Ulbrich, E. E.; Kim, G.; Hah, H.; Strollo, C.; Fan, W.; Gurjar, R.; Koo, S.; Kopelman, R. *Anal. Chem.* **2010**, *82*, 8446.

(12)   Kim, G.; Huang, S. W.; Day, K. C.; O'Donnell, M.; Agayan, R. R.; Day, M. A.; Kopelman, R.; Ashkenazi, S. *J. Biomed. Opt.* **2007**, *12*, 044020.

(13)   Gupta, A.; Wang, S.; Pera, P.; Rao, K. V.; Patel, N.; Ohulchanskyy, T. Y.; Missert, J.; Morgan, J.; Koo-Lee, Y. E.; Kopelman, R.; Pandey, R. K. *Nanomedicine* **2012**, *8*, 941.

(14)   Winer, I.; Wang, S.; Lee, Y. E.; Fan, W.; Gong, Y.; Burgos-Ojeda, D.; Spahlinger, G.; Kopelman, R.; Buckanovich, R. J. *Cancer Res.* **2010**, *70*, 8674.

(15)   Hah, H. J.; Kim, G.; Lee, Y. E.; Orringer, D. A.; Sagher, O.; Philbert, M. A.; Kopelman, R. *Macromol. Biosci.* **2011**, *11*, 90.

(16)   Curry, T.; Epstein, T.; Smith, R.; Kopelman, R. *Nanomedicine* **2013**, *8*, 1577.

(17)   Daubresse, C.; Grandfils, C.; Jerome, R.; Teyssie, P. *J. Colloid Interface Sci.* **1994**, *168*, 222.

(18)   Caulfield, M. J.; Qiao, G. G.; Solomon, D. H. *Chem. Rev.* **2002**, *102*, 3067.

(19)   Kulkarni, R. V.; Sa, B. *Drug Dev. Ind. Pharm.* **2008**, *34*, 1406.

(20)   Owens, D. E.; Jian, Y.; Fang, J. E.; Slaughter, B. V.; Chen, Y.-H.; Peppas, N. A. *Macromolecules* **2007**, *40*, 7306.

(21)   Orringer, D. A.; Koo, Y. E.; Chen, T.; Kim, G.; Hah, H. J.; Xu, H.; Wang, S.; Keep, R.; Philbert, M. A.; Kopelman, R.; Sagher, O. *Neurosurgery* **2009**, *64*, 965.

(22)   Hah, H. J.; Um, J. I.; Han, S. H.; Koo, S. M. *Chem. Commun.* **2004**, 1012.

(23)   Koo Lee, Y. E.; Cao, Y.; Kopelman, R.; Koo, S. M.; Brasuel, M.; Philbert, M. A. *Anal. Chem.* **2004**, *76*, 2498.

(24)   Koo Lee, Y. E.; Kopelman, R. *Biomedical Nanoetechnology: Methods and Protocols*; Methods in Molecular Biology Series; Springer: New York, 2011, Vol. *726*, p151.

(25)   Kim, S.; Ohulchanskyy, T. Y.; Bharali, D.; Chen, Y.; Pandey, R. K.; Prasad, P. N. *J. Phys. Chem. C, Nanomater. Interfaces* **2009**, *113*, 12641.

(26)   Compagnin, C.; Bau, L.; Mognato, M.; Celotti, L.; Miotto, G.; Arduini, M.; Moret, F.; Fede, C.; Selvestrel, F.; Rio Echevarria, I. M.; Mancin, F.; Reddi, E. *Nanotechnology* **2009**, *20*, 345101.

(27)   Buck, S. M.; Koo, Y. E. L.; Park, E.; Xu, H.; Philbert, M. A.; Brasuel, M. A.; Kopelman, R. *Curr. Opin. Chem. Biol.* **2004**, *8*, 540.

(28)   Kim, G.; Lee, Y. E.; Xu, H.; Philbert, M. A.; Kopelman, R. *Anal. Chem.* **2010**, *82*, 2165.

(29)   Kim, G.; Lee, Y. E.; Kopelman, R. *Methods Mol. Biol.* **2013**, *1028*, 101.

(30)   Gaumet, M.; Vargas, A.; Gurny, R.; Delie, F. *Eur. J. Pharm. Biopharm.* **2008**, *69*, 1.

(31)   Pasut, G.; Veronese, F. M. *J. Control. Release* **2012**, *161*, 461.

(32)   Pasut, G.; Veronese, F. M. *Adv. Drug Deliv. Rev.* **2009**, *61*, 1177.

(33)   Webster, R.; Elliott, V.; Park, B. K.; Walker, D.; Hankin, M.; Taupin, P. *Milestones Drug. Ther.* **2009**, 127.

(34)   Knop, K.; Hoogenboom, R.; Fischer, D.; Schubert, U. S. *Angew. Chem. Int. Ed.* **2010**, *49*, 6288.

(35)   Xu, Y. D.; Huang, W.; Ren, G.; Qi, S. B.; Jiang, H.; Miao, Z.; Liu, H. G.; Lucente, E.; Bu, L. H.; Shen, B. Z.; Barron, A.; Cheng, Z. *Acs Macro Lett.* **2012**, *1*, 753.

(36)   Shi, J.; Yu, X.; Wang, L.; Liu, Y.; Gao, J.; Zhang, J.; Ma, R.; Liu, R.; Zhang, Z. *Biomaterials* **2013**, *34*, 9666.

(37)   Bonora, G. M.; Drioli, S. *Milestones Drug Ther.* **2009**, 33.

(38)   Li, W.; Zhan, P.; De Clercq, E.; Lou, H.; Liu, X. *Prog. Polym. Sci.* **2013**, *38*, 421.

(39)   Das, M.; Shim, K.; An, S.; Yi, D. *Toxicol. Environ. Health Sci.* **2011**, *3*, 193.

(40)   Sperling, R. A.; Rivera gil, P.; Zhang, F.; Zanella, M.; Parak, W. J. *Chem. Soc. Rev.* **2008**, *37*, 1896.

(41)   Koh, B.; Kim, G.; Yoon, H. K.; Park, J. B.; Kopelman, R.; Cheng, W. *Langmuir* **2012**, *28*, 11676.

(42)   Liu, Z.; Cai, W.; He, L.; Nakayama, N.; Chen, K.; Sun, X.; Chen, X.; Dai, H. *Nat. Nanotechnol.* **2007**, *2*, 47.

(43)   Ochekpe, N. A.; Olorunfemi, P. O.; Ngwuluka, N. C. *Trop J. Pharm. Res.* **2009**, *8*, 275.

(44)   Ntziachristos, V. *Ann. Rev. Biomed. Eng* **2006**, *8*, 1.

(45)   Freudiger, C. W.; Min, W.; Saar, B. G.; Lu, S.; Holtom, G. R.; He, C.; Tsai, J. C.; Kang, J. X.; Xie, X. S. *Science* **2008**, *322*, 1857.

(46)   Alander, J. T.; Kaartinen, I.; Laakso, A.; Patila, T.; Spillmann, T.; Tuchin, V. V.; Venermo, M.; Valisuo, P. *Int. J. Biomed. Imaging* **2012**, *2012*, 940585.

(47)   Recknagel, P.; Claus, R. A.; Neugebauer, U.; Bauer, M.; Gonnert, F. A. *J. Biophotonics* **2012**, *5*, 571.

(48)   Kisu, I.; Banno, K.; Mihara, M.; Lin, L. Y.; Tsuji, K.; Yanokura, M.; Hara, H.; Araki, J.; Iida, T.; Abe, T.; Kouyama, K.; Suganuma, N.; Aoki, D. *PloS One* **2012**, *7*, e35124.

(49)   Kitai, T.; Inomoto, T.; Miwa, M.; Shikayama, T. *Breast cancer* **2005**, *12*, 211.

(50)   Vinegoni, C.; Botnaru, I.; Aikawa, E.; Calfon, M. A.; Iwamoto, Y.; Folco, E. J.; Ntziachristos, V.; Weissleder, R.; Libby, P.; Jaffer, F. A. *Sci. Transl. Med.* **2011**, *3*, 84ra45.

(51)   Fineman, M. S.; Maguire, J. I.; Fineman, S. W.; Benson, W. E. *Arch. Ophthalmol.* **2001**, *119*, 353.

(52)   Desmettre, T.; Devoisselle, J. M.; Mordon, S. *Surv. Ophthalmol.* **2000**, *45*, 15.

(53)   Lichtman, J. W.; Conchello, J. A. *Nat. Methods* **2005**, *2*, 910.

(54)   Ray, A.; Rajian, J. R.; Lee, Y. E.; Wang, X.; Kopelman, R. *J. Biomed. Opt.* **2012**, *17*, 057004.

(55)   Ray, A.; Wang, X. D.; Lee, Y. E. K.; Hah, H. J.; Kim, G.; Chen, T.; Orringer, D. A.; Sagher, O.; Liu, X. J.; Kopelman, R. *Nano Res.* **2011**, *4*, 1163.

(56)   Xu, M. H.; Wang, L. H. V. *Rev. Sci. Instrum.* **2006**, *77*.

(57)   Cox, B.; Laufer, J. G.; Arridge, S. R.; Beard, P. C. *J. Biomed. Opt.* **2012**, *17*, 061202.

(58)   Wang, L. V. *Nat. Photon.* **2009**, *3*, 503.

(59)   Zhang, Y.; Hong, H.; Cai, W. *Cold Spring Harb. Protoc.* **2011**, *2011*, pdb.top065508.

(60)   Kirchherr, A. K.; Briel, A.; Mader, K. *Mol. Pharmaceutics* **2009**, *6*, 480.

(61)   Engel, E.; Schraml, R.; Maisch, T.; Kobuch, K.; Konig, B.; Szeimies, R. M.; Hillenkamp, J.; Baumler, W.; Vasold, R. *Invest. Ophthalmol. Vis. Sci.* **2008**, *49*, 1777.

(62)   Wang, K.; He, X.; Yang, X.; Shi, H. *Acc. Chem. Res.* **2013**, *46*, 1367.

(63)   Alivisatos, P. *Nat. Biotechnol.* **2004**, *22*, 47.

(64)   Michalet, X.; Pinaud, F. F.; Bentolila, L. A.; Tsay, J. M.; Doose, S.; Li, J. J.; Sundaresan, G.; Wu, A. M.; Gambhir, S. S.; Weiss, S. *Science* **2005**, *307*, 538.

(65)   Medintz, I. L.; Uyeda, H. T.; Goldman, E. R.; Mattoussi, H. *Nat. Mater.* **2005**, *4*, 435.

(66)   De la Zerda, A.; Zavaleta, C.; Keren, S.; Vaithilingam, S.; Bodapati, S.; Liu, Z.; Levi, J.; Smith, B. R.; Ma, T. J.; Oralkan, O.; Cheng, Z.; Chen, X.; Dai, H.; Khuri-Yakub, B. T.; Gambhir, S. S. *Nat. Nanotechnol.* **2008**, *3*, 557.

(67)   Harrell, J. A.; Kopelman, R. *Biophotonics International* **2000**, *7*, 22.

(68)   Kopelman, R.; Lee Koo, Y.-E.; Philbert, M.; Moffat, B. A.; Ramachandra Reddy, G.; McConville, P.; Hall, D. E.; Chenevert, T. L.; Bhojani, M. S.; Buck, S. M.; Rehemtulla, A.; Ross, B. D. *J. Magn. Magn. Mater.* **2005**, *293*, 404.

(69)   Dolmans, D. E. J. G. J.; Fukumura, D.; Jain, R. K. *Nat. Rev. Cancer* **2003**, *3*, 380.

(70)   Tardivo, J. P.; Del Giglio, A.; de Oliveira, C. S.; Gabrielli, D. S.; Junqueira, H. C.; Tada, D. B.; Severino, D.; Turchiello, R. D. F.; Baptista, M. S. *Photodiagn. Photodyn.* **2005**, *2*, 175.

(71)   Mang, T. S. *Photodiagn. Photodyn.* **2004**, *1*, 43.

(72)   Mitton, D.; Ackroyd, R. *Photodiagn. Photodyn.* **2008**, *5*, 103.

(73)   Garland, M. J.; Cassidy, C. M.; Woolfson, D.; Donnelly, R. F. *Future Med. Chem.* **2009**, *1*, 667.

(74)   Buytaert, E.; Dewaele, M.; Agostinis, P. *Biochim. Biophys. Acta* **2007**, *1776*, 86.

(75)   Dougherty, T. J.; Gomer, C. J.; Henderson, B. W.; Jori, G.; Kessel, D.; Korbelik, M.; Moan, J.; Peng, Q. *J. Natl. Cancer Inst.* **1998**, *90*, 889.

(76)   Finkel, T. *J. Cell Biol.* **2011**, *194*, 7.

(77)   Theodossiou, T. A.; Hothersall, J. S.; De Witte, P. A.; Pantos, A.; Agostinis, P. *Mol. Pharm.* **2009**, *6*, 1775.

(78)   Robertson, C. A.; Evans, D. H.; Abrahamse, H. *J. Photochem. Photobiol. B* **2009**, *96*, 1.

(79)   Cruz de Carvalho, M. H. *Plant Signal. Behav.* **2008**, *3*, 156.

(80)   Qin, M.; Hah, H. J.; Kim, G.; Nie, G.; Lee, Y. E.; Kopelman, R. *Photochem. Photobiol. Sci.* **2011**, *10*, 832.

(81)   Tang, W.; Xu, H.; Park, E. J.; Philbert, M. A.; Kopelman, R. *Biochem. Bioph. Res. Commun.* **2008**, *369*, 579.

(82)   Avula, U. M.; Kim, G.; Lee, Y. E.; Morady, F.; Kopelman, R.; Kalifa, J. *Heart Rhythm* **2012**, *9*, 1504.

CHAPTER 2
POLYMER-PROTEIN HYDROGEL NANOMATRIX FOR STABILIZATION OF INDOCYANINE GREEN TOWARDS TARGETED FLUORESCENCE AND PHOTOACOUSTIC BIO-IMAGING

2.1 Introduction

Indocyanine Green (ICG) is a Food and Drug Administration (FDA) approved tricarbocyanine fluorescent dye; it is negatively charged and is extremely water soluble. [1-5] It has absorption and fluorescence maxima in the near-infrared (NIR) region, around 780 nm and 820 nm, respectively. [6-8] The use of NIR radiation facilitates deep tissue imaging *in vivo*, due to good penetration of the NIR photons. Moreover, biological tissues have significantly reduced autofluorescence in the NIR region, which also leads to a much better signal to noise ratio (SNR) as compared to visible radiation. [1,5]

ICG has been used as a contrast agent for fluorescence imaging (FI), which is one of the most commonly used medical imaging modalities, and is also a good contrast agent for the photoacoustic imaging (PI). [9-11]. Although ICG is one of the most widely used contrast agents for FI and PI, its applications have often been limited due to its intrinsic drawbacks, such as: 1) it does not have specificity towards the target tissue; 2) it aggregates to form dimers and oligomers, depending on the local dye concentration (dimers and oligomers at concentrations > 3.9 mg·L^{-1} and J - aggregates at concentrations

$> 10^3$ mg·L^{-1}), leading to a reduction in signal intensity; 3) the "naked" dye gets degraded under enzymatic *in vivo* conditions, by losing its carbon-carbon double bond in its conjugated chain, which results in the formation of a colorless leuko form; 4) in the blood circulatory system, ICG has a short circulation lifetime ($t_{1/2}$ = 2 - 4 min), as it is rapidly bioeliminated through the kidneys; and 5) ICG shows lower fluorescence intensity with increasing temperature, making it more difficult to obtain strong signals under *in vivo* conditions, compared to room temperature. [1,2,5,12-15]

Recently, diverse approaches have been utilized to overcome the above mentioned disadvantages of ICG as an imaging contrast agent. Metallic particles such as gold and silver colloids have been used to enhance the fluorescence and photo-stability of ICG, utilizing the metal enhanced fluorescence (MEF) effect, which occurs due to the presence of surface plasmons on the noble metal surface. [7,16] It was also reported that biocompatible nanocarriers such as phospholipid–polyethylene glycol (PL–PEG), poly(lactic–co–glycolic acid) (PLGA) and organic modified silica (Ormosil) nanostructures have been utilized for the purpose of increasing the thermal- and photo-stability of ICG in aqueous solutions. [12,14,17-19] In addition, specific targeting of ICG was accomplished by attaching targeting moieties to the surface of a carbon nanotube, acting as a nanocarrier, to increase the cellular uptake and obtain stronger contrast enhancement. [10,20]

Here, a new kind of polymer/protein hybrid nanoparticle – a polyacrylamide nanoparticle (PAA NP) incorporated with human serum albumin (HSA), decorated with tumor-specific peptide on the surface – was developed as a tumor-targeting nanocarrier of ICG. HSA (66.5 kDa and d = 7 nm), the most abundant protein present in human blood,

has a high affinity towards ICG through non-covalent bonding, resulting from electrostatic interactions, hydrophobic interactions and hydrogen bonding. [21-23] The PAA NPs have been shown to be promising nanoplatforms for *in vivo* applications, such as sensing and drug delivery, for both diagnosis and therapy, due to their excellent biomedical properties and engineerability, including high aqueous solubility, small size, nontoxicity, biodegradability and easy surface modification with PEG, for longer circulation times, as well as with targeting moieties, for high targeting efficiency. [24-29] In addition, the PAA nanomatrix efficiently protects the encapsulated chromophore from external interference. [30,31] Due to these advantages, it has already been shown that loading of PAA NPs that include ICG into brain tumor cells can be used for tumor delineation purposes. [32]

We incorporated HSA into the PAA NPs so as to help overcome the drawbacks of free ICG dye molecule, while maximizing biocompatibility by keeping all the *in vivo* advantages of the PAA nanoparticles listed above. We report on 1) the optimized loading parameters of ICG into HSA–PAA NPs, 2) minimizing perturbations on the chemical and physical properties of ICG (i.e. reduced chemical degradation, and increased thermal- or photo-stability), 3) the use of ICG–HSA–PAA NPs for photoacoustic response, and 4) the specific targeting capabilities of the NPs towards tumoric endothelial cells through fluorescence imaging.

2.2 Experimental Section

2.2.1 Materials

Materials. Indocyanine Green (ICG), acrylamide (AA), acrylic acid *N*-hydroxysuccinimide ester (NAS) (≥ 90%), glycerol dimeathacrylate, mixture of isomers (85%) (GDMA), ammonium persulfate (APS), *N,N,N',N'*- tetramethylethylenediamine (TEMED), sodium dioctylsulfosuccinate (AOT), Brij 30, dimethyl sulfoxide (DMSO), L-cysteine, and 3-(4,5-dimethylthiazolyl-2)-2,5-diphenyltetrazolium bromide (MTT agent), Phosphate buffered saline (BioReagent, pH 7.4, for molecular biology), fluorescein 5(6)-isothiocyanate (FITC), and hexane were purchased from Sigma-Aldrich. *N*-(3-aminopropyl)methacrylamide hydrochloride (APMA) was purchased from Polysciences. Coomassie protein assay kit and 8-well chambered cover glasses were purchased from Thermo Scientific. Ethanol (95%) was purchased from Fisher Scientific. F3–Cys peptide (KDEPQRRSARLSAKPAPPKPEPKPKKAPAKKC) was purchased from SynBioSci. The heterobifunctional polyethylene glycol (MAL–PEG–NHS, 2 k) was purchased from Creative PEG Works. Six-well cell culture plates and 96-well microplates were purchased from BD Biosciences. Roswell Park Memorial Institute 1640 medium (RPMI), RPMI 1640 medium, no Phenol Red (colorless RPMI) and Dulbecco's phosphate buffered saline (DPBS) were purchased form Life Technologies. The water was purified with a Milli-Q system from Millipore. All chemicals were used without further purification.

2.2.2 ICG loaded Nanoparticle Synthesis

Preparation of HSA–PAA NPs. The HSA–PAA NPs were prepared by reverse microemulsion polymerization adapted from our previous study involving PAA NPs

synthesis. [25] The monomer solution was prepared in two steps: 1) dissolving HSA (67 mg) in 1 mL of PBS (pH 7.4) and then adding 0.3 mL of NAS (1.7 mg) to the HSA solution under stirring for 2 h at 37 °C; 2) adding AA (689.5 mg), APMA (53.6 mg) and then subsequently GDMA (85%, 360 μL), a cross-linker, to the mixture solution under stirring. This monomer solution was added to 45 mL of deoxygenated hexane that contained surfactants, AOT (1.6 g) and 3.3 mL of Brij 30 (3.1 g). After stirring the mixture under inert atmosphere for 20 min, 100 μL of TEMED and a freshly prepared 100 μL of APS (10%, w/v) were added to the mixture solution to initiate polymerization. The reaction mixture was stirred under inert atmosphere at room temperature. During the radical polymerization, the double bonds in monomer and cross-linker react with initiator or initiated monomers, resulting in a three dimensional polymer network. After 2 h, the solution was concentrated by rotary evaporator and the remaining residue subsequently suspended in ethanol. The reaction mixture solution was transferred into an Amicon Stirred Ultrafiltration Cells (200 mL, equipped with a Biomax 300,000 MWCO membrane) and washed thoroughly with ethanol and distilled water five times respectively. After washing and freeze-drying, 1.0 g (94%) of HSA–PAA NPs was obtained (Scheme 2-1).

Preparation of ICG–HSA–PAA NPs. ICG stock solution (1 mg·mL^{-1}) was prepared in purified water. HSA–PAA NP (50 mg) was dissolved in 8.5 mL of pure water and stirred for 1 h at room temperature. 1.5 mL of ICG stock solution (1 mg·mL^{-1} in pure water) was added into nanoparticle solution and stirred during 2 h at room temperature. These ICG "post-loaded" NPs were rinsed with pure water (20 mL) by Amicon

centrifugal cell (100 kDa). After washing, the NPs were freeze-dried and 42.7 mg of ICG–HSA–PAA NPs were obtained.

Preparation of F3–ICG–HSA–PAA NPs. HSA–PAA NPs (50 mg) were dissolved in 8.5 mL of PBS (pH 7.4) and stirred and sonicated until the solution became homogeneous. 4 mg of bi-functional PEG (MAL–PEG–SCM, 2k) was added into nanoparticle solution and stirred at room temperature. After 20 min, 1.5 mL of ICG solution (1 mg·mL^{-1} in water) was added and stirred for another 10 min. The NPs solution was washed three times with PBS (pH 7.4) by Amicon centrifugal filter (100 kDa). After diluting the solution into a 5 mg·mL^{-1} solution in PBS (pH 7.4), 7mg of F3–Cys peptide was added and the solution was stirred for 2 h at room temperature. To inactivate unreacted maleimide esters, 1.74 mg of L-cysteine was added to the solution and stirred for another 1 h. F3–(3% ICG)–HSA–PAA NPs were washed completely with water using Amicon centrifugal filter (100 kDa). After freeze-drying, 33.0 mg of F3–ICG–HSA–PAA NPs were obtained (Scheme 2-1).
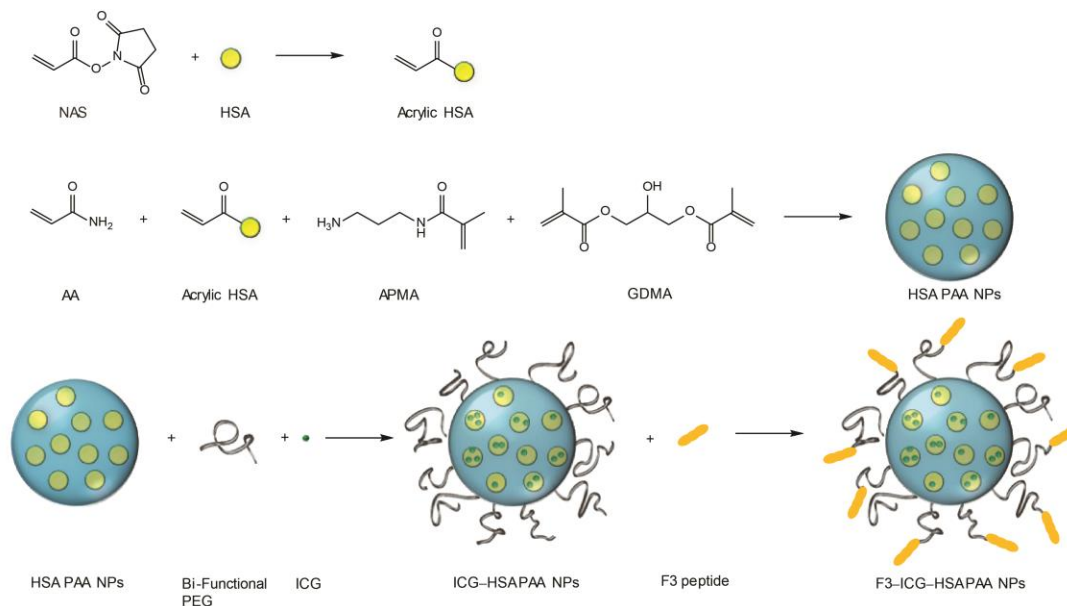
Scheme 2-1 Synthesis of F3–(3% ICG)–HSA–PAA NPs.

2.2.3 Characterization

Dynamic Light Scattering Measurement. The size and surface charge of the NPs were measured using dynamic light scattering (DLS) with a Delsa Nano C particle analyser (Beckman Coulter). For the size measurements, the HSA–PAA NPs solution was prepared in PBS (pH 7.4) (0.5 mg·mL^{-1}), stirred for 1 h and sonicated for 5 min. For the surface charge measurements, the sample solution was prepared in pure water instead of PBS (pH 7.4). All the measurements were conducted in triplicate.

Absorbance & Fluorescence Measurement. To monitor the ICG–HSA–PAA NPs' absorption spectrum, UV-1601 UV-vis spectrometer (Shimadzu) was used. A FluoroMax-3 Spectrofluorometer (Jobin Yvon Horiba) was used for fluorescence measurements. The ICG–HSA–PAA NPs solution was prepared (0.1 mg·mL^{-1}) in PBS (pH 7.4). The measurements were conducted in triplicate.

Temperature dependent Fluorescence Test. Fluorescence spectra of 2 mL of (3% ICG)–HSA–PAA NPs, (3% ICG)–PAA NPs (0.1 mg·mL^{-1}), and of naked ICG (0.00291 mg·mL^{-1}) in PBS (pH 7.4), were measured at 25 °C. The temperature was then increased to 37 °C, in a temperature control chamber, and each sample was incubated for 5 min in the chamber. Any molecular degradation that might have occurred during this incubation period has been corrected, based on Figure 2-4a. All measurements were conducted in triplicate.

Photo-stability Test. 3 mL of (3% ICG)–HSA–PAA NPs, (3% ICG)–PAA NPs (0.1 mg·mL^{-1}), and naked ICG (0.00291 mg·mL^{-1}) in PBS (pH 7.4) were placed at 9 cm below an UV lamp (Spectroline EF-160C, 254 nm, 115 volts, 60 Hz, 0.2 Amps). These samples

were exposed to UV light for 10 min at room temperature. The fluorescence spectra were obtained before and after the light exposure and compared.

Transmission Electron Microscopy (TEM). The TEM image was obtained using a Philips CM-100 transmission electron microscope. The NP sample for TEM was prepared by dissolving 0.1 mg of (3% ICG)–HSA–PAA NPs in 1 mL of pure water. The NPs were stained with uranyl-acetate and imaged on carbon coated copper grids.

Coomassie Protein Assay. The amount of HSA in HSA–PAA NPs was analyzed by Coomassie protein assay. 30 µL of HSA–PAA NPs solution (10 mg·mL^{-1} in PBS (pH 7.4)) was added into 1.5 mL of Coomassie protein assay solution. As a control sample, 30 µL of pure PBS (pH 7.4) was mixed with 1.5 mL of Coomassie protein assay solution. The absorbance of this mixture and that of the control were taken at 595 nm and the HSA amount was calculated from a calibration curve made with free HSA.

Photoacoustic Set-up and Measurement. A homemade photoacoustic imaging setup (Scheme 2-2) was employed to obtain the photoacoustic spectra from the ICG loaded NPs. A tuneable optical parametric oscillator (OPO) (Vibrant B, Opotek) pumped by the second harmonic of a Nd:YAG laser (Brilliant B, BigSky), with a pulse duration of 10 ns, a tuning range of 700 - 800 nm, and a repetition rate of 10 Hz was used as the excitation source. This light was collimated and used to illuminate a transparent soft tubing (0.58 mm - BD Intramedic), mimicking a blood vessel, containing the ICG NPs. The NPs were used at a concentration of 5 mg·mL^{-1}. The OPO was used to illuminate ICG–HSA–PAA NPs flowing through soft tubing that mimics blood vessels. The light fluence was about 5 mJ·cm^{-2}, which is much lower than the ANSI standard limit of 30 mJ·cm^{-2}. A high-sensitivity, wide-bandwidth (132.63% at - 6 dB with a central frequency

of 9.01 MHz) ultrasonic transducer, cylindrically focused with a focal length of 0.75 inch, was used to detect the photoacoustic signals emitted by the NPs. The photoacoustic signals received by the transducer were amplified and digitized using a 500 MHz digital oscilloscope (TDS, 540B, Tektronix), and subsequently transferred to a computer. Each data point was obtained by averaging of 30 signal measurements. A beam splitter was used to direct a small fraction of the beam from the OPO to a photodiode (Model 2031, Newport Corporation) for the monitoring of laser fluctuation. This served to normalize the measured photoacoustic signal intensities so as to take into account any errors due to the instability in the laser output power.
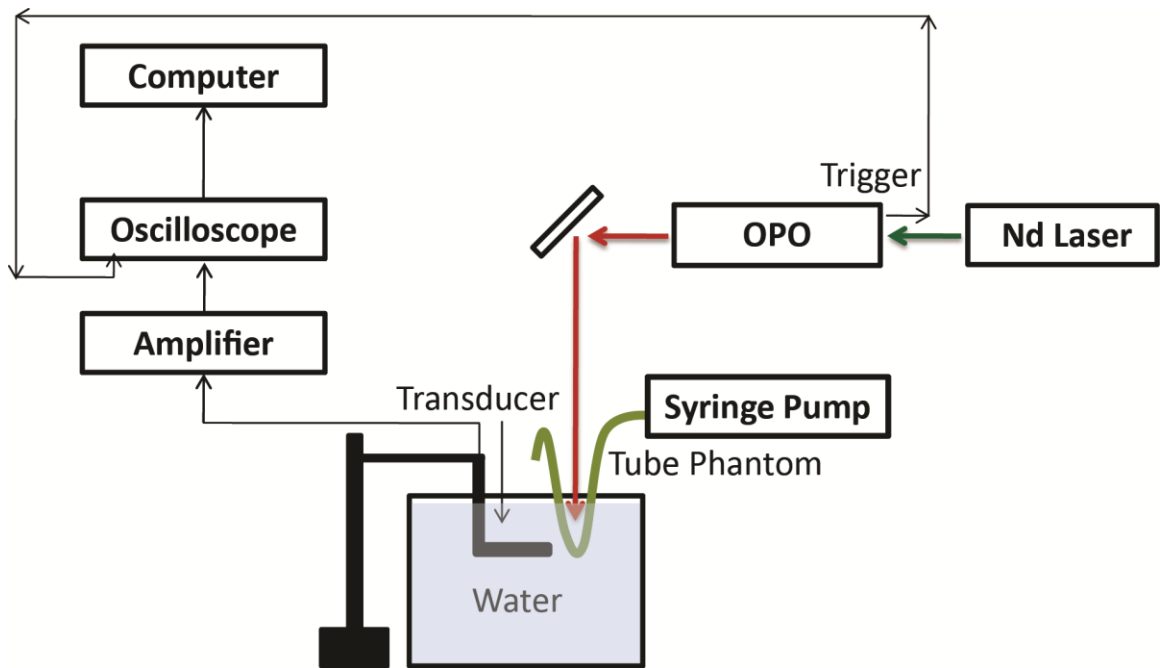
Scheme 2-2 Homemade setup for photoacoustic image.

2.2.4 *In Vitro* Tests

Cell Culture. Two different cell lines, rat gliosarcoma cell line (9L) and human breast adenocarcinoma cell line (MCF-7) were cultivated in RPMI-1640 media with 10%

heat inactivated fetal bovine serum (HI-FBS) and 1% Antibiotic-Antimycotic (100X). These cells were plated into 96 well plates for the cell viability assays and 8 well chambered slides for fluorescence imaging.

Cytotoxicity (CCK-8 Assay). The cytotoxicity of the NPs was tested by the CCK-8 assay, which is based on the reduction of tetrazolium salt, WST-8, to a water soluble formazan dye by the dehydrogenase activity of viable cells. [33] Approximately 5000 9L cells, in 100 µL of RPMI, were seeded on each well of a 96 well plate. The 25 µL of (3% ICG)–HSA–PAA NPs, HSA–PAA NPs and PAA NPs solution (10, 5, 2.5 and 1.25 mg·mL^{-1} in PBS (pH 7.4)) were added into each well to prepare final NP concentrations of 2, 1, 0.5 and 0.25 mg·mL^{-1}. Wells containing 9L cells without any NPs treatment served as the control. After 24 h incubation at 37 °C, the NP solutions were removed gently to avoid absorbance interference of ICG and/or phenol red with WST-8 formazan dye. CCK-8 stock solution (9% (v/v) CCK-8 in colorlesss RPMI, no phenol red) was then pipetted into each well (100 µL) and incubated for 4 h at 37°C. The amount of WST-8 formazan dye produced was analysed, by measuring absorbance at 492 nm, by an Anthos 2010 Microplate Absorbance Reader (Biochrom Ltd.).

Fluorescence Imaging. For fluorescence imaging, both 9L (F3 positive cell line) and MCF-7 cells (F3 negative cell line) were seeded into 8 well chambered slides. F3–(3% ICG)–FITC–HSA–PAA NPs, F3–(3% ICG)–FITC–PAA NPs and PEG–(3% ICG)–FITC–PAA NPs were added to each well to prepare a final concentration of 1 mg·mL^{-1} in cell culture medium. After 30 min incubation, any unbound NPs were washed with DPBS three times, followed by addition of colorless RPMI. Confocal fluorescence images were obtained on a Leica Inverted SP5X Confocal Microscope System.

2.3 Results and Discussion

2.3.1 Characterization of ICG–HSA–PAA NPs

Compared to traditional PAA NPs, the HSA–PAA NPs have a larger size, presumably due to the inclusion of HSA inside the NPs. The hydrodynamic size of PAA NPs was 63.3 ($\pm$ 1.0) nm and the zeta potential was 25.2 ($\pm$ 0.9) mV, as measured by DLS. For the HSA–PAA NPs, the size increased to 136.6 ($\pm$ 15.4) nm, but the zeta potential was 26.1 ($\pm$ 0.7) mV, similar to that of the PAA NPs. The negative charge of the HSA did not affect the overall surface charge, probably since most of the conjugated HSA were present inside the polymer matrix. After ICG post-loading, neither size nor zeta potential of the NPs changed much. The latter were recorded, respectively, as 67.3 ($\pm$ 2.1) nm and 24.9 ($\pm$ 0.5) mV for (3% ICG)–PAA NPs and as 133.1 ($\pm$ 7.2) nm and 24.5 ($\pm$ 0.7) mV for (3% ICG)–HSA–PAA NPs (Table 2-1). In addition to the hydrodynamic NPs size, we also monitored the dehydrated size of the NPs using TEM. The size of the dehydrated (3% ICG)–HSA–PAA NPs was around 48 nm (Figure 2-1). We note that the hydrogel matrix easily swells under aqueous conditions but shrinks back when it is dried, leading to a difference between the actual volume and the hydrodynamic volume. [25] The amount of HSA in the NPs was determined by a Coomassie protein assay kit and 403.3 μg of HSA was incorporated in 10 mg of HSA–PAA NPs, which amounted to 4% (w/w) of loading in NPs. To achieve specific targeting, the NPs were attached to the F3 peptide by using a bi-functional PEG as cross-linker, which was conjugated to the primary amines in APMA prior to ICG loading. This order was chosen since if ICG is loaded in advance, the binding site, primary amine, can be blocked by post-loaded ICG.

Table 2-1 Size and zeta potential of PAA and HSA–PAA NPs with 3% (w/w) ICG loading.

Hydrogel Nanoparticles (NPs)	Hydrodynamic Size (nm)	Zeta Potential (mV)
PAA NPs	63.3 (± 1.0)	25.2 (± 0.9)
(3% ICG)–PAA NPs	67.3 (± 2.1)	24.9 (± 0.5)
HSA–PAA NPs	136.6 (± 15.4)	26.1 (± 0.7)
(3% ICG)–HSA–PAA NPs	133.1 (± 7.2)	24.5 (± 0.7)
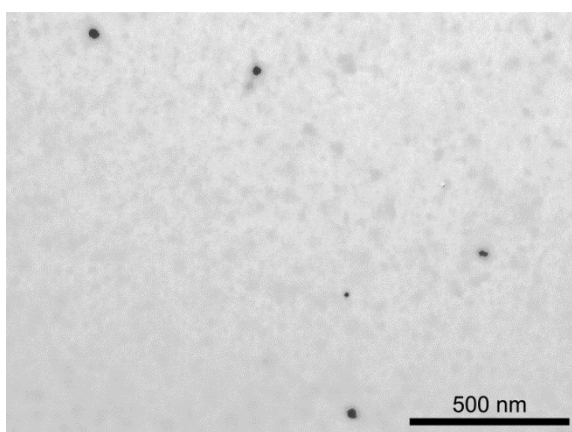
Figure 2-1 TEM image of (3% ICG)–HSA–PAA NPs.

2.3.2 Optimization of ICG Loading within HSA–PAA NPs

ICG has a tendency to aggregate and also leach out of the NP platform when it is loaded at high concentrations. To optimize the ICG loading into the NPs, different amounts of free ICG were loaded into HSA–PAA NPs. During the radical polymerization, ICG loses its double bond and is converted into a leuko form, preventing it from being preconjugated or encapsulated in the nanomatrix. Thus HSA–PAA NPs were loaded with ICG by the post-loading method, which is a quick and easy modification method which facilitates small scale reactions, compared to pre-conjugation or encapsulation. Up to 12%

(w/w), ICG was loaded into the HSA–PAA NPs through post-loading modification that is free of any dye leaching.

We monitored the absorption spectra from the HSA–PAA NPs containing different amounts of ICG (Figure 2-2a). At lower ICG loading, we observe a strong absorbance around 780 nm which corresponds to the free ICG monomer. However, on increasing the amount of ICG, there was a marked increase in the absorbance at 720 nm, due to the formation of ICG dimers. We also compared the fluorescence from the ICG–HSA–PAA NPs' for different ICG loadings (Figure 2-2b). Since the (3% ICG)–HSA–PAA NPs have the highest fluorescence signal, we used the 3% loading for all further experiments.
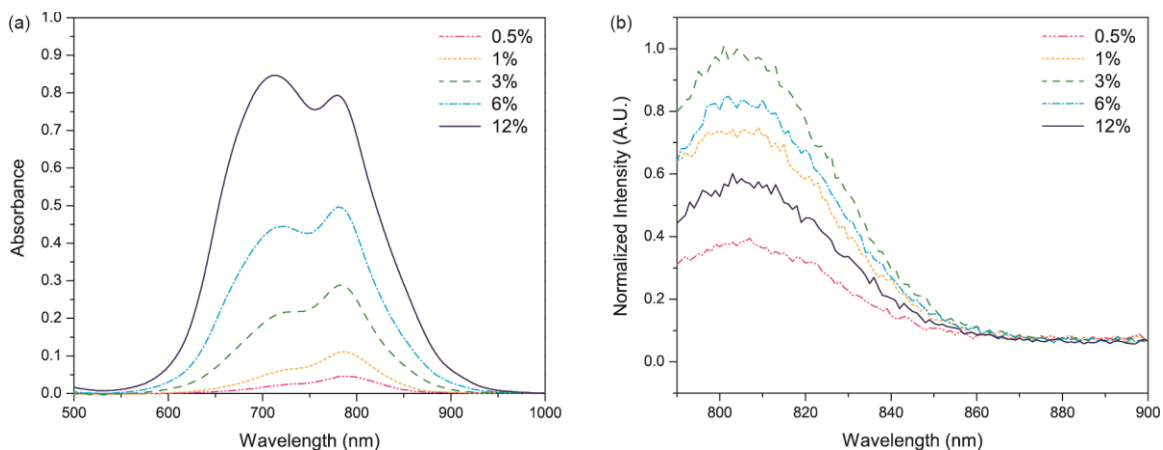
Figure 2-2 (a) Absorption spectra and (b) normalized fluorescence emission spectra of ICG–HSA–PAA NPs, using 780 nm excitation. The absorption and fluorescence measurements were taken with 0.1 mg·mL^{-1} of 0.5 - 12% (w/w) ICG loaded HSA–PAA NPs in PBS (pH 7.4) buffer, showing spectral changes with different ICG loading.

2.3.3 *In Vitro* Test Results for Toxicity

Polyacrylamide hydrogel is a nontoxic polymer and has been used extensively in biomedical applications. [29,34] The nontoxicity of PAA NPs was demonstrated in previous studies, for both *in vitro* and *in vivo* experiments. [25,30,35] The ICG–HSA–

PAA NPs are expected to be non-toxic since HSA is one of the constituents of human blood and ICG is already an FDA approved dye. To test the NP's toxicity, we performed a cytotoxicity assay using a CCK-8 assay on the 9L cell line, with a variety of NPs concentration (0.25, 0.5, 1 and 2 mg·mL^{-1}). All (3% ICG)–HSA–PAA, HSA–PAA and PAA NPs showed higher than 98% cell survival over the 24 h incubation time (Figure 2-3). This result demonstrates that the ingredients of ICG–HSA–PAA NPs do not cause any cytotoxicity.
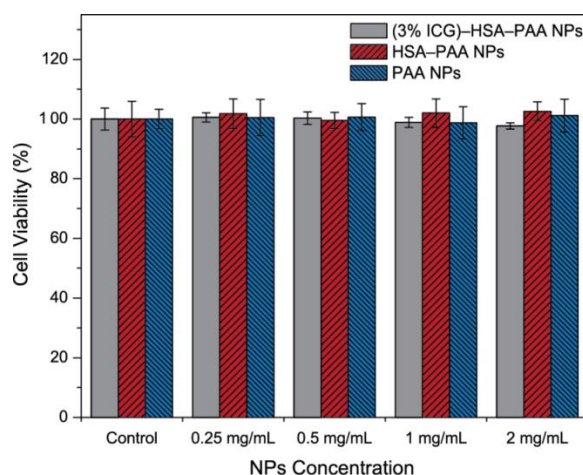
Figure 2-3 Cytotoxicity of NPs in 9L cells. Cell viability of (3% ICG)–HSA–PAA, HSA–PAA and PAA NPs at various concentrations (0.25, 0.5 1, 2 mg·mL^{-1}) was monitored after 24 h incubation with NPs by CCK-8 assay (*n* =8). Control (100%) was 9L cells incubated for 24 h without NPs.

2.3.4 Stability Enhancement of Post-loaded ICG within HSA–PAA NPs

The ICG–HSA–PAA NPs were designed to further enhance the chemical stability of ICG over ICG–PAA NPs. The PAA NPs, like other nano carriers, such as silica, PL–PEG and PLGA NPs, help to increase chemical stability of the ICG dye since the dye is trapped inside the porous PAA nanomatrix, thus limiting accessibility of other chemicals, especially of the large enzymes. [12,17-19,30] For HSA–PAA NPs, the HSA, with its

hydrophobic cavities, binds strongly to the ICG molecules, thus offering greater stability to the ICG, compared to the HSA-less PAA NPs. [36,37]

First, encapsulation in the HSA–PAA NPs helps to improve the stability of ICG in aqueous solution. The degradation rate of free ICG and ICG in different matrixes in PBS (pH 7.4) were monitored by measuring the absorbance of ICG at different time points. The free ICG solution showed fast degradation and only 30 ($\pm$ 3.9) % of the dye remained intact after 24 h at normal body temperature, 37 °C. However, 59 ($\pm$ 6.4) % and 69 ($\pm$ 7.3) % of the ICG remained intact when encapsulated inside the PAA and HSA–PAA NPs, respectively, over the 24 h period, at 37 °C (Figure 2-4a).

Secondly, the HSA–PAA NPs also help to prevent the reduction of ICG fluorescence intensity due to rise in temperature, from 25 °C to 37 °C. For free ICG, we observed a 31% decrease in fluorescence intensity when the temperature was increased to 37 °C. The reduction in fluorescence can be attributed to faster diffusion of ICG at higher temperature, leading to an increased rate of collision with oxygen molecules, and thus increased quenching. [15] However, the reduction in fluorescence intensity was only 7% and 2% for ICG in PAA NPs and HSA–PAA NPs, respectively (Figure 2-4b), due to the limited mobility in the matrix.

Lastly, the HSA–PAA NPs improve the photo-stability by preventing photo-degradation of the ICG dye. Photo-degradation is an irreversible process that leads to a loss in optical properties due to the breakdown of dye molecule into smaller fragments through oxidation processes. [38] The photo-degradation renders the dye ineffective as a contrast agent, due to loss of colour, and also increases its photo-toxicity since ICG produces toxic products following photo-degradation. [39] We observed significant

reduction in the photo-degradation of the ICG dye in the (3% ICG)–HSA–PAA NPs, compared to the free dye. After 10 min UV lamp exposure at 254 nm, 87% and 73% of ICG remained intact in the HSA–PAA and PAA NPs, respectively, while only 44% of the free ICG remained intact (Figure 2-4c). It is well known that this photo-decomposition is caused by reaction of photo-excited ICG molecules with solvent radical species and ions. [2] This protection from photo-decomposition by the NP platform could be attributed to the higher scattering cross section in the UV region of the spectrum and also limiting the interaction of the solvent radical species with the dye molecules compare to free ICG. Additionally, the hydrophobic pocket in HSA might prevent the interaction of radical ions and helps to further improve the photo-stability of ICG.
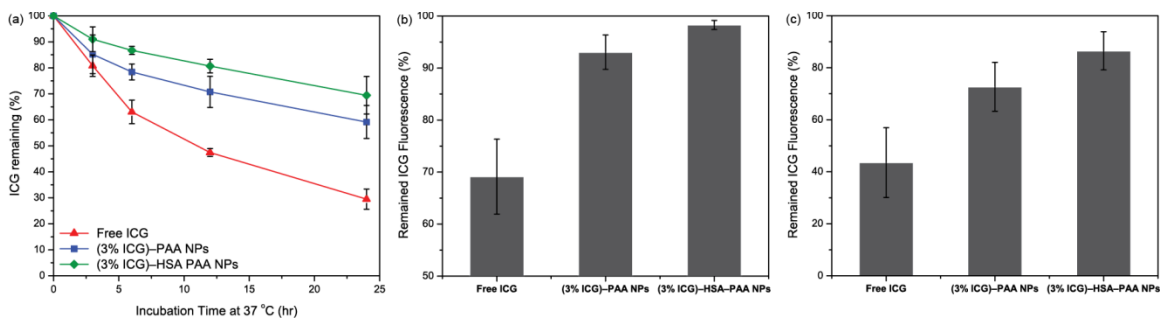
Figure 2-4 Advantages of dye encapsulation in HSA–PAA NPs and PAA NPs. (a) Enhancement of ICG stability, under aqueous conditions at 37 °C, by PAA or HSA–PAA NPs; (b) Prevention of ICG fluorescence quenching, under physiological condition (37 °C) compared to room temperature (25 °C), by encapsulation in PAA or HSA–PAA NPs; (C) Enhancement of ICG photo-stability, under UV lamp illumination (240 nm) for 10 min, by encapsulation in PAA or HSA–PAA NPs.

2.3.5 Photoacoustic Response of ICG–HSA–PAA NPs

To demonstrate the feasibility of photoacoustic imaging using the NPs, we monitor the photoacoustic spectrum from ICG–HSA–PAA NPs (Scheme 2-2). The photoacoustic spectrum was monitored over the range of 700 - 800 nm (Figure 2-5). We observed two

peaks at around 720 nm and 790 nm, which respectively correspond to the signals from the dimer and monomer forms of ICG. Interestingly, the signal peak corresponding to the dimer ICG is much stronger, as compared to the other peak corresponding to the monomer ICG. This is in contrast to the observed optical absorption spectrum of the NPs (Figure 2-2a), where the monomer peak showed a higher value than the dimer peak, at 3% loading, since the photoacoustic signal is generally proportional to the absorbance. This may be attributed to the higher fluorescence quantum yield for the ICG monomer, compared to its dimer form. For the ICG monomer, most of the energy is converted to fluorescence; whereas for the dimer form, most of the energy is converted to heat and subsequently to photoacoustic signal, due to the low fluorescence quantum yield. Thus we observed a higher photoacoustic signal at 720 nm than at 790 nm.
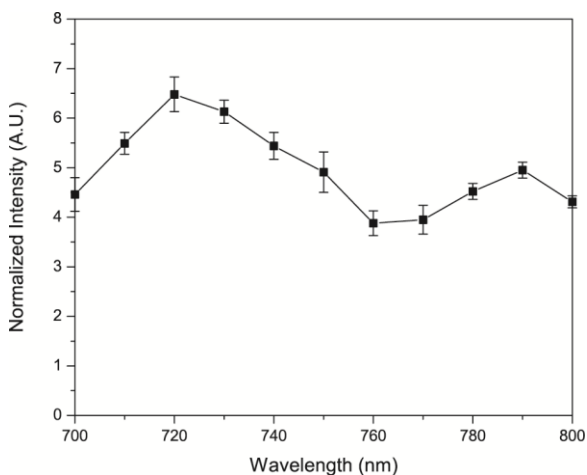
Figure 2-5 Photoacoustic spectrum of (3% ICG)–HSA–PAA NPs (5 mg·mL^{-1}) in PBS (pH 7.4).

2.3.6 *In Vitro* Cell Targeting Using Fluorescence Imaging

The fluorescence imaging of ICG–HSA–PAA NPs and ICG–PAA NPs, both in targeted (F3 conjugated) and non-targeted (PEG conjugated) forms, were performed

using a Leica SP5X confocal microscope. Due to limited availability of appropriate light source and filters, we could not obtain clear ICG images. To overcome this limitation, we introduced FITC dye into the HSA–PAA NPs. FITC has a high fluorescence quantum yield and helped compliment the fluorescence signal from ICG, so as to determine the targeting efficiency, with very high accuracy, for each of the three NPs carrying ICG. To avoid leaching out, the FITC dye was pre-conjugated into the HSA–PAA and PAA NPs during NP synthesis, using a previously reported protocol, and then the ICG dye was post-loaded after conjugation of the targeting moiety, F3. [25] The F3 peptide was used since it is a commercially available targeting moiety and has been reported to bind to the nucleolin receptors, which are overexpressed in some cancer cells. [40,41] To study the specific binding ability of the ICG carrier, three different NPs were prepared, including F3–(3% ICG)–FITC–HSA–PAA NPs, F3–(3% ICG)–FITC–PAA NPs and PEG–(3% ICG)–FITC–PAA NPs. All three types of NPs were loaded into 9L and MCF-7 cell lines and incubated for 30 min, at a 1 mg·mL^{-1} concentration. The 9L cells (high expression of nucleolin receptors) were used as a positive control, and the MCF-7 cells (lower expression of nucleolin) as the negative control. The targeting efficiency of the NPs was calculated, based on the fluorescence intensity from the cells. We observed a 2.4 and 2.3 times higher binding efficiency in the 9L cell line, for F3–(3% ICG)–HSA–PAA NPs and F3–(3% ICG)–PAA NPs, respectively, compared to the MCF-7 cells (Figure 2-6). The PEG–PAA NPs were barely visible, indicating poor uptake of these NPs by both cell lines.
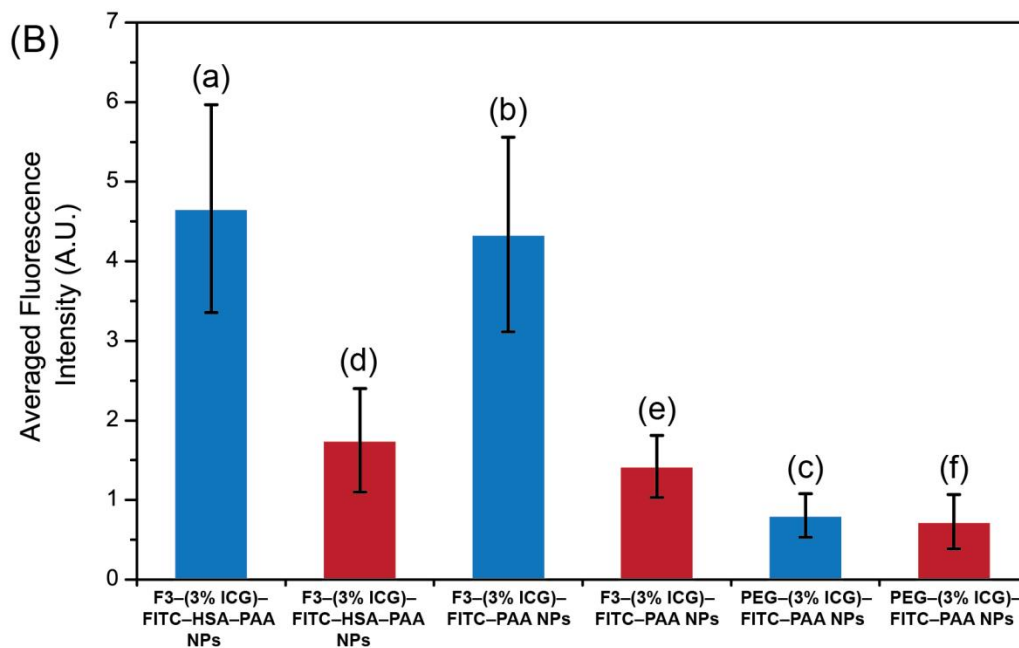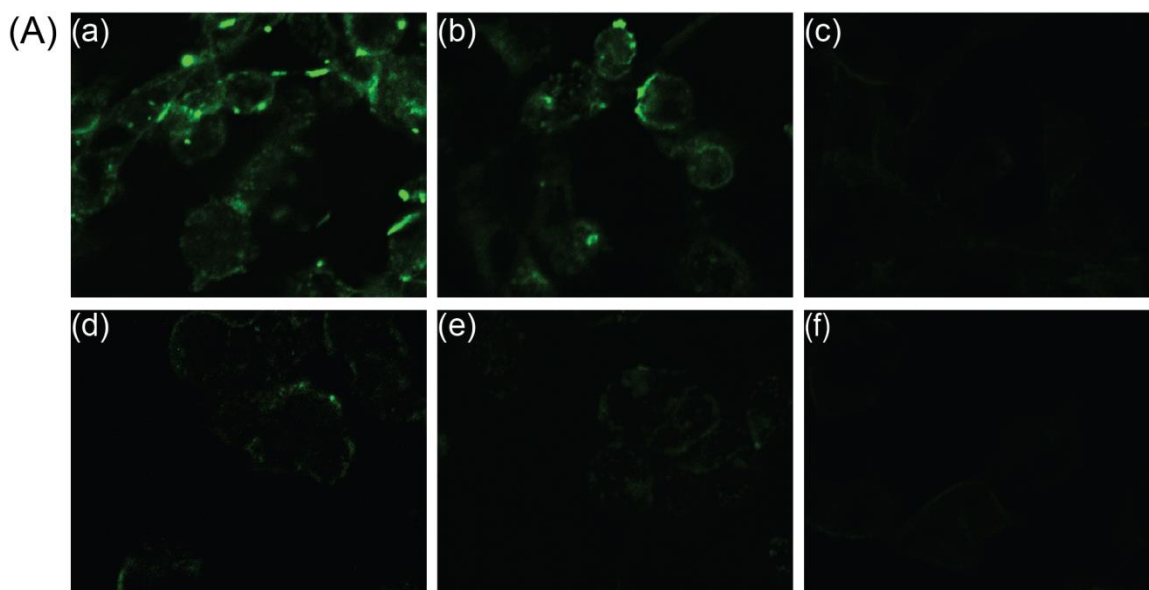
Figure 2-6 Confocal images of F3 targeted selective delivery of ICG: A-a) F3–(3% ICG)–FITC–HSA–PAA NPs in 9L cells; A-b) F3–(3% ICG)–FITC–PAA NPs in 9L cells; A-c) PEG–(3% ICG)–FITC–PAA NPs in 9L cells; A-d) F3–(3% ICG)–FITC–HSA–PAA NPs in MCF-7 cells; A-e) F3–(3% ICG)–FITC–PAA NPs in MCF-7 cells; A-f) PEG–(3% ICG)–FITC–PAA NPs in MCF-7 cells; B) Relative cell specificity of F3 and ICG containing NPs, based on averaged fluorescence intensity of the FITC fluorescence confocal image (blue bar is for 9L and red bar is for MCF-7 cells). For quantification, the averaged background was subtracted from the intensity of the cell images.

2.4 Conclusions

In summary, a novel ICG nanocarrier based on a hybrid polyacrylamide matrix and HSA was developed, so as to effectively overcome the inherent drawbacks associated with the free ICG dye. This new type of NP carrier contains 40.3 µg of HSA per 1 mg of NPs, i.e. 4% (w/w) loading, with a size of 133.1 nm and surface charge of 24.5 mV. *In vitro* toxicity of the NPs was monitored at several concentrations, showing no significant biological toxicity. These NPs were modified by adding the contrast agent, ICG, and also the tumor targeting F3 peptides. The optimized ICG loading into NPs was found to be 3%, since at this loading, the NPs containing ICG have the strongest fluorescence intensity. The ICG–HSA–PAA NPs show an outstanding ability to protect the encapsulated ICG from 1) fast chemical degradation under aqueous conditions, 2) reduction in fluorescence at higher temperature, and 3) photo-degradation. The photoacoustic spectrum of ICG–HSA–PAA NPs showed two strong peaks, at 720 nm and 790 nm, in the NIR range. However, contrary to the absorbance and fluorescence spectra, the dimeric ICG form (720 nm) shows a stronger photoacoustic signal than the monomeric form of ICG (790 nm), due to the lower fluorescence quantum yield of the dimeric ICG form. Moreover, after successful modification with the targeting moiety, F3–Cys, these NPs showed high cell specific selectivity. We believe that this polymeric nanoparticle design could also be used as an efficient, biodegradable and biocompatible carrier for other kinds of fluorescent molecules, which could be of interest in important biomedical applications of fluorescence and photoacoustic imaging. [42]

2.5 Acknowledgments

2.6 Refercences

(1)   Yaseen, M. A.; Yu, J.; Jung, B.; Wong, M. S.; Anvari, B. *Mol. Pharmaceutics* **2009**, *6*, 1321.

(2)   Saxena, V.; Sadoqi, M.; Shao, J. *J. of pharm. Sci.* **2003**, *92*, 2090.

(3)   Jung, B.; Anvari, B. *Biotechnol. Prog.* **2012**, *28*, 533.

(4)   Berezin, M. Y.; Lee, H.; Akers, W.; Achilefu, S. *Biophys. J.* **2007**, *93*, 2892.

(5)   Kirchherr, A. K.; Briel, A.; Mader, K. *Mol. Pharmaceutics* **2009**, *6*, 480.

(6)   McCorquodale, E. M.; Colyer, C. L. *Electrophoresis* **2001**, *22*, 2403.

(7)   Malicka, J.; Gryczynski, I.; Geddes, C. D.; Lakowicz, J. R. *J. Biomed. Opt.* **2003**, *8*, 472.

(8)   Yu, J.; Yaseen, M. A.; Anvari, B.; Wong, M. S. *Chem. Mater.* **2007**, *19*, 1277.

(9)   Alander, J. T.; Kaartinen, I.; Laakso, A.; Patila, T.; Spillmann, T.; Tuchin, V. V.; Venermo, M.; Valisuo, P. *Int. J. Biomed. Imaging* **2012**, *2012*, 940585.

(10)   de la Zerda, A.; Liu, Z.; Bodapati, S.; Teed, R.; Vaithilingam, S.; Khuri-Yakub, B. T.; Chen, X.; Dai, H.; Gambhir, S. S. *Nano Lett.* **2010**, *10*, 2168.

(11)   de la Zerda, A.; Bodapati, S.; Teed, R.; May, S. Y.; Tabakman, S. M.; Liu, Z.; Khuri-Yakub, B. T.; Chen, X.; Dai, H.; Gambhir, S. S. *ACS Nano* **2012**, *6*, 4694.

(12)   Zheng, X.; Xing, D.; Zhou, F.; Wu, B.; Chen, W. R. *Mol. Pharmaceutics* **2011**, *8*, 447.

(13)   Mauerer, M.; Penzkofer, A.; Zweck, J. *J. Photochem. Photobiol. B* **1998**, *47*, 68.

(14)   Saxena, V.; Sadoqi, M.; Shao, J. *J. Photochem. Photobiol. B, Biology* **2004**, *74*, 29.

(15)   Boddington, S.; Sutton, E. J.; Jones, E.; Purcell, D. D.; Henning, T. D.; Tavri, S.; Meier, R.; Sista, A.; Fu, Y.; Daldrup-Link, H. *Contrast Media Mol. Imaging* **2008**, *3*, 191.

(16)   Geddes, C. D.; Cao, H.; Gryczynski, I.; Gryczynski, Z.; Fang, J. Y.; Lakowicz, J. R. *J. Phys. Chem. A* **2003**, *107*, 3443.

(17)   Kim, G.; Huang, S. W.; Day, K. C.; O'Donnell, M.; Agayan, R. R.; Day, M. A.; Kopelman, R.; Ashkenazi, S. *J. Biomed. Opt.* **2007**, *12*, 044020.

(18)   Quan, B.; Choi, K.; Kim, Y. H.; Kang, K. W.; Chung, D. S. *Talanta* **2012**, *99*, 387.

(19)   Zheng, C.; Zheng, M.; Gong, P.; Jia, D.; Zhang, P.; Shi, B.; Sheng, Z.; Ma, Y.; Cai, L. *Biomaterials* **2012**, *33*, 5603.

(20)   De la Zerda, A.; Zavaleta, C.; Keren, S.; Vaithilingam, S.; Bodapati, S.; Liu, Z.; Levi, J.; Smith, B. R.; Ma, T. J.; Oralkan, O.; Cheng, Z.; Chen, X.; Dai, H.; Khuri-Yakub, B. T.; Gambhir, S. S. *Nat. Nanotechnol.* **2008**, *3*, 557.

(21)   Bunschoten, A.; Buckle, T.; Kuil, J.; Luker, G. D.; Luker, K. E.; Nieweg, O. E.; van Leeuwen, F. W. *Biomaterials* **2012**, *33*, 867.

(22)   Lim, Y. T.; Noh, Y. W.; Han, J. H.; Cai, Q. Y.; Yoon, K. H.; Chung, B. H. *Small* **2008**, *4*, 1640.

(23)   Naik, P. N.; Chimatadar, S. A.; Nandibewoor, S. T. *J. Photochem. Photobiol. B, Biology* **2010**, *100*, 147.

(24)   Ray, A.; Rajian, J. R.; Lee, Y. E.; Wang, X.; Kopelman, R. *J. Biomed. Opt.* **2012**, *17*, 057004.

(25)   Hah, H. J.; Kim, G.; Lee, Y. E.; Orringer, D. A.; Sagher, O.; Philbert, M. A.; Kopelman, R. *Macromol. Biosci.* **2011**, *11*, 90.

(26)   Lee, Y. E.; Ulbrich, E. E.; Kim, G.; Hah, H.; Strollo, C.; Fan, W.; Gurjar, R.; Koo, S.; Kopelman, R. *Anal. Chem.* **2010**, *82*, 8446.

(27)   Avula, U. M.; Kim, G.; Lee, Y. E.; Morady, F.; Kopelman, R.; Kalifa, J. *Heart Rhythm* **2012**, *9*, 1504.

(28)   Wang, S.; Kim, G.; Lee, Y. E.; Hah, H. J.; Ethirajan, M.; Pandey, R. K.; Kopelman, R. *ACS Nano* **2012**, *6*, 6843.

(29)   Caulfield, M. J.; Qiao, G. G.; Solomon, D. H. *Chem. Rev.* **2002**, *102*, 3067.

(30)   Qin, M.; Hah, H. J.; Kim, G.; Nie, G.; Lee, Y. E.; Kopelman, R. *Photochem. Photobiolo. Sci.* **2011**, *10*, 832.

(31)   Tang, W.; Xu, H.; Park, E. J.; Philbert, M. A.; Kopelman, R. *Biochem. Biophys. Res. Commun.* **2008**, *369*, 579.

(32)   Orringer, D. A.; Koo, Y. E.; Chen, T.; Kim, G.; Hah, H. J.; Xu, H.; Wang, S.; Keep, R.; Philbert, M. A.; Kopelman, R.; Sagher, O. *Neurosurgery* **2009**, *64*, 965.

(33)   Zhang, Y.; Wang, L.; Sun, Y.; Zhu, Y.; Zhong, Z.; Shi, J.; Fan, C.; Huang, Q.
         ACS Appl. Mater. Interfaces **2013**, *5*, 5291.

(34)   Christensen, L. H.; Breiting, V. B.; Aasted, A.; Jorgensen, A.; Kebuladze, I. *Plast.
         Reconstr. Surg.* **2003**, *111*, 1883.

(35)   Nie, G.; Hah, H. J.; Kim, G.; Lee, Y. E.; Qin, M.; Ratani, T. S.; Fotiadis, P.;
         Miller, A.; Kochi, A.; Gao, D.; Chen, T.; Orringer, D. A.; Sagher, O.; Philbert, M.
         A.; Kopelman, R. *Small* **2012**, *8*, 884.

(36)   Trynda-Lemiesz, L. *Bioorg. Med. Chem.* **2004**, *12*, 3269.

(37)   Sułkowska, A. *J. Mol. Struct.* **2002**, *614*, 227.

(38)   Verhoeven, J. W. *Pure Appl. Chem.* **1996**, *68*, 2223.

(39)   Engel, E.; Schraml, R.; Maisch, T.; Kobuch, K.; Konig, B.; Szeimies, R. M.;
         Hillenkamp, J.; Baumler, W.; Vasold, R. *Invest. Ophthalmol. Visual Sci.* **2008**, *49*,
         1777.

(40)   Porkka, K.; Laakkonen, P.; Hoffman, J. A.; Bernasconi, M.; Ruoslahti, E. *Proc.
         Nat. Acad. Sci.U.S.A.* **2002**, *99*, 7444.

(41)   Christian, S.; Pilch, J.; Akerman, M. E.; Porkka, K.; Laakkonen, P.; Ruoslahti, E.
         J. Cell. Biol. **2003**, *163*, 871.

(42)   Zhang, Y.; Yang, J. *J. Mater. Chem. B* **2013**, *1*, 132.

CHAPTER 3
NANOPHOTOSENSITIZERS ENGINEERED TO GENERATE A TUNABLE MIX OF REACTIVE OXYGEN SPECIES, FOR OPTIMIZING PHOTODYNAMIC THERAPY, USING A MICROFLUIDIC DEVICE

3.1 Introduction

The reactive oxygen species (ROS) are several highly oxidative molecules and radicals such as singlet oxygen ($^1O_2$), hydroxyl radical, superoxide anion radical, hydrogen peroxide, etc. [1] These ROS can be generated by visible light with the help of appropriate photosensitizers. [1-3] This mechanism underlies photodynamic therapy (PDT), which is a clinically approved noninvasive localized therapeutic modality for cancer, cardiovascular, ophthalmic, dermatological and dental diseases. [3-9] The interest in optimizing nanophotosensitizers is associated with their advantages as PDT agents, due to their potential for increased efficiency, targetability and biocompatibility, as well as their theranostic (therapy + diagnostics) operation. [1.10-12]

The utility of PDT in medical applications is restricted due to the following factors: 1) wavelength-dependent tissue penetration depth of the light, 2) inefficient delivery of photosensitizer (PS) to targeted area, 3) loss of PDT efficacy due to aggregation, degradation, or reduction of photosensitizers, and 4) dark toxicity of the photosensitizer. [1,10,13] Notably, PDT efficacy can be significantly improved when nanoparticles (NPs)

are applied as PS carriers, as the use of NPs can help overcome the limitations 2), 3) and 4) listed above. [1,5,14-17] Methylene Blue (MB) is a promising PDT dye due to its high quantum yield ($\Phi_\Delta \approx 0.5$) and long absorption wavelength ($\lambda_{max} = 664$ nm), enabling a better light penetration depth in live tissue, as well as due to its high solubility in aqueous media. [10,18] However, MB's use for *in vivo* PDT has been limited because of its conversion into an inactive form (leuko MB) by enzyme reduction reactions that occur in the blood stream. At higher concentration, MB may form aggregates that reduce the fluorescence quantum yield; furthermore, the MB molecule lacks specificity towards target tissues. [18,19]

In our previous studies, MB loaded polyacrylamide nanoparticles (PAA NPs) have been developed by two different loading methods, encapsulation and chemical conjugation. [10,20] The PAA NPs were found to be biocompatible and biodegradable nanocarriers; moreover, the NP matrix was easily modified with targeting moieties and successfully protected the MB from reduction/conversion by bio-enzymes. [19,21-24] For making the MB NPs, the conjugation approach was found to be the most efficient method, demonstrated by higher loading, negligible leaching of MB from the nanocarrier, and by better PDT efficacy, probably due to a more homogeneous distribution of the high amounts of conjugated MB inside the NP matrix. [10] These MB conjugated PAA NPs showed a PDT efficacy (per 1 mg of NPs) of almost 9 times that of MB encapsulated PAA NPs. This PDT efficacy was estimated by the traditional kinetics-based method: *i.e.*, by determining the rate constant, *k*, of the first order decay kinetics of anthracence-9,10-dipropionic acid (ADPA), under oxidative quenching by the produced ROS. [10,20,25]

45

Notably, upon increasing the photosensitizer loading, the MB conjugated PAA NPs showed an upper limit for the k value. The k value initially increased with MB loading, but then peaked and decreased. [10,21] This limitation on the PDT efficacy of the MB conjugated NPs — probably due to aggregation of MB moieties and self-quenching of produced excitations and/or ROS inside the nanocarriers — may be overcome by modifying the NP matrix structure through the use of longer cross-linkers. This is expected to allow 1) longer distances (gaps) between the conjugated MB moieties, 2) a higher oxygen permeability, and 3) a lower collision probability between the produced ROS.

Herein, we present the preparation of a modified MB–PAA NP, which uses poly(ethylene glycol) dimethacrylate (PEGDMA, $M_n = 550$), a cross-linker that is longer than the 3-(Acryloyloxy)-2-hydroxypropyl methacrylate, (AHM, MW = 214), which was used for previously developed MB conjugated PAA NPs. [10] The new PEGDMA PAA NP also uses a smaller mole fraction of the cross-linker per nanoparticle, so as to further enlarge the average pore size of the NP matrix. The PEGDMA PAA NPs were conjugated with different amounts of MB, and then characterized. Their ROS productivity was investigated using two ROS sensing dyes, ADPA and Singlet Oxygen Sensor Green (SOSG), so as to determine the optimal MB loading for PDT.

In addition, a new microfluidic chip was introduced for quick and reliable *in vitro* PDT tests. The microfluidic chip is a promising analytic device for screening PDT efficiency due to its low cost, high-throughput and ease of controlling the micro-environment. [26,27] It should be noted that the therapeutic effect of PDT depends not only on the dose of the drugs but also on the doses of light and oxygen, making a reliable

estimation of the therapeutic efficacy difficult and lengthy. Regarding *in vitro* PDT tests, usually they are performed in chambered cover glasses, for one specific test condition per experiment, and it is difficult to increase the number of tests done simultaneously, using several NP samples, due to the limited illumination area of the laser light source. [10,19,21] It would be expensive to design an intense and monochromatic light source with a large enough illumination area; on the other hand, if multiple small light sources were used, it would be challenging to have the same flux of the light source on each PDT test area. Thus, employing a new approach, batches of NPs with three different MB loadings were tested simultaneously on the microfluidic chip, so as to determine their cell killing efficacy by PDT. Also, this device allowed to perform several PDT efficacy tests under exactly identical test conditions (the same NP concentration, oxygen concentration, and homogeneous light illumination) while using only small amounts of test sample. Based on this, results for light illumination at half maximal inhibitory time (IT_{50}) were derived by measuring cell survival at varying light illumination time periods, for given MB–PEGDMA PAA NP doses, using C6 glioma cancer cells.

3.2 Experimental Section

3.2.1 Materials

Materials. Acrylamide (AA), poly(ethylene glycol) dimethacrylate, M_n 550, (PEGDMA), ammonium persulfate (APS), *N,N,N',N'*- tetramethylethylenediamine (TEMED), sodium dioctylsulfosuccinate (AOT), Brij 30, dimethyl sulfoxide (DMSO), phosphate buffered saline (BioReagent, pH 7.4, for molecular biology), β-nicotinamide adenine dinucleotide, reduced dipotassium salt (NADH), diaphorase from *Clostridium*

kluyveri (NADH dehydrogenase), Trichloro(1H,1H,2H,2H-perfluorooctyl)silane and hexane were purchased from Sigma-Aldrich. *N*-(3-aminopropyl)methacrylamide hydrochloride (APMA) was purchased from Polysciences. Dicarboxymethylene blue NHS ester (DCMB-SE) was purchased from European Molecular Precision Biotech. Singlet Oxygen Sensor Green (SOSG), 9,10-dipropionic acid disodium salt (ADPA), Dulbecco's Modified Eagle Medium (DMEM),colorless DMEM (no phenol red), 100X Antibiotic-Antimycotic and LIVE/DEAD® Viability/Cytotoxicity Kits were purchased from Life Technologies. The water was purified with a Milli-Q system from Millipore Corporation.   SU8 2050 was purchased from MicroChem Corporation. Poly(dimethylsiloxane) (PDMS) kit (Sylgard 184) was purchased from Dow Corning Corporation. Glass slides were purchased from Fisher Scientific. All chemicals were used without further purification.

3.2.2 MB–PEGDMA PAA NPs Synthesis

Preparation of MB–PEGDMA PAA NPs. The MB–PEGDMA PAA NPs were prepared similarly to a previously reported MB–PAA NPs method. [10] A 100 µL of DCMB-SE solution (50 µg·µL^{-1} in DMSO) was added to a monomer solution including 368 mg of AA and 28 mg of APMA in 0.93 mL of PBS (pH 7.4). After 2 h incubation for MB conjugation with APMA, 53.4 µL of PEGDMA cross-linker was added into the monomer solution. The resultant monomer solution was then added into a 100 mL round bottomed flask containing 30 mL of deoxygenated hexane, 1.07 g of AOT and 2.2 mL of Brij 30 surfactants. To initiate radical polymerization, 100 µL of TEMED and 100 µL of APS (15% w/v) were added to the reaction mixture under inert conditions and stirred for 2 h at room temperature. The polymerized NPs were concentrated by rotary evaporation,

to remove hexane, and washed with enough ethanol and pure water, using Amicon Stirred Ultrafiltratoin Cells (200mL, equipped with a Biomax 300,000 MWCO membrane). The washed MB–PEGDMA PAA NPs were freeze-dried and stored at -20 °C.

3.2.3 Characterization

Characterization. The absorption spectra were taken on a UV-1601 UV-vis spectrometer (Shimadzu) and a FluoroMax-3 Spectrofluorometer (Jobin Yvon Horiba) was used for fluorescence spectra. For both spectra, 1 mg·mL^{-1} of MB–PEGDMA PAA NPs solution in PBS (pH 7.4) was used. For the absorbance spectra, background absorbance from the scattering of PEGDMA PAA NPs was subtracted, using Origin program. Using the absorbance spectrum of MB–PEGDMA PAA NPs, the actual amount of MB content per NP was calculated, based on the calibration curve of MB-SE in PBS (pH 7.4). The differential intensity based averaged size distribution and the surface charge of the MB–PEGDMA PAA NPs were determined by dynamic light scattering (DLS) using a Delsa Nano C particle analyzer instrument (Beckman Coulter). Transmission electron microscopy (TEM) images of MB–PEGDMA PAA NPs were obtained on a Philips CM-100 transmission electron microscope, using uranyl-acetate staining on the grid. All of the measurements were triplicated.

Detection of ROS (k and S value tests). The ROS produced from the MB–PEGDMA PAA NPs was detected by using ADPA. A 2 mL of MB–PEGDMA PAA NPs solution (1 mg·mL^{-1} in PBS (pH 7.4)), containing 80 μL of ADPA (100 μM in pure water), was irradiated at 660 nm, over different time periods (0, 60, 120, 180, 240, 300, 480 and 660 sec), under constant stirring and temperature (25 °C). The fluorescence

spectra of ADPA, excited at 370 nm, were taken right after each irradiation time period. The ADPA decay constant, the "k value," was calculated by the equation reported previously. [20,25] For the detection of $^1O_2$ emanating from the NPs, a specific chemical probe, SOSG was used. [28-31] A 10 µL aliquot of SOSG (0.5 mM in MeOH) was added to a 2 mL MB–PEGDMA PAA NPs solution (1 mg·mL^{-1} in PBS (pH 7.4)), under constant stirring and temperature (25 °C). Note that the free SOSG can be activated in a pH 7.4 solvent; thus, a "blank spectrum" of SOSG fluorescence (without singlet oxygen) was taken by irradiating at 504 nm. After taking a blank spectrum, the photosensitizer sample was irradiated for 5 min at 660 nm. The enhanced SOSG fluorescence spectrum (λ_{ex} = 504 nm) was obtained immediately after stopping the irradiation of photosensitizer. The arbitrarily defined "S value" constant, for singlet oxygen production, was obtained by calculating the ratio of SOSG fluorescence comparing fluorescence before and after irradiation (enhanced/unenhanced).

Enzymatic Reduction Test of MB–PEGDMA PAA NPs. The enzymatic reduction test of MB–PEGDMA PAA NPs was obtained based on our previous reported method. [19,21] In this test, NADH and diaphorase are mixed with MB. The diaphorase catalyzes oxidation of NADH, and the H$^+$ released from the NADH reduces the MB, converting it into the lueko-MB that neither works as a photosensitizer nor fluoresces. Into 2 mL of 12.1 nmol·mg^{-1} of MB conjugated PEGDMA PAA NPs solution (1 mg·mL^{-1} in PBS (pH 7.4)), 133.6 µL of NADH (10 mg·mL^{-1} in PBS (pH 7.4)) and 200 µL of diaphorase (1 mg·mL^{-1} in PBS (pH 7.4)) were added. The fluorescence emission signal of MB–PEGDMA PAA NPs, excited at 660 nm, was monitored for 10 min, at 25 °C and under constant stirring. As a control, considering the photobleaching effect on MB, the

fluorescence emission signal of the same MB conjugated PEGDMA PAA NPs solution without NADH and diaphorase was monitored. This experiment was repeated with free MB solution and the measurements were conducted in triplicate.

3.2.4 *In Vitro* PDT through Microfluidic Device

Microfluidic Chip Preparation. The microfluidic chips were fabricated using a customized soft lithography process similar to what was reported earlier. [26,27] The replication mold was made of 170 μm thick negative photoresist on a silicone substrate. SU8 2050 (epoxy-based negative photoresist) is spin-coated at 1000 rpm, to reach the target thickness, and patterned with standard photolithography (UV dose 350 mJ·cm^{-2}). The resulting SU8 thickness is measured using a Dektak 6M surface profilometer (Veeco Instruments Inc.). Before applying PDMS, replication molds are coated with a self-assembly monolayer (SAM) of Trichloro(1H,1H,2H,2H-perfluorooctyl)silane by vacuuming for 1 h in a desiccator. Then, a mixture of PDMS prepolymer at a 10:1 ratio (base: curing reagent) was poured onto the mold and peeled off after curing under 100 °C for 1 h. Inlet and outlet reservoirs were punched out using 2 mm and 4 mm diameter biopsy punches (MedPlus Inc.). After an oxygen plasma treatment procedure (200 mTorr, 50 W, 30 sec) was conducted on the surface, the PDMS microfluidic layer was bonded to a glass slide. A post-bake for 20 min at 90 °C was adopted for enhancing the permanent bonding between the PDMS and the glass, finalizing the assembly.

Test of LED Light Illumination Uniformity on Microfluidic Chip. To test the uniformity of light illumination on the microfluidic chip, an LED lamp (625 (± 20) nm, Philips Lumileds) was placed 9 cm above the chip and used as a light source, instead of the microscope light bulb, for mimicking the illumination conditions as would be used in

51

the PDT test. Then, a x2 bright field image of the microfluidic chip was obtained on a Nikon eclipse TE2000-U microscope (Nikon Instruments Inc.). The grayscale intensity of the whole PDT tested area in each quadrant on the bright field image was measured and averaged by ImageJ program.

Cell Culture and PDT Test on the Chip. The C6 rat glioma cells (CCL-107, ATCC) were cultivated in DMEM media with 10% heat inactivated fetal bovine serum (HI-FBS) and 1% 100x Antibiotic-Antimycotic (10,000 units·mL^{-1} of penicillin, 10,000 µg·mL^{-1} of streptomycin, and 25 µg·mL^{-1} of Fungizone®). Prior to cell plating on the microfluidic chip, the chip was coated, using a solution of 0.01% collagen and 0.2% acetic acid in pure water, and incubated overnight at 37 °C. Thereafter, the chip was washed with DMEM media to remove any residual collagen solution, and the C6 cells were subsequently loaded into the microfluidic chip and cultured for about 24 h in the incubator, under 5% CO_2 at 37 °C. In 3 of the 4 wells on the chip, 50 µL of either 2.1 nmol·mg^{-1}, 5.5 nmol·mg^{-1} or 12.1 nmol·mg^{-1} of MB conjugated PEGDMA PAA NPs (0.2 mg·mL^{-1} in DMEM) were injected and the chip was covered by aluminum foil, to protect the sample from light. The remaining well of the microfluidic chip was not treated with NPs solution, and thus served as a control for each condition. After 10 min incubation, the chip was illuminated by LED light (625 (± 20) nm; 35.2 mW), for varying periods of time, ranging from 0 to 21 min, to deliver light doses of 0, 5.6, 11.2, 16.8, 22.4, 28, 33.6 and 39.2 J·cm^{-2} (Scheme 3-1). For 0 min light illumination, the NPs were incubated an extra 21 min (the same condition as for the longest light illumination times) without any light source as a dark toxicity test of NPs on C6 glioma cells. The distance between the chip and the LED was kept at 9 cm. After additional 15 min incubation, without any light,

the MB–PEGDMA PAA NPs solution was removed from the chip. Then, 50 µL of colorless DMEM solution containing 0.25 µL of calcein AM (2 mM in DMSO) and 0.25 µL of ethidium homodimer-1 (2 mM in DMSO) were added to each well. After 10 min incubation, the fluorescence images of calcein AM (excited at 460 - 500 nm), and ethidium homodimer-1 (excited at 530 - 560 nm) were taken, using the Nikon Eclipse TE2000-U microscope. The numbers of live and dead cells in an x10 image were counted manually, and cell viability was calculated by equation 3-1 (eq. 3-1) below.

$$\text{Survivability (\%)} = \frac{\text{\# of live cells (green)}}{\text{\# of live cells (green)} + \text{\# of dead cells (red)}} \times 100 \qquad \textbf{(eq. 3-1)}$$
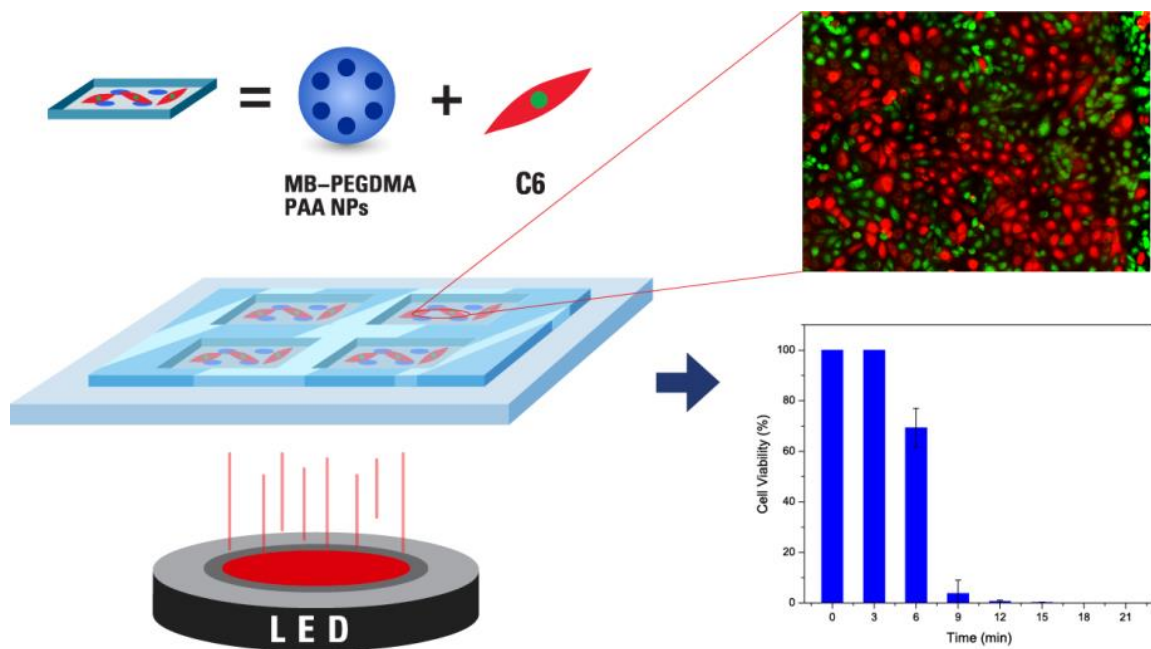
Scheme 3-1 Simplified PDT test setup of MB–PEGDMA PAA NPs on microfluidic chip.

3.3 Results and Discussion

3.3.1 Characteristics of MB–PEGDMA PAA NPs

Based on the differential intensity (%) obtained by DLS, the hydrodynamic size of the MB–PEGDMA PAA NPs was 78.5 ($\pm$ 5.8) nm (Figure 3-1). This is a larger size than the one previously reported for MB–AHM PAA NPs, 55.8 ($\pm$ 5.0) nm. [10] The increased size of the NPs is attributed to the use of a longer cross-linker, PEGDMA (M_n 550), compared to AHM (MW 214). Furthermore, a reduced amount of cross-linker, from 13.6% to 2% (molar ratio of total monomer), may have also helped to increase the hydrodynamic size of the NPs, possibly due to a higher swelling ratio of the hydrogel, caused by the forming of fewer networks inside the NP matrix. [32] The size of the dehydrated MB–PEGDMA PAA NPs was checked by TEM imaging. Similar with previous reported hydrogel NPs, the dehydrated MB–PEGDMA PAA NP shrunk upon drying, its size being around 14 nm (Figure 3-2). [10,24] The surface charge of the MB–PEGDMA PAA NPs was 23.0 ($\pm$ 1.7) mV. This positive surface charge presumably originates from the primary amines, from the APMA monomer that was used for further modification, e.g. for PEGylation, or for attaching a targeting moiety. [10,24,33]
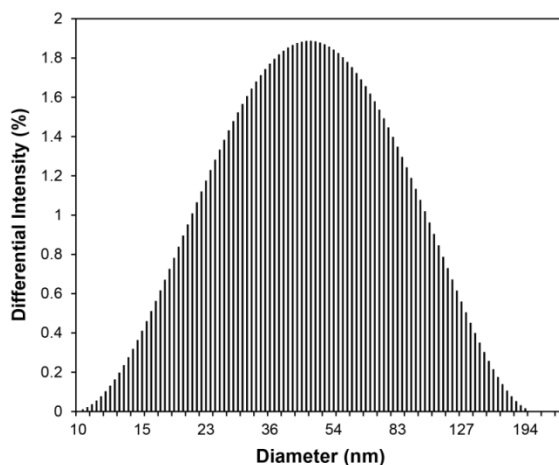
Figure 3-1 DLS of MB–PEGDMA PAA NPs.
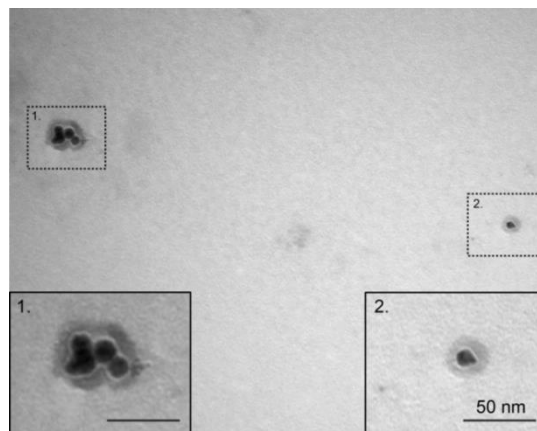
Figure 3-2 TEM of MB–PEGDMA PAA NPs.

The absorption spectra of the MB–PEGDMA PAA NPs, containing different amounts of conjugated MB, were obtained (Figure 3-3a). The MB–PEGDMA PAA NPs have their absorbance peak at 669 nm, which is the same position as for free DCMB-SE. Increasing the conjugated MB amount, another peak appears at 619 nm, which is due to aggregation of the MBs. [34-36] A significant dimer aggregate signal is observed, starting at 12.1 nmol·mg^{-1} of MB loaded PEGDMA PAA NPs, and at higher loadings. Under the same conditions, the excitation and emission spectra of MB–PEGDMA PAA NPs were

55

obtained (Figure 3-3b). There are strong excitation and emission signal peaks at 669 nm and 690 nm, respectively. The excitation peak wavelength matches exactly with the absorbance wavelength. Both the excitation and emission signals increased as more MBs are conjugated. However, these spectral intensities rather decreased from the 12.1 nmol·mg^{-1} of MB loading, which is the same MB loading point where the significant MB dimer absorbance peak was observed. Because of the large amount of MB dimers inside the NP matrix, there might be self-quenching of MB fluorescence, caused by interactions between excited states of MB molecules, and indeed a very low fluorescence signal was obtained, at the highest MB loading, 29.6 nmol·mg^{-1}, in PEGDMA PAA NPs. [10,18]
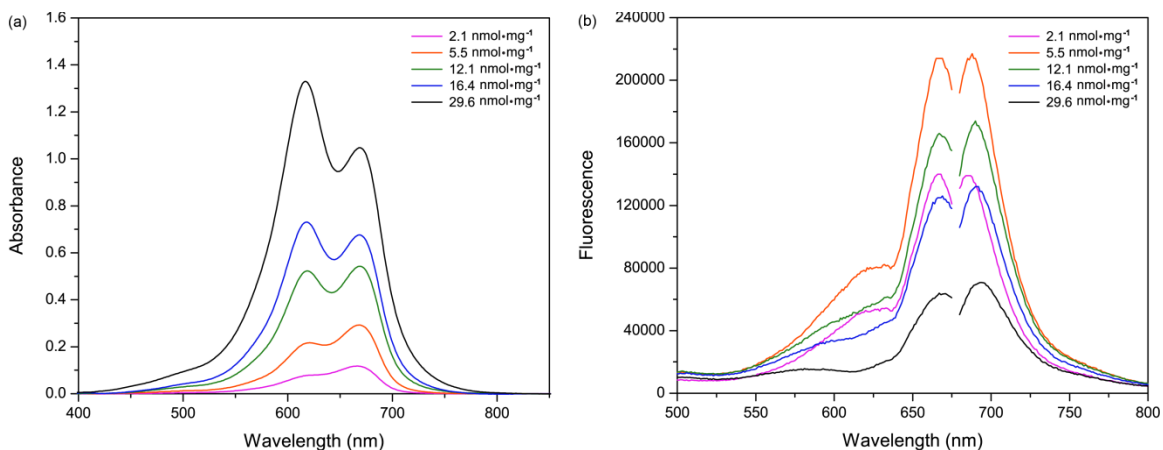
Figure 3-3 (a) Absorbance spectra of MB–PEGDMA PAA NPs, as function of matrix concentration; (b) Fluorescence excitation (left peak) and emission (right peak) spectra of MB–PEGDMA PAA NPs, λ_{ex} = 660 nm.

3.3.2 Advantages of MB–PEGDMA PAA NPs

According to our previous studies, the PAA nanomatrix protected the embedded MB molecules from undergoing reduction into a photo-inactive form, leuko-MB, due to an isomerization reaction catalyzed by bio-enzymes. [19,21] Although the MB–PEGDMA

PAA NPs may have a larger pore size, due to having longer chains and reduced amounts of cross-linker, we believe that the pore size is still small enough to prevent the enzymes from entering into the NP matrix — to prevent the embedded MB from reduction. The efficiency of protection of MB from reduction was tested for the MB–PEGDMA PAA NPs by the enzyme reduction test. While less than 20% of the fluorescence intensity of free MB remained in the presence of NADH and diaphorase, more than 90% of MB fluorescence intensity in the PEGDMA PAA NPs remained under the same conditions (Figure 3-4). The 8% of fluorescence decrease of MB–PEGDMA PAA NPs is presumably caused by the MBs conjugated onto the surface of the PEGDMA PAA NPs, which are not well protected by the matrix, while most of the conjugated MBs residing deeper inside the NPs are protected by the nanomatrix.
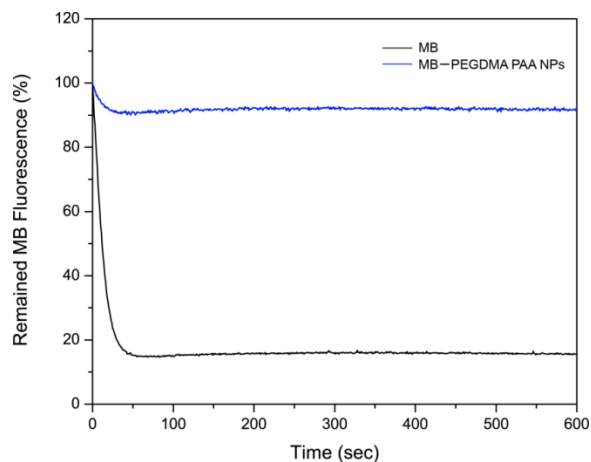
Figure 3-4 Enzyme reduction test of MB–PEGDMA PAA NPs: Free *vs* PAA encapsulated MB.

In addition, the MB–PEGDMA PAA NPs have an advantage based on optical considerations. In the PDT experiment, it is very important to optimize the local concentration of the photosensitizer in the blood stream, or inside organs since the absorbance maxima could change depending on the MB concentration, due to dimer

formation. [18] Hence, the *in vivo* production efficiency of ROS may be very different from the *in vitro* experimental value. In contrast with MB encapsulated in the nanomatrix, the PEGDMA PAA NPs attach their MB moieties by a conjugation method. MB–PEGDMA PAA NPs essentially keep the same distances between MBs even when varying the NP concentrations, since the distances among the MBs are fixed by the chemical bonds within the PAA chain. In Figure 3-5, the absorbance spectra of MB–PEGDMA PAA NPs do not change shape even at the higher NP concentrations. Thus one can maximize the PDT efficacy of MB at a high optimal concentration by the use of these NPs.
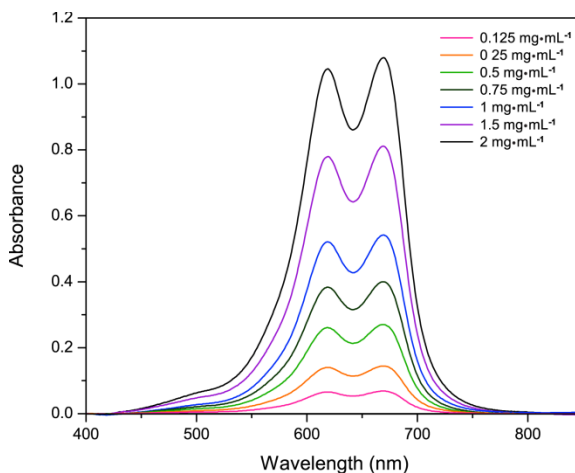
Figure 3-5 Absorbance spectra of MB–PEGDMA PAA NPs (12.1 nmol·mg^{-1} MB loading) with varying NP concentration. The absorbance peak of the MB dimer is at 619 nm and that of the monomer MB at 669 nm.

3.3.3 ROS Productivity Tests of MB–PEGDMA PAA NPs

Based on the k value test using ADPA, the ROS production efficiency of the MB–PEGDMA PAA NPs was estimated and compared with the previous MB–AHM PAA NPs (Figure 3-6). The k value increased with MB loading concentration up to 12.1

nmol·mg^{-1} of MB loaded PEGDMA PAA NPs, where $k = 13.4 \times 10^{-4}$ s^{-1}, and this k value maximum is 1.44 times higher than the maximum value found with MB–AHM PAA NPs, namely $k = 9.3 \times 10^{-4}$ s^{-1} at 8.8 nmol·mg^{-1} of MB loaded sample. [10] In addition, to compare the required amounts of conjugated MB between the two different NPs for producing the same amount of ROS, the MB–AHM PAA NPs were reproduced. [10] The MB–AHM PAA NPs containing 3.0 nmol·mg^{-1} of MB have a k value of 5.9×10^{-4} s^{-1} while the MB–PEGDMA PAA NPs containing only 2.1 nmol·mg^{-1} of MB produce a similar amount of ROS, i.e., with $k = 6.0 \times 10^{-4}$ s^{-1}. These improvements presumably originate from a reduced amount of longer cross-linker, which increases the distances between MBs, resulting in reduction of self-quenching while also providing a larger pore size, which allows for better oxygen permeation and lower collision probability between the produced ROS.

In Figure 3-6 (black line), the k value of the MB–PEGDMA PAA NPs decreases after peaking at 12.1 nmol·mg^{-1} of MB loading, which may result from too high MB loading within the limited space of the PAA NPs. It is necessary for the produced ROS to escape from the nanomatrix in order to kill the cancer cell or, in our measurements here, to react with the external ROS detection probe. However, the overproduced ROS species could react among themselves before getting out of the PAA NPs, so the amount of ROS outside the NPs may decrease, rather. Moreover, the excited photosensitizers could be self-quenched at the highly concentrated MB loading inside the limited space of the NPs, when those MB groups are close enough due to proximity of MBs in adjacent polymer chains.

Notably, the fluorescence emission spectra are determined by the amount of MB monomer, which is involved in producing $^1O_2$. [18] However, the k value dependence on the total MB loading does not follow the trend observed in the fluorescence spectra (Figure 3-3b) in a simple way. The highest fluorescence intensity of the NPs was obtained at 5.5 nmol·mg^{-1} of MB loading, not at the MB loading of the highest k value, which was 12.1 nmol·mg^{-1}. Furthermore, at 2.1 nmol·mg^{-1} of MB loading, the NPs have 2 times higher fluorescence intensity but 42% less k value than at 29.6 nmol·mg^{-1} of MB loading. For finer discrimination, so as to detect only the $^1O_2$, among all the ROS produced by the MB–PEGDMA PAA NPs, a singlet oxygen probe, SOSG was applied; SOSG reacts solely with $^1O_2$ but not with other ROS such as superoxide radical anion or hydroxyl radical. [29-31] In the presence of singlet oxygen, it emits an enhanced fluorescence at 525 nm. The SOSG can be activated in a DMSO and PBS (pH 7.4) solvent, in which a blank SOSG fluorescence spectrum was first taken, i.e., without $^1O_2$ generation from MB–PEGDMA PAA NPs. Then, with the NPs included, the enhanced SOSG fluorescence intensity, which is due to the presence of $^1O_2$, was taken, and the enhancement ratio was calculated, so as to give the "S value". In Figure 3-6 (blue line), it can be seen that the maximal amount of $^1O_2$ was produced at a loading of 5.5 nmol·mg^{-1} MB in PEGDMA PAA NPs. Also, the relationship between the fluorescence of MB–PEGDMA PAA NPs and the S value was quite linear, which supports the hypothesis that $^1O_2$ is produced overwhelmingly by the MB monomer, but not by the MB dimer (Figure 3-7). Due to the small size of the ADPA and SOSG molecules, these dyes can penetrate into the nanoparticles and detect the ROS inside the PAA NPs platform. Because of this, the k and S values can be overestimated due to detecting the ROS generated inside NPs.

However, the overestimation equally applies to all the tested NPs and the relative k and S values should not be affected. Thus, this potential overestimation will not distort the general trend of k and S values observed with various MB loadings in PAA NPs.
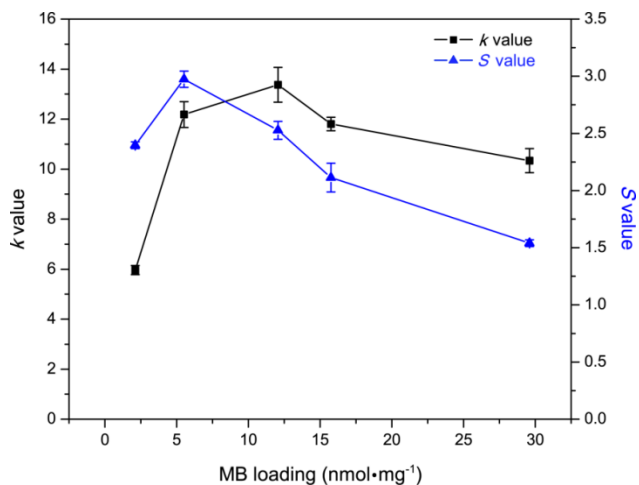
Figure 3-6 The k and S values of MB–PEGDMA PAA NPs depend on the amount of loaded MB. Black line: k value obtained by ADPA, Blue line: S value obtained by SOSG dye.
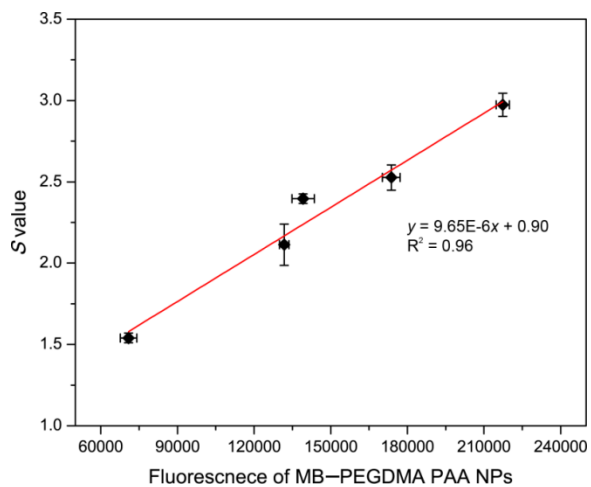
Figure 3-7 Correlation of S value with fluorescence emission intensity of MB–PEGDMA PAA NPs based on Figure 3-3b.

To find out the relationship of the k value and S value with the PDT effect of the MB–PEGDMA PAA NPs, the ROS producing routes of MB were investigated. Baptista's

group reported that not only the MB monomer but also the MB dimers produce specific ROS, through two major photochemical pathways, Type I and II (Scheme 3-2). [18,35-37] The MB monomer produces $^1O_2$ by energy transfer to the oxygen molecule from the triplet excited state MB ($^3MB^{+*}$), Type II, while at the higher MB concentration, the dimer MB (($MB)_2^{2+}$) produces semireduced MB radicals ($MB^•$) by redox suppression of excited ground sate dimers, and the $MB^•$ is oxidized to produce superoxide, Type I. Therefore we can explain why the higher MB loaded NPs (12.1, 15.8, 29.6 nmol·mg^{-1}) had a higher overall ROS production, compared to the lower MB loading case; the increase in superoxide radical production also affects the ADPA quenching rate, which reflects a weighted total ROS count, even though the production of $^1O_2$ decreases.
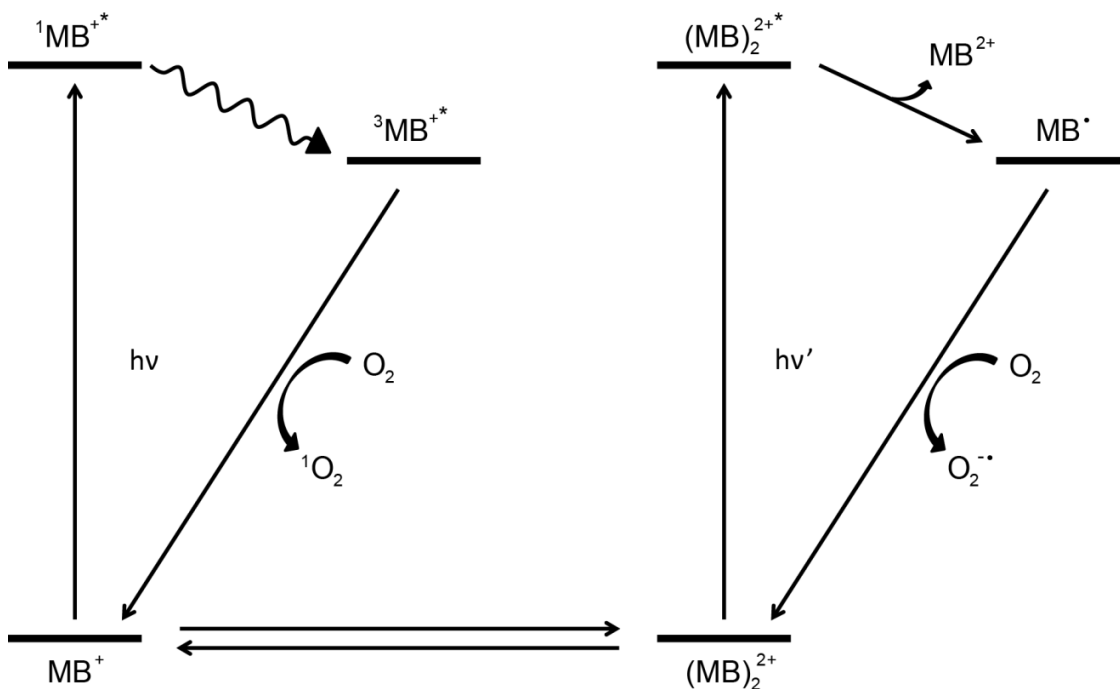
Scheme 3-2 Schematic ROS producing routes of MB: MB monomer produces singlet oxygen (Type II) while MB dimer produces superoxide (radical anion) (Type I). Note: Energy levels not drawn to scale.

3.3.4 PDT Efficacy Test Using Microfluidic Chips

To find out the relationship of ROS productivity based on the k and S values with the actual cell killing efficacy, an *in vitro* PDT test was performed using microfluidic chips. The chip was divided into four equal parts to increase throughput per test and it was illuminated homogeneously by the same light source. Through a gray scale test of the microfluidic chip's bright field image, the homogeneity of the LED light illumination was confirmed for the microfluidic chip under test. The averaged gray scale exhibited a very similar intensity, around 2300 (arbitrary units) for each quadrant in the microfluidic chip (Figure 3-8). In Figure 3-9, it shows cell survival data, for three different MB loadings, under a fixed NP concentration of 0.2 mg·mL^{-1}, based on a live/dead cell assay, as a function of light illumination time. The MB–PEGDMA PAA NPs of the three different MB loadings (2.1, 5.5 and 12.1 nmol·mg^{-1}) were investigated vs. a control of C6 cells without any NP treatment. Notably, based on "0 min" and "control" cases, no cell death was induced by light without NPs, nor by NPs without light. The k and S values exhibit significantly different trends in the MB loading range of 5.5 to 12.1 nmol·mg^{-1}. As expected for this loading range, the 2.1 nmol·mg^{-1} MB loaded NPs which have the lowest k and S values among three samples took the longest times, 21 min, to kill all of the C6 cells. In addition, with the 5.5 nmol·mg^{-1} of MB loaded NPs, it took 12 min to kill the C6 cells, but only 9 min was taken for killing most of the cells when using the 12.1 nmol·mg^{-1} of MB loaded NPs (Figure 3-9a). This trend clearly corresponds with the k value, not the S value, and is expected since not just the $^1O_2$ but also the superoxide radical anion contributes to the killing of the cells. [18,38] In addition, the half maximal inhibitory time (IT$_{50}$), needed to kill the C6 cells, was calculated for each batch of NPs

based on Figure 3-9b, and it shows a linear relationship with the k value (Figure 3-10). This supports the hypothesis that the relative trend of the detected k values is not distorted by potential overestimation of the absolute values. Using this trend, the IT_{50} for different MB loaded NPs could be estimated.
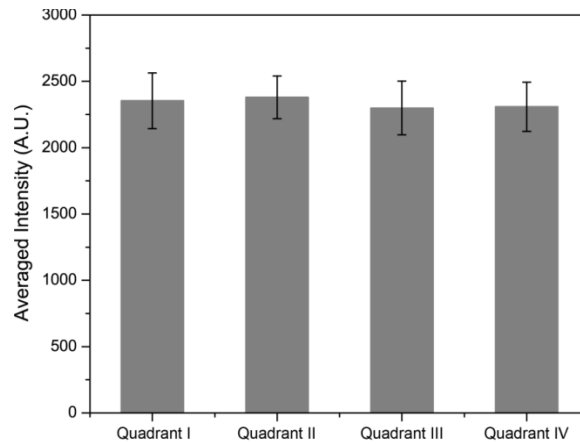
Figure 3-8 Averaged bright field image intensity on microfluidic chip illuminated by LED light source. Overall grayscale intensities in each quadrant of the chip were obtained and averaged.
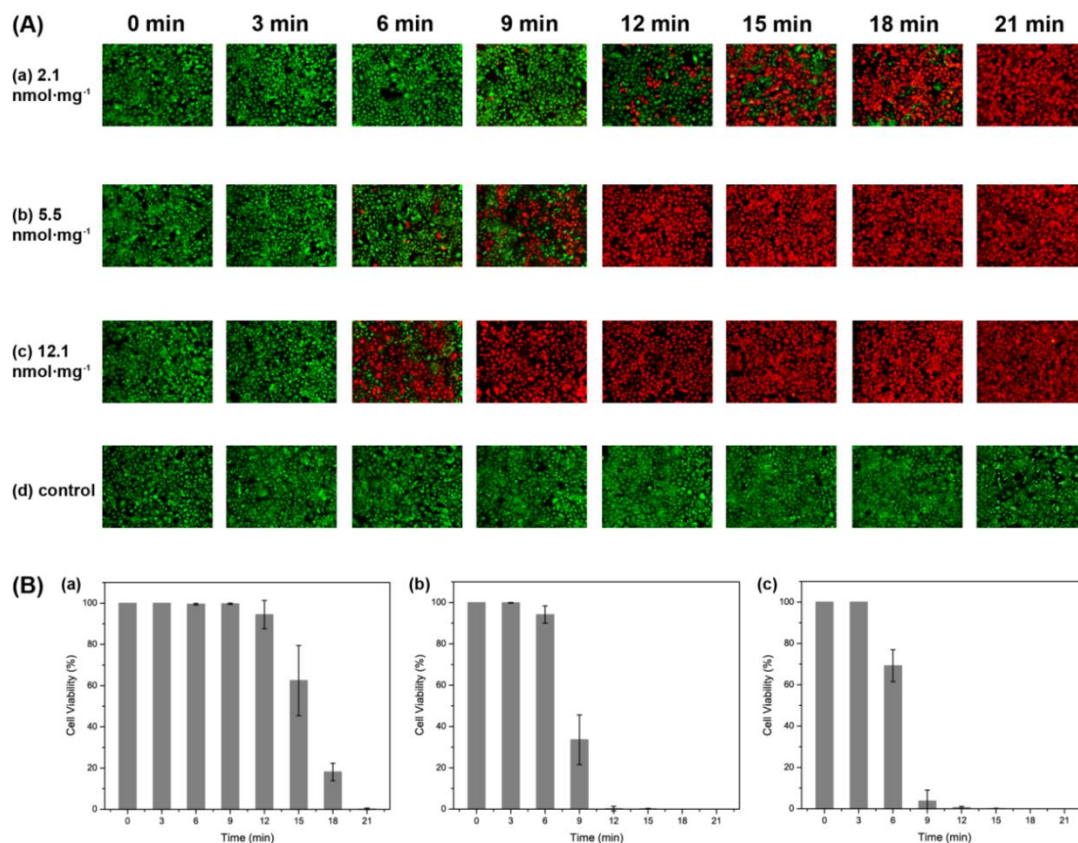
Figure 3-9 (A) Fluorescence images, with calcein AM and ethidium homodimer-1, for determining the viability of C6 cells, after PDT treatment using MB−PEGDMA PAA NPs, with varied MB concentration (2.1, 5.5, 12.1 nmol·mg^{-1}) and illumination time (0 − 21 min). The green color identifies a live cell (calcein AM) and the red color a dead cell (ethidium homodimer-1); (B) Cell viability (%) of A (a-c) based on eq. 1 ($n = 3$).
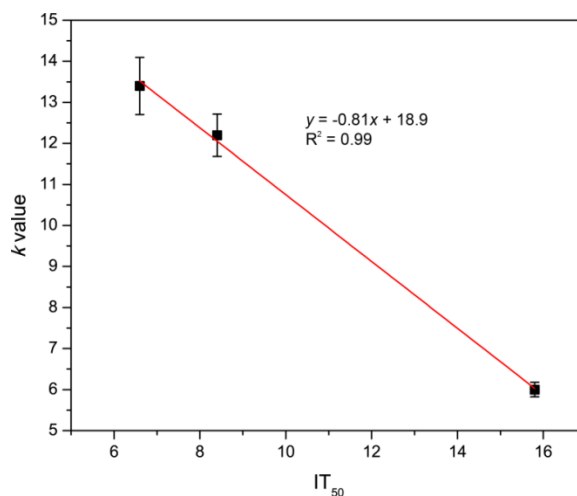
Figure 3-10 Relationship between IT$_{50}$ and k value of MB−PEGDMA PAA NPs.

3.4 Conclusions

In summary, a revision in synthetic approach of MB loaded PAA NPs coupled with improved analytical methods resulted in more efficient PDT. The PEGDMA cross-linked PAA NPs were designed for a higher PDT efficacy. Because of the longer cross-linker, PEGDMA, this novel NP matrix provides an increased distance among the conjugated MB photosensitizer groups, so as to control/minimize the aggregation of MB moieties inside the NPs reducing collision probability among the produced ROS and providing higher oxygen permeability. Such control of aggregation can serve as a tuning mechanism for the produced ROS mixture. At the same time, the PEGDMA PAA NPs matrix prevents any leaching out of the MB photosensitizer; protects it from reduction by plasma enzymes as tested in the presence of NADH with diaphorase even with increased pore size, and also preserves its spectral shape at both low and high concentrations.

The ROS productivity was measured using both k and S values, respectively obtained from the ROS sensitive ADPA probe and from the singlet oxygen sensitive SOSG probe. An excellent correlation was found between the MB *monomer* fluorescence peak intensity and the *singlet oxygen* production (S value), as well as between the k value and the total ROS production. Based on the k value, 1.44 times more ROS was produced by the new MB–PEGDMA PAA NPs, relative to the previous generation's MB–AHM PAA NPs, when comparing them at the most optimized MB loading for each NP. In addition, using the MB–PEGDMA PAA NPs saves 30% of the costly MB-SE needed to produce the same yield of ROS ($k = 6.0 \times 10^{-4}$ s^{-1}) with the 3.0 nmol·mg^{-1} MB loaded AHM PAA NPs.

A microfluidic device optimized for *in vitro* PDT was developed so as to enable reliable quantitative measurements of the PDT efficacy of MB–PEGDMA PAA NPs. Because of the small size of the chip, the LED illumination could be provided homogeneously, making it possible to reliably compare several different NPs simultaneously. The highest measured k value for the MB–PEGDMA PAA NPs, $k = 13.4 \times 10^{-4}$ s^{-1} (at 12.1 nmol·mg^{-1} MB loading), correlates with the most rapid killing of the C6 cancer cells (IT$_{50}$ = 6.6 min) and a linear relationship was found between this traditional k value and the IT$_{50}$ for PDT cell killing. This confirms the accepted, but sometimes overlooked, notion that PDT is not just due to singlet oxygen, but a result of various ROS, and that the ROS composition/mix may be important, as well as the ability of tuning this composition/mix.

3.5 Acknowledgments

3.6 References

(1)   Koo Lee, Y. E.; Kopelman, R. *Biomedical Nanoetechnology: Methods and Protocols*; Methods in Molecular Biology Series; Springer: New York, 2011, Vol. *726*, p151.

(2)   Garland, M. J.; Cassidy, C. M.; Woolfson, D.; Donnelly, R. F. *Future Med. Chem.* **2009**, *1*, 667.

(3)   Kim, S.; Ohulchanskyy, T. Y.; Bharali, D.; Chen, Y. H.; Pandey, R. K.; Prasad, P. N. *J. Phys. Chem. C* **2009**, *113*, 12641.

(4)   Dougherty, T. J.; Gomer, C. J.; Henderson, B. W.; Jori, G.; Kessel, D.; Korbelik, M.; Moan, J.; Peng, Q. *J. Natl. Cancer Inst.* **1998**, *90*, 889.

(5)   Chatterjee, D. K.; Fong, L. S.; Zhang, Y. *Adv. Drug. Delivery Rev.* **2008**, *60*, 1627.

(6)   Avula, U. M.; Kim, G.; Lee, Y. E.; Morady, F.; Kopelman, R.; Kalifa, J. *Heart Rhythm* **2012**, *9*, 1504.

(7)   Sibata, C. H.; Colussi, V. C.; Oleinick, N. L.; Kinsella, T. J. *Braz. J. Med. Biol. Res.* **2000**, *33*, 869.

(8)   Konopka, K.; Goslinski, T. *J. Dent. Res.* **2007**, *86*, 694.

(9)   Gursoy, H.; Ozcakir-Tomruk, C.; Tanalp, J.; Yilmaz, S. *Clin. Oral Invest.* **2013**, *17*, 1113.

(10)   Hah, H. J.; Kim, G.; Lee, Y. E.; Orringer, D. A.; Sagher, O.; Philbert, M. A.; Kopelman, R. *Macromol. Biosci.* **2011**, *11*, 90.

(11)   Kostron, H. *Methods Mol. Biol.* **2010**, *635*, 261.

(12)   Zhang, J.; An, F.; Li, Y.; Zheng, C.; Yang, Y.; Zhang, X.; Zhang, X. *Chem Commun.* **2013**, *49*, 8072.

(13)   Lin, J.; Wang, S. J.; Huang, P.; Wang, Z.; Chen, S. H.; Niu, G.; Li, W. W.; He, J.; Cui, D. X.; Lu, G. M.; Chen, X. Y.; Nie, Z. H. *ACS Nano* **2013**, *7*, 5320.

(14)   Bechet, D.; Couleaud, P.; Frochot, C.; Viriot, M. L.; Guillemin, F.; Barberi-Heyob, M. *Trends Biotechnol.* **2008**, *26*, 612.

(15)   Simon, T.; Boca-Farcau, S.; Gabudean, A. M.; Baldeck, P.; Astilean, S. *J. biophotonics* **2013**, *6*, 950.

(16)   Yan, F.; Zhang, Y.; Kim, K. S.; Yuan, H. K.; Vo-Dinh, T. *Photochem. Photobiol.* **2010**, *86*, 662.

(17)   Wilson, B. C.; Patterson, M. S. *Phys. Med. Biol.* **2008**, *53*, R61.

(18)   Tardivo, J. P.; Del Giglio, A.; de Oliveira, C. S.; Gabrielli, D. S.; Junqueira, H. C.; Tada, D. B.; Severino, D.; Turchiello, R. D. F.; Baptista, M. S. *Photodiagn. Photodyn.* **2005**, *2*, 175.

(19)   Tang, W.; Xu, H.; Park, E. J.; Philbert, M. A.; Kopelman, R. *Biochem. Bioph. Res. Commun.* **2008**, *369*, 579.

(20)   Tang, W.; Xu, H.; Kopelman, R.; Philbert, M. A. *Photochem. Photobiol.* **2005**, *81*, 242.

(21)   Qin, M.; Hah, H. J.; Kim, G.; Nie, G.; Lee, Y. E.; Kopelman, R. *Photochem. Photobiol. Sci.* **2011**, *10*, 832.

(22)   Wang, S.; Kim, G.; Lee, Y. E.; Hah, H. J.; Ethirajan, M.; Pandey, R. K.; Kopelman, R. *ACS nano* **2012**, *6*, 6843.

(23)   Wang, S. Y.; Fan, W. Z.; Kim, G.; Hah, H. J.; Lee, Y. E. K.; Kopelman, R.; Ethirajan, M.; Gupta, A.; Goswami, L. N.; Pera, P.; Morgan, J.; Pandey, R. K. *Laser Surg Med* **2011**, *43*, 686.

(24)   Yoon, H.; Ray, A.; Koo Lee, Y. E.; Kim, G.; Wang, X.; Kopelman, R. *J. Mater. Chem. B* **2013**, *1*, 5611.

(25)   Moreno, M. J.; Monson, E.; Reddy, R. G.; Rehemtulla, A.; Ross, B. D.; Philbert, M.; Schneider, R. J.; Kopelman, R. *Sens. Actuators, B* **2003**, *90*, 82.

(26)   Lou, X.; Kim, G.; Koo Lee, Y. E.; Kopelman, R.; Yoon, E. *International Conference on Miniaturized Systems for Chemistry and Life Sciences (MicroTAS'10)*; Groningen, The Netherlands, Oct 3-7, **2010**; Chemical and Biological Microsystems Society: San Diego, CA, 2010; p719

(27)   Lou, X.; Kim, G.; Koo Lee, Y. E.; Kopelman, R.; Yoon, E. *International Conference on Miniaturized Systems for Chemistry and Life Sciences (MicroTAS '11)*; Seattle, WA, Oct 2-6, 2011; Chemical and Biological Microsystems Society: San Diego, CA, 2011, p2058.

(28)   Wang, J.; Zhu, G.; You, M.; Song, E.; Shukoor, M. I.; Zhang, K.; Altman, M. B.; Chen, Y.; Zhu, Z.; Huang, C. Z.; Tan, W. *ACS Nano* **2012**, *6*, 5070.

(29)   Xiao, L.; Gu, L.; Howell, S. B.; Sailor, M. J. *ACS Nano* **2011**, *5*, 3651.

(30)   Lin, H. Y.; Shen, Y.; Chen, D. F.; Lin, L. S.; Wilson, B. C.; Li, B. H.; Xie, S. S. *J. Fluoresc.* **2013**, *23*, 41.

(31)   Flors, C.; Fryer, M. J.; Waring, J.; Reeder, B.; Bechtold, U.; Mullineaux, P. M.; Nonell, S.; Wilson, M. T.; Baker, N. R. *J. Exp. Bot.* **2006**, *57*, 1725.

(32)   Ilic-Stojanovic, S. S.; Nikolic, L.; Nikolic, V.; Stankovic, M.; Stamenkovic, J.; Mladenovic-Ranisavljevic, I.; Petrovic, S. *Chem. Ind. Chem. Eng. Q.* **2012**, *18*, 1.

(33)   Karamchand, L.; Kim, G.; Wang, S.; Hah, H.; Ray, A.; Jiddou, R.; Koo Lee, Y. E.; Philbert, M.; Kopelman, R. *Nanoscale* **2013,** *5*, 10327.

(34)   Patil, K.; Pawar, R.; Talap, P. *Phys. Chem. Chem. Phys.* **2000**, *2*, 4313.

(35)   Severino, D.; Junqueira, H. C.; Gugliotti, M.; Gabrielli, D. S.; Baptista, M. S. *Photochem. Photobiol.* **2003**, *77*, 459.

(36)   Junqueira, H. C.; Severino, D.; Dias, L. G.; Gugliotti, M. S.; Baptista, M. S. *Phys. Chem. Chem. Phys.* **2002**, *4*, 2320.

(37)   Gabrielli, D.; Belisle, E.; Severino, D.; Kowaltowski, A. J.; Baptista, M. S. *Photochem. Photobiol.* **2004**, *79*, 227.

(38)   Auten, R. L.; Davis, J. M. *Pediatr. Res.* **2009**, *66*, 121.

CHAPTER 4
PHOTO-MODULATION OF HEART RHYTHM: CELL SELECTIVE ARRHYTHMIA ABLATION USING TARGETED NANOPLATFORMS

4.1 Introduction

Heart disease is the primary cause of death in developed countries, and is overwhelmingly correlated with rhythm anomalies, *i.e.*, arrhythmias. [1,2] The heart rhythm and its failures are controlled by myocytes which account for 2-3 billion cells in each heart. [3] The cardiac myocytes are the excitable cells that form an electrical syncytium and enable heart contraction and dilation. [4] Other cells include 1) fibroblasts and other connective tissue cells, 2) nerve cells, 3) smooth muscle and endothelial cells of the coronary vasculature and endocardium, 4) mast cells as well as stem cells and pericytes. [3,5]

Disturbances of the myocyte-generated electrical impulse may result in the formation localized self-perpetuating arrhythmia sources. [6] Most arrhythmias are associated with substantial morbidity and mortality and represent an ever-growing therapeutic challenge. Arrhythmia management generally includes either anti-arrhythmic drugs and/or interventional procedures, such as surgery and catheter ablation. [7,8] In the last decades, catheter ablation has emerged as a common procedure employed in the hospital setting. Ablation technologies implement ablative energy delivered locally to cardiac regions harboring electrical sources of arrhythmia. Energies commonly employed are radiofrequency, cryoenergy, light amplification by stimulated emission of radiation (LASER), or ultrasound. Understandably, the resultant cellular damage from current

ablation technique is highly unspecific; all bystander cells are damaged along with the myocytes. [9] In addition, the catheter ablation technique is complex and difficult, and carries with it many risks, such as atrioesophageal fistula, pulmonary veins stenosis, coronary artery injury, tissue edema, thrombus formation and steam. [10-14]

To overcome the disadvantages of the existing catheter ablation technique, we have developed a nanoplatform enabled photodynamic therapy (PDT) which is a clinically approved localized phototherapy which has been tested for several medical conditions, especially cancer diseases. [15] During the PDT treatment, the photosensitizer, excited by illumination from an appropriate wavelength light source (e.g., laser), produces cytotoxic reactive oxygen species (ROS), resulting in tissue damage. [15,16] In a previous *in vitro* study, 50-60 nm sized methylene blue (MB) loaded polyacrylamide nanoparticles (MB–PAA NPs) were prepared as a PDT nano-drug and showed high efficacy in killing cancer cells. [17] Furthermore, conjugating the cardiac targeting peptide (CTP) to these NPs, cell selectivity was achieved *in vitro*, *i.e.*, killing only the myocytes, but not the fibroblasts. [9] However, *in vivo*, the size of the cardiac capillary vessels' fenestrations (pores) is highly limited (range 6-25 nm). [18-21]

Thus, a new nanoplatform had to be engineered, so as to have the ability to pass through the *in vivo* heart endothelial structure and be delivered to cardiac myocytes. Among available biocompatible materials, we chose the FDA (Food and Drug Administration) approved polyethylene glycol (PEG) material, with its low toxicity, enhanced plasma circulation time, reduced proteins fouling and chemical versatility. [22-24] We adapted a star shaped 8-arm PEG supramolecule so as to enable the attachment of Chlorin e6 (Ce6), and multiple moieties of CTP, to a single PEG macromolecule in order

to achieve both therapeutic and targeting functionalities. [25,26] A photosensitizer, Ce6 is a natural product derived from the chlorella species and has high optical absorption in the near infrared, a wavelength which deeply penetrates into living tissues. [27,28] The CTP, a nontoxic 12 amino acid targeting moiety (APWHLSSQYSRT), provides cell targeting specificity for myocytes. [9]

In this chapter, we report on 1) a synthetic strategy to prepare the CTP modified Ce6 conjugated 8-arm PEG nanoplatform (CTP–Ce6–PEG) and its characterization; 2) successful selective myocyte killing by *in vitro* PDT; and 3) CTP–Ce6–PEG targeting to the myocytes in a live rat, as well as selective cardiac ablation by *in vivo* PDT on live hearts.

4.2 Experimental Section

4.2.1 Materials

Materials. 8-arm polyethylene glycol-amine (8-arm PEG, 40 kDa and heterobifunctional polyethylenegylcol (Mal-PEG-NHS, 2 kDa) were purchased from Creative PEG Works. *N,N′*-dicyclohexylcarbodiimide (DCC), *N*-hydroxysuccinimide (NHS), *N,N*-dimethylformamide (DMF), phosphate buffered saline (BioReagent, pH 7.4, for molecular biology), bovine serum albumin (BSA) medium 199 (M199), sodium chloride (NaCl), potassium chloride (KCl), 4-(2-hydroxyethyl)-1-piperazineethanesulfonic acid (HEPES), potassium phosphate dibasic anhydrous (K_2HPO_4), magnesium sulfate ($MgSO_4$), glucose, calcium chloride ($CaCl_2$) glutathione, sodium bicarbonate ($NaHCO_3$) and Monoclonal Anti-Vimentin−Cy3 antibody were all purchased from Sigma-Aldrich. Chlorin e6 (> 95%, 596.67 Da) was purchased from

Frontier Scientific. Cardiac targeting peptide with cysteine attached (CTP−Cys, APWHLSSQYSRTC, > 95%, 1535.7 Da) was purchased from RS synthesis. Anthracene-9,10-dipropionic acid disodium salt (ADPA), calcein AM, propidium iodide (PI), penicillin-streptomycin, Dulbecco's Modified Eagle Medium (DMEM), 4′,6-diamidino-2-phenylindole (DAPI) and 0.05% trypsin-EDTA were purchased from Life Technologies. Blebbistain was purchased from Cayman Chemical. Collagenase II was purchased from Worthington Biochemicals. Anti-heavy chain cardiac Myosin antibody (clone # 3-48) and Alexa fluor 488 were purchased from abcam. The water was purified with a Milli-Q system from Millipore. All chemicals were used without further purification.

4.2.2 Synthesis of the Nanomatrix

Preparation of Ce6 conjugated 8-arm PEG (Ce6–PEG). The Ce6 was conjugated to amine groups of the 8-arm PEG through DCC and NHS coupling. The 448 µL of Ce6 solution (20 mg·mL^{-1} in DMF) was activated with 154.8 µL of DCC (20 mg·mL^{-1} in DMF) and 172.8 µL of NHS, 20 mg·mL^{-1} in DMF by stirring for 30 - 45 min. The 8-arm PEG solution (40 kDa, 20 mg·mL^{-1} in DMF) was prepared by stirring and sonicating until the entire 8-arm PEG was dissolved. The prepared NHS activated Ce6 solution was added into a PEG solution and stirred overnight. To remove unreacted Ce6, the crude product was washed with 60% ethanol, PBS (pH 7.4) and D.I. water using an Amicon filtration system (10 kDa filter membrane). After the washing, the Ce6–PEG was filtered by a 0.45 nm syringe filter and stored after freeze drying (Scheme 4-1).

Preparation of CTP targeted Ce6–PEG (CTP–Ce6–PEG). For the CTP targeting, 1.47 mL of MAL-PEG-NHS (100 mg·mL^{-1} in PBS (pH 7.4)) was added into 5 mL of Ce6–PEG (20 mg·mL^{-1} in PBS (pH 7.4)) and stirred for 30 min. Using an Amicon

centrifugal cell (10 kDa), the unreacted MAL-PEG-NHS was washed out three times and the concentration of nanoplatform solution was diluted to 20 mg·mL^{-1} with PBS (pH 7.4). Then, 537 µL of CTP solution (100 mg·mL^{-1} in PBS (pH 7.4)) was added into the nanoplatform solution under constant stirring. After overnight, 0.43 mL of cysteine (10 mg·mL^{-1} in D.I. water) was added and stirred 1 h additionally. The mixture was washed with enough D.I. water through an Amicon centrifugal cell (10 kDa) and the final CTP–Ce6–PEG was obtained through freeze drying (Scheme 4-1).
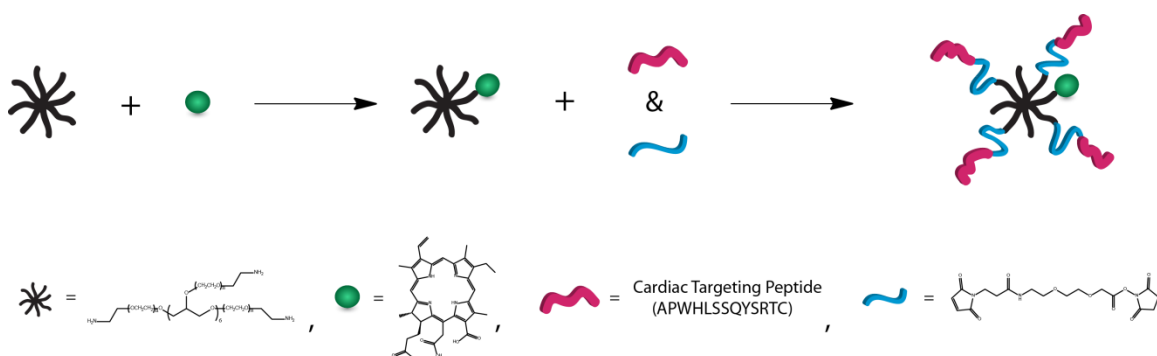
Scheme 4-1 Synthesis of CTP–Ce6–PEG nanoplatform.

4.2.3 Characterization

Absorbance & Fluorescence Measurements. To monitor the absorption and fluorescence spectrum of the nanomatrix, a UV-1601 UV-vis spectrometer (Shimadzu) and a FluoroMax-3 Spectrofluorometer (Jobin Yvon Horiba) were used. The nanomatrix solution was prepared (0.1 mg/mL) in PBS (pH 7.4). The measurements were conducted in triplicate.

Detection of ROS. The ROS produced from CTP–Ce6–PEG were measured based on a previously reported method. [29] To 2 mL of CTP–Ce6–PEG (0.1 mg·mL^{-1} in PBS (pH 7.4)), 80 µL of ADPA (100 µM in pure water) was added. The fluorescence of ADPA

75

(λ_{ex} = 370 nm) measured by a FluoroMax-3 Spectrofluorometer (Jobin Yvon Horiba), right after irradiation at 660 nm of the CTP–Ce6–PEG solution, over several time periods (0, 60, 120, 180, 240, 300, 480 and 660 sec), under constant stirring and temperature (25 °C). The decay constant of the ADPA fluorescence, the "k value" was calculated by the previously reported equation. [29]

4.2.4 Animal Tests

Isolation of Adult Rat Myocytes and Fibroblasts. Adult cardiomyocytes from normal adult male rats (200–300 g) were isolated as described before. [30] Briefly, after euthanasia, hearts were retrogradely perfused through the aorta for up to 5 minutes with modified Krebs-Henseleit buffer (KHB), containing NaCl (118 mM), KCl (4.8 mM), HEPES (25 mM), K_2HPO_4 (1.25 mM), $MgSO_4$ (1.25 mM), glucose (11 mM) and $CaCl_2$ (1 mM), at pH 7.40. The perfusate was then switched to modified a Krebs buffer without calcium for 3 minutes. Following the calcium-free KHB perfusion, hearts were digested by perfusing calcium-free KHB containing 200 units/ml collagenase II, and blebbistatin (33.3 μM) for 15 min. The collagenase digested hearts were removed from the apparatus and the tissue was minced gently to separate out the cells. The suspension was centrifuged (500×g) for 30 sec, and the cell pellet was resuspended in KHB-A containing 2% bovine serum albumin and blebbistatin. The cell suspension was centrifuged again and resuspended in culture media (M199) containing glutathione (10 mM), $NaHCO_3$ (26 mM), 100 units·mL^{-1} penicillin, 100 μg·mL^{-1} streptomycin and 5% fetal bovine serum. Cells were plated on laminin coated (40 μg·mL^{-1}) tissue culture cover slips. After 2 h, the medium was changed to serum-free M199. Cell suspension supernatant from both spins was saved for fibroblast isolation. The suspended fibroblasts were centrifuged at 2000

rpm for 10 min, and the cell pellet was suspended in DMEM supplemented with 1% penicillin-streptomycin and 10% fetal bovine serum (full medium). Cardiac fibroblasts were grown in a similar full medium until 70–80% confluent and passaged using 0.05% trypsin EDTA.

In vitro **PDT Test.** The myocyte and fibroblast cells were co-cultured. The co-cultures were incubated with free Ce6 (0.0016 mg·mL^{-1}) or CTP–Ce6–PEG (0.1 mg·mL^{-1}) for 2 h and washed with PBS (pH 7.4) three times. Using a Nikon A1R confocal microscope (Nikon Instruments Inc.), the nanoplatforms were activated by laser illumination at 405 nm (7-10 mW) over 10 min. After the illumination, co-cultured cells were treated by calcein AM and PI, as a live-dead cell assay. The fluorescence images measured of calcein AM and PI were taken by confocal microscope.

Histology and Imaging. Immuno-fluorescence analysis was carried out on paraffin embedded tissue samples which were sectioned into slides. The following antibodies were used for the staining: 1) Myocytes - Anti-heavy chain cardiac Myosin antibody (clone # 3-48) with Alexa fluor 488 tagged secondary antibody, 2) Fibroblasts - Monoclonal Anti-Vimentin−Cy3 antibody (dilution 1: 100). DAPI was used to counterstain the nuclei. Primary and secondary antibodies were diluted in PBS (pH 7.4) plus 0.1% Triton X-100 and 5% donkey serum. Images were acquired using a Nikon A1R confocal microscope with sequential laser firing.

Open Chest Rat Model, Protocol and Analysis. All procedures were approved by the University of Michigan Committee on Use and Care of Animals and complied with the National Institutes of Health guidelines. We used male Sprague–Dawley rats weighing 200 to 250 g that were housed under conditions of controlled temperature and a

12 h light-dark cycle. The animals were anesthetized with ketamine (60 mg·kg^{-1} IP) and xylazine (6 mg·kg^{-1}), placed in dorsal recumbency, and then intubated and ventilated throughout the procedure with 100% humidified oxygen at 90 strokes·min^{-1} and 10 mL·kg^{-1} tidal volume. An extra dose of anesthetic (one third of the initial dose of ketamine) could be administered as needed at 45 min after the first dose to prolong anesthesia. Limb electrodes are placed and connected to an amplifier to record EKG continuously. With the animal in dorsal recumbency, the skin on the ventral thorax is shaved and disinfected and then is incised at the left thorax, lateral to the sternum near the third intercostal space. After incising intercostal muscle, the left atrium is exposed and held with the help of retractors. The animal is allowed to stabilize for 15 min. A bipolar electrode is placed on the left atrial appendage (LAA) and the amplitude is recorded. Then the laser (671 nm, 300 mW) light is directed onto the left atrial appendage for 4 minutes. This served as a control to evaluate the possible effects on the electrogram amplitude with laser illumination alone. Then, 2 mL of CTP–Ce6–PEG (50 mg·mL^{-1} in PBS (pH 7.4)) is injected into the tail vein. After 60 min, following CTP–Ce6–PEG injection, the laser is directed towards the LAA, and the changes in LAA electrogram amplitude recorded (Scheme 4-2). Rats were injected with a dead cell stain - propidium iodide (PI) - via the tail vein (40 mg·kg^{-1} body weights, in 1 mL PBS (pH 7.4)) for group 2. After the experiment, the animal is euthanized and the heart is stored in formalin for histological analysis. For LAA amplitude analysis, bipolar recordings were filtered to eliminate AC power noise (60 Hz IIR band stop). The amplitude from the baseline is derived for the atrial signal and measured as difference of voltage between negative peak and positive peak of single deflection.
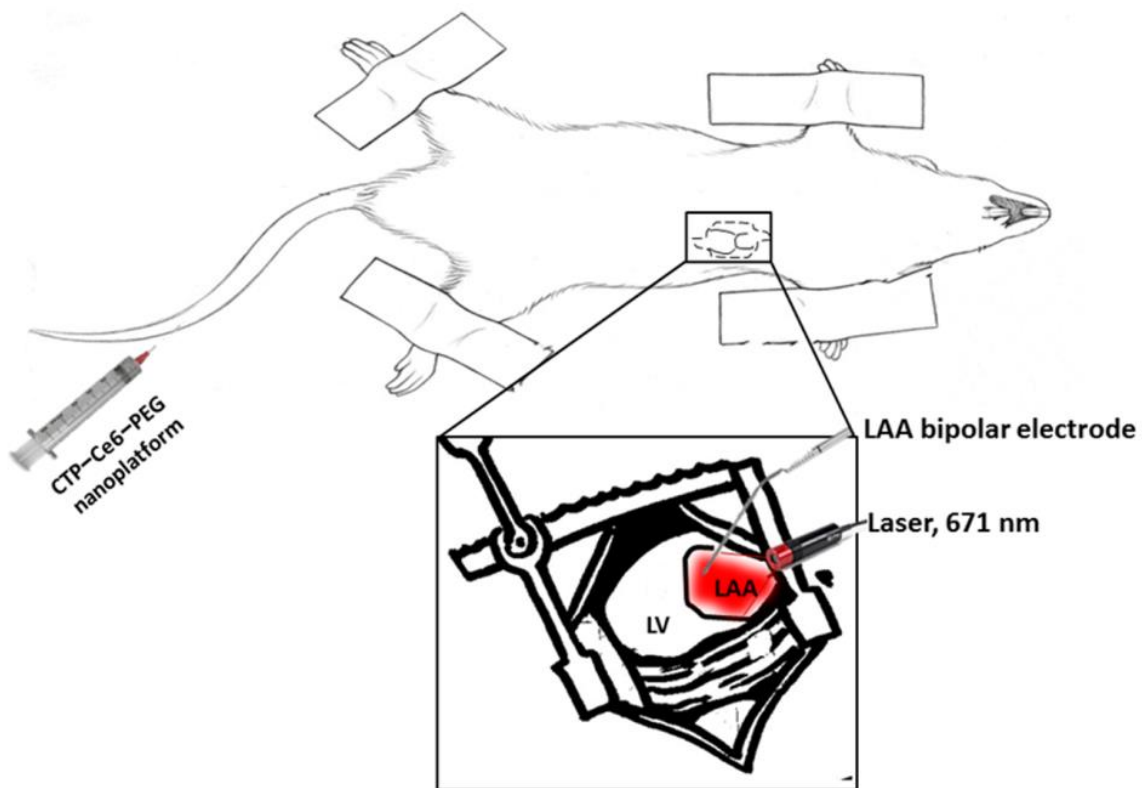
Scheme 4-2 Simplified scheme of the rat open chest PDT experimental set-up for *in vivo* PDT test.

4.3 Results and Discussion

4.3.1 Characteristics of the CTP–Ce6–PEG

CTP–Ce6–PEG absorbance and fluorescence spectra are shown in Figure 4-1, (a) and (b) respectively. In PBS (pH 7.4) buffer, free Ce6 has three absorption peaks, at 403 nm, 505 nm and 655 nm. In comparison, Ce6–PEG shows three shifted absorption peaks at 401 nm, 502 nm and 660 nm. In particular, the peak around 660 nm of Ce6–PEG indicates a significant red shift compared to free Ce6. The Ce6 content in the 8-arm PEG was calculated based on a free Ce6 absorbance calibration curve. It was found that 2.2 ($\pm$ 0.1) mg of Ce6 have been incorporated into 100 mg of Ce6–PEG molecules, so that an

average of about 1.5 ($\pm$ 0.1) molecules of Ce6 is conjugated per one 8-arm PEG nanoplatform. As shown in Figure 4-1b, free Ce6 excitation and fluorescence emission spectra appear at 655 nm and 660 nm (λ_{max}), while the Ce6–PEG peaks are shifted to 660 nm and 663 nm (λ_{max}), respectively. Both excitation maxima correspond to the analogous absorbance maxima, at around 660 nm, of the Ce6–PEG and free Ce6 solution. Importantly, the fluorescence emission of Ce6–PEG shows a higher intensity than free Ce6, with a similar Ce6 concentration.

The targeting moiety, CTP, was conjugated to the surface of the Ce6–PEG. After CTP conjugation, the absorbance and fluorescence spectra of 0.1 mg·mL^{-1} of CTP–Ce6–PEG decreased, presumably just due to its increased molecular weight (Figure 4-1). Based on the assumption that the entire bi-functional PEG was conjugated to CTP, the average number of CTPs per one PEG molecule was calculated from the ratio of the CTP–Ce6–PEG and Ce6–PEG absorbance spectra. Accordingly, an average of 4.4 ($\pm$ 1.2) CTP molecules was conjugated per one 8-arm PEG molecule, with an expected molecular weight of around 56.2 kDa. For the behavior of these nanoplatforms under biological conditions, the hydrodynamic size is very important, since the CTP–Ce6–PEG should be small enough to penetrate through the pores of the normal heart endothelial cell membrane. Following the hydrodynamic size dependence on the molecular weight for various proteins, the hydrodynamic size of the CTP–Ce6–PEG is estimated at 6.7 ($\pm$ 0.9) nm. [31,32] However, it shouldn't be overlooked that the CTP–Ce6–PEG, due to its star-shape, could have a smaller hydrodynamic size than linear proteins of the same molecular weight. [24]
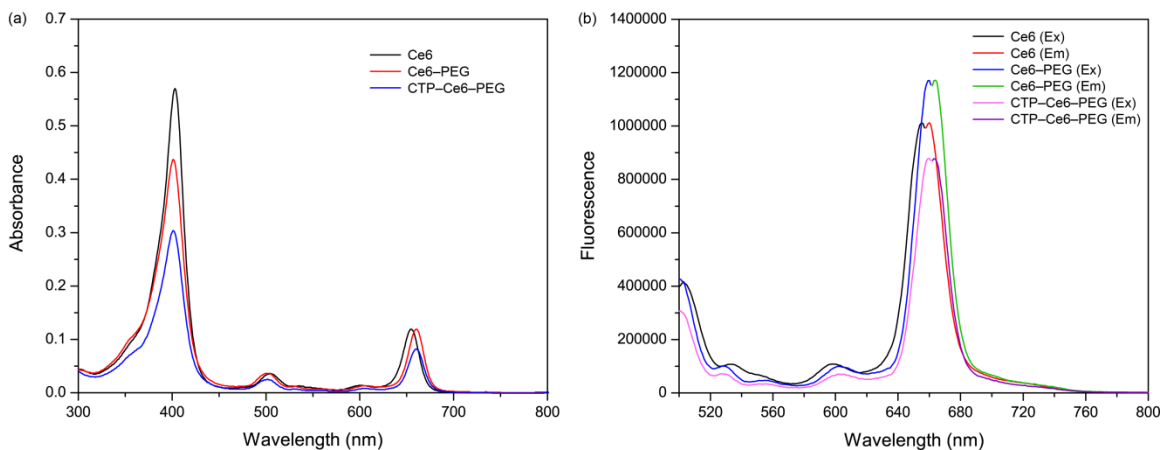
Figure 4-1 (a) Absorbance spectra CTP–Ce6–PEG; (b) Fluorescence excitation (left peak) and emission (right peak) spectra of CTP–Ce6–PEG, λ_{ex} = 660 nm.

To confirm the amount of produced ROS from the Ce6–PEG, the "*k* value" was determined by calculating the first order decay kinetics of the ADPA's oxidative quenching (Figure 4-2). [17,29] For 0.1 mg/mL of Ce6–PEG in PBS (pH 7.4), the *k* value was found to be 2.99×10^{-4}, but the *k* value for the same amount of free Ce6 in a test solution of Ce6–PEG was only 2.12×10^{-4}. This increase is presumably due to the bulkiness of the 8-arm PEG which helps to increase the distance between the fluorescent dye moieties; this may reduce the self-quenching rate of Ce6, thus increasing both the fluorescence yield (Figure 4-1b) and also the singlet oxygen productivity. We note that an about 4.5 times higher amount of ROS was produced from these Ce6–PEG nanoplatforms than from the same total nanoplatform mass of the previously reported MB–PAA NPs. [9,17]
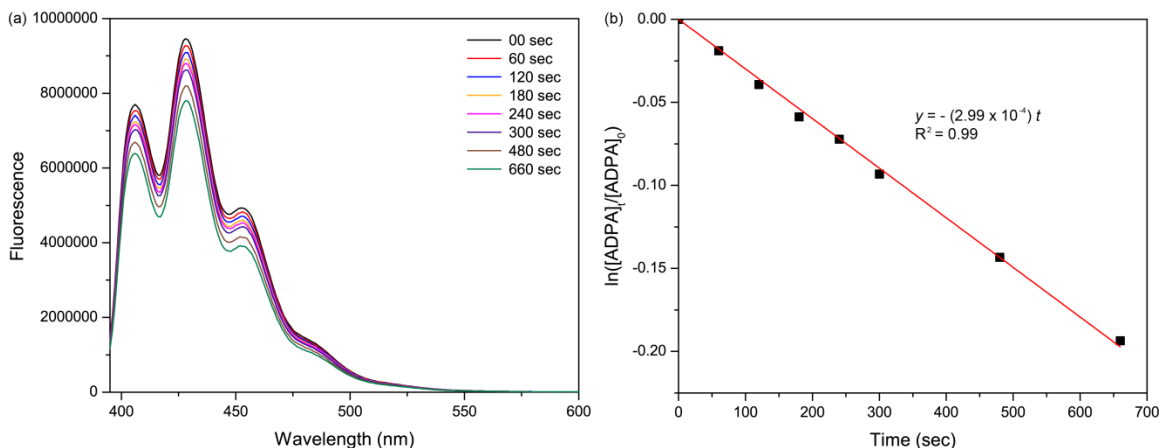
Figure 4-2 Efficiency of singlet oxygen production. Fluorescence spectra of ADPA with Ce6–PEG solution (left) and fluorescence change of ADPA with linear fitted graph dependence on irradiation time of Ce6–PEG, λ_{ex} = 660 nm.

4.3.2 *In Vitro* PDT of Cardiac Ablation Using CTP–Ce6–PEG

We first tested the cell specific *in vitro* PDT efficiency of the CTP–Ce6–PEG. Co-cultures of isolated adult rat ventricular myocytes and fibroblasts were obtained, as detailed in the experimental section. The cells in the co-culture were treated by PDT in a medium containing 0.0016 mg·mL^{-1} of free Ce6 or 0.1 mg·mL^{-1} of CTP–Ce6–PEG, in the presence of live/death indicator reagents, *i.e.*, calcein-AM, for designating live cells, and PI, for designating dead cells. Under laser illumination, for free Ce6, both myocytes and fibroblasts exhibited rapid morphological changes with progressively increasing PI uptake (red fluorescence) and vanishing calcein-AM staining (green fluorescene), clearly indicating cell death (Figure 4.3a). However, for CTP–Ce6–PEG, only myocytes exhibited rapid morphological changes, from a rod-like shape to a random shrunken shape with emerging red PI fluorescence; in contrast, the fibroblast showed no such changes (Figure 4-3b). In addition, even when two different cell types came into contact with each other, the myocyte selectivity of the PDT damage caused by the targeted CTP–Ce6–PEG nanoplatforms was still maintained (Figure 4-3b).
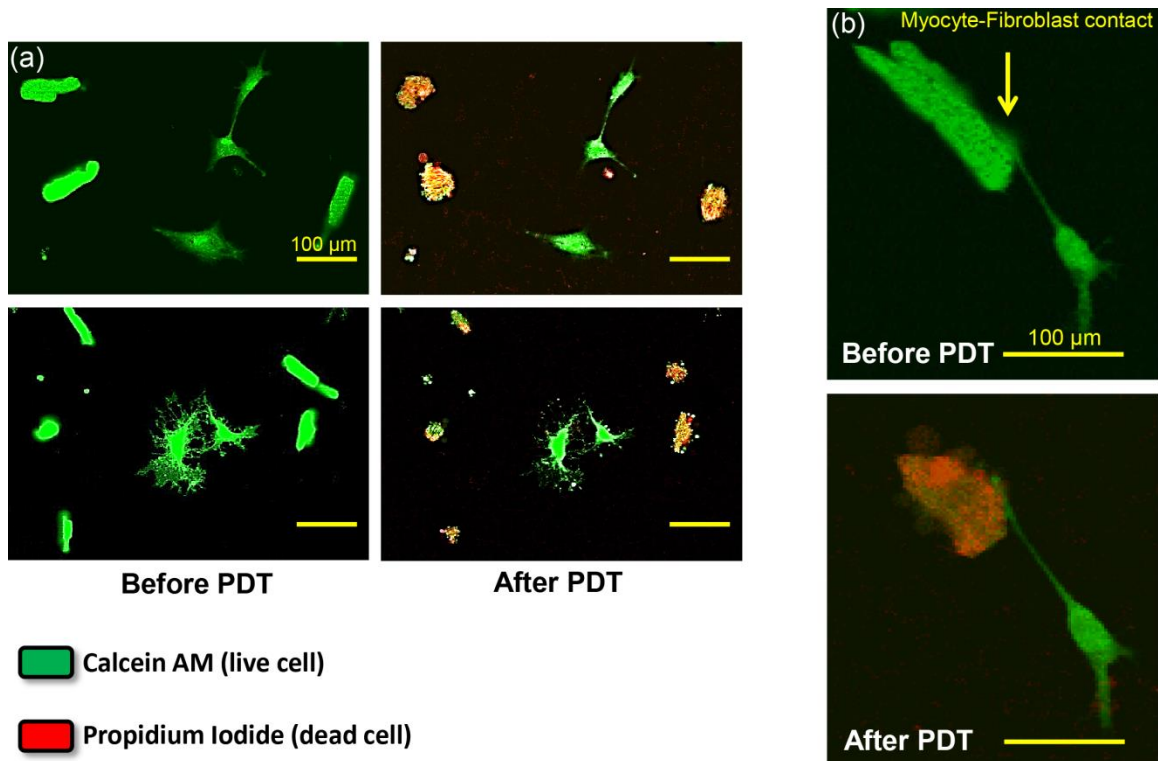
Figure 4-3 Targeted PDT in *in vitro* co-culture of primary adult rat ventricular myocytes and cardiac fibroblasts; (a) non-selective ablation of free Ce6; (b) selective myocyte ablation of CTP–Ce6–PEG; (c) selective myocyte ablation of CTP–Ce6–PEG for contacted two different cell types.

4.3.3 *In Vivo* PDT of Cardiac Ablation Using CTP–Ce6–PEG

We evaluated the ability of the CTP–Ce6–PEG to achieve myocytes-specific ablation *in vivo*. We injected nanoplatform samples into 2 groups of rats: to confirm CTP–Ce6–PEG delivery and myocyte-specific affinity (group 1) and to test myocyte-specific photo-ablation (group 2). All rats were injected via the tail vein, with CTP–Ce6–PEG (1.6 mg Ce6/rat).

In group 1, 1 h after injection of the nanoplatforms, the hearts were isolated and immuno-stained for myocytes and for fibroblasts, as described in the experimental section. From the co-localization study of confocal microscopy, the affinity of CTP–Ce6–PEG nanoplatforms towards myocytes, but not fibroblast, is clearly shown (Figure 4-4).

In Figure 4-4a, the image shows co-localized fluorescence of myocyte staining with Anti-heavy chain cardiac Myosin antibody (green), fibroblast staining with Monoclonal Anti-Vimentin-Cy3 antibody (yellow), Ce6 from CTP–Ce6–PEG (purple) and nucleus counterstaining with DAPI (blue). After removing (filtering out) the green color for myocyte staining, there was purple fluorescence observed, from the CTP–Ce6–PEG (Figure 4-4b). This stands for the CTP–Ce6–PEG that penetrated the heart endothelial structure and got attached to the myocytes. In Figure 4-4c, however, after filtering out the yellow fibroblast staining, we cannot observe any purple fluorescence from the CTP–Ce6–PEG in the previously yellow fluorescence locations of the fibroblast. Thus, this study clearly shows that the CTP–Ce6–PEG nanoplatform is small enough to pass the heart endothelial structure as well as showing the selective affinity of the CTP–Ce6–PEG nanoplatform towards only myocytes, but not towards fibroblasts.
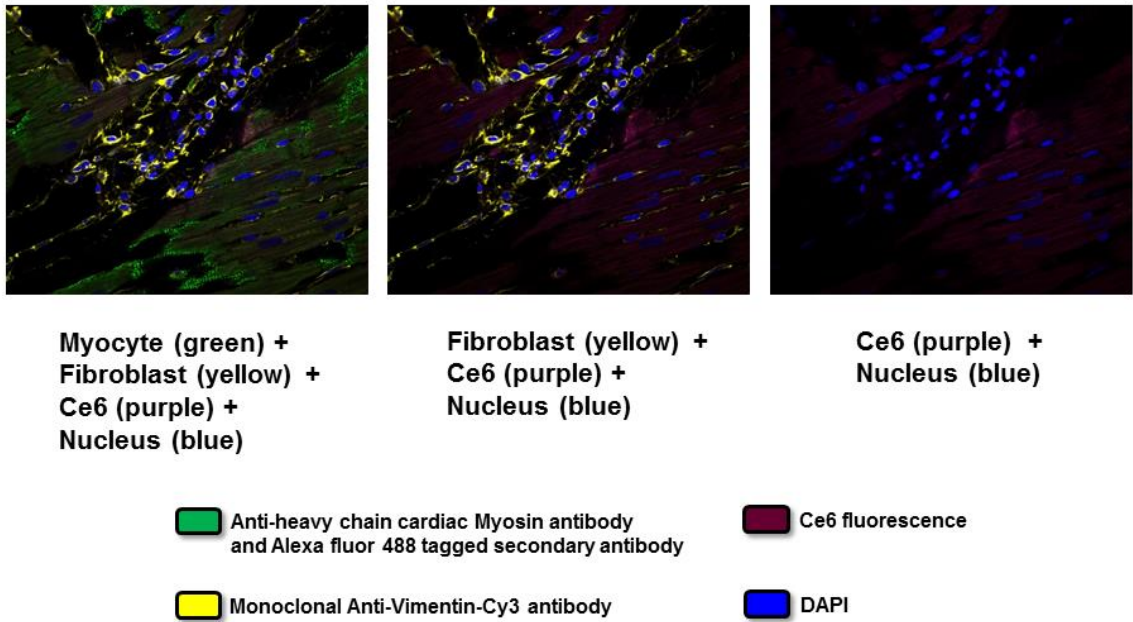
Figure 4-4 Myocyte specific targeting by CTP–Ce6–PEG nanoplatform.

In group 2, 1 h after CTP–Ce6–PEG injection, PDT ablation was performed in anesthetized rats. After left lateral thoracotomy and exposure of the left atrium, 300 mW of 671 nm LASER light was directed towards the left atrium, with 10-15 minutes of total illumination, Scheme 4-2. An LAA electrogram amplitude was continuously recorded during the experiment with a bipolar electrode positioned directly onto the LAA. Laser illumination led to rapid myocardial ablation as indicated by a progressive amplitude decrease in the LAA electrogram with local signal amplitude decreasing by about a factor of 6 after PDT (82.8 $\pm$7.3% decrease, $p < 0.05$, $n = 5$) (Figure 4-5a). Results were compared with the sham experiments (control), in which a similar protocol was followed but in the absence of CTP–Ce6–PEG injection; it was observed that the LAA local electrogram amplitude did not significantly change after laser illumination (9.08 $\pm$ 3.8% decrease, $p = 0.24$, $n = 5$) (Figure 4-5b).
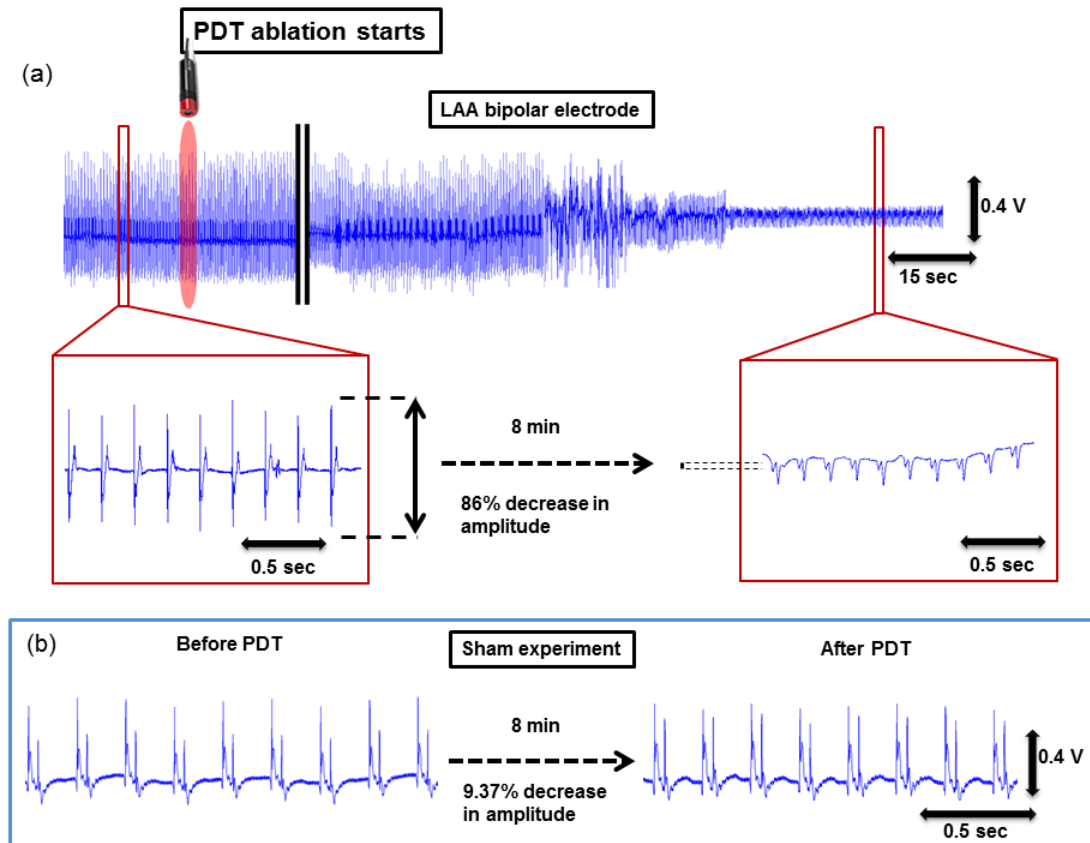
Figure 4-5 *In vivo* targeted photodynamic therapy and LAA electrogram amplitude recordings. After one hour of injecting CTP–Ce6–PEG, the laser (671 nm, 300 mW) light is shined on the LAA. The LAA electrogram amplitude is continuously recorded throughout the experiment, from a bipolar electrode placed directly on the LAA. (a) LAA electrogram with CTP–Ce6–PEG nanoplatforms; (b) LAA electrogram without nanoplatforms.

After cell specific PDT ablation, we used a histology study to determine whether only myocytes, not fibroblasts, were ablated by PDT. Figure 4-6 shows strong PI intensity (red fluorescence, dead cell staining) at the nuclei located at the center of myocytes (green fluorescence) for ablated sites, while strong DAPI (blue fluorescence, counterstaining) is observed at the nuclei of fibroblasts, which are non-ablated sites. The significant fluorescence intensity change of DAPI and PI between the nucleus of a fibroblast and a myocyte (from star mark to diamond mark) was graphically presented in Figure 4-6d. The fibroblasts could not be stained due to overlapping emission wavelength between

Monoclonal anti-vimentin-Cy3 antibody and PI. In this histology study, we confirmed that only myocytes were ablated by *in vivo* PDT, not fibroblast
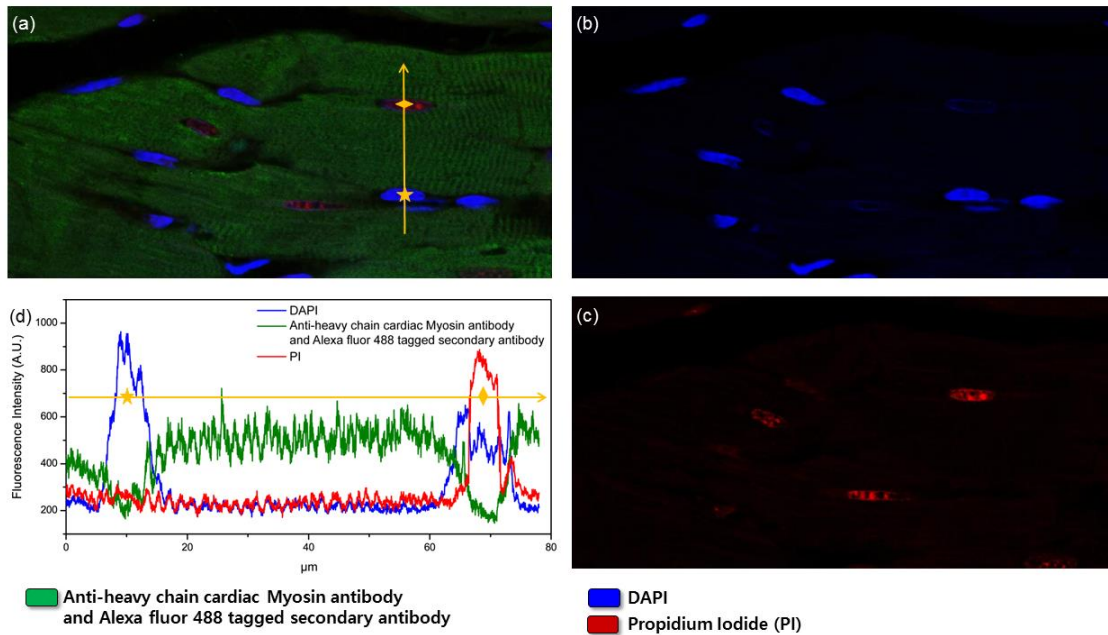
Figure 4-6 Enlarged confocal fluorescence image of ablation site after *in vivo* PDT. a) Co-localized fluorescence image for Anti-heavy chain cardiac Myosin antibody and Alexa fluor 488-tagged secondary antibody stained myocytes (green fluorescence), DAPI stained nuclei of unablated cells (blue staining), and PI stained nuclei of ablated cells (red staining); b) isolated fluorescence image of DAPI stained nuclei for unablated cells (fibroblast); c) isolated fluorescence image of PI stained nuclei for ablated cells (myocytes); and d) fluorescence intensity profiles for each of three color stainings along yellow arrow in Figure 4-6a.

4.4 Conclusions

The above results strongly support the feasibility of a myocyte-specific photo-ablation approach. The use of a myocyte-targeted PDT-enabled nanoplatform (CTP–Ce6–PEG), which satisfies several requirements for cardiac PDT: 1) small size, 2) hydrophilicity, 3) no dark toxicity, 4) facile multiple modifications (conjugating with both Ce6 and CTP) and 5) low price, has been shown as a sound approach for modulating the cardiac rhythm. For *in vitro* PDT, the new photo-drug nanoplatform, CTP–Ce6–PEG,

successfully targeted and killed only the myocytes. Furthermore, the CTP–Ce6–PEG is small enough to penetrate the cardiac capillary vessels' pores and the selective targeting ability of these nanoplatforms towards myocytes was retained during the *in vivo* PDT, in order to ablate myocytes while preserving the integrity of the bystander cells. Also, this work sets the stage for the development of similar 'alternative' approaches to common cardiac ablation. It has been suggested that nerve terminals or Purkinje myocytes play a critical role in arrhythmia initiation. [33-36] Still, with traditional methods, it is nearly impossible to target these structures without affecting other cardiac cells. Potentially, treatment similar to our cell-specific technology could be implemented in well-defined clinical scenarios, as a stand-alone or as an adjuvant therapy. In our view, cell-specific photo-ablation could advantageously complement current ablation systems, with the dual goal of decreasing procedure time and decreasing complications and thus increasing efficacy.

4.5 Acknowledgments

4.6 References

(1)   de Luna, A. B.; Coumel, P.; Leclercq, J. F. *Am. heart J.* **1989**, *117*, 151.

(2)   Huikuri, H. V.; Castellanos, A.; Myerburg, R. J. *New Engl. J. Med.* **2001**, *345*, 1473.

(3)   Tirziu, D.; Giordano, F. J.; Simons, M. *Circulation* **2010**, *122*, 928.

(4)   Kizana, E.; Ginn, S. L.; Allen, D. G.; Ross, D. L.; Alexander, I. E. *Circulation* **2005**, *111*, 394.

(5)   Bu, L.; Jiang, X.; Martin-Puig, S.; Caron, L.; Zhu, S.; Shao, Y.; Roberts, D. J.; Huang, P. L.; Domian, I. J.; Chien, K. R. *Nature* **2009**, *460*, 113.

(6)   Kleber, A. G.; Rudy, Y. *Physiol. Rev.* **2004**, *84*, 431.

(7)   Nattel, S. *Nature* **2002**, *415*, 219.

(8)   Labrova, R.; Spinar, J.; Honzikova, N. *Physiol. Res.* **2010**, *59 Suppl 1*, S43.

(9)   Avula, U. M.; Kim, G.; Lee, Y. E.; Morady, F.; Kopelman, R.; Kalifa, J. *Heart Rhythm* **2012**, *9*, 1504.

(10)   Shah, D.; Dumonceau, J. M.; Burri, H.; Sunthorn, H.; Schroft, A.; Gentil-Baron, P.; Yokoyama, Y.; Takahashi, A. *J. Am. Coll. Cardiol.* **2005**, *46*, 327.

(11)   Cappato, R.; Calkins, H.; Chen, S. A.; Davies, W.; Iesaka, Y.; Kalman, J.; Kim, Y. H.; Klein, G.; Packer, D.; Skanes, A. *Circulation* **2005**, *111*, 1100.

(12)   Pappone, C.; Oral, H.; Santinelli, V.; Vicedomini, G.; Lang, C. C.; Manguso, F.; Torracca, L.; Benussi, S.; Alfieri, O.; Hong, R. *Circulation* **2004**, *109*, 2724.

(13)   Sosa, E.; Scanavacca, M. *J. Cardiovasc. Electrophysiol.* **2005**, *16*, 249.

(14)   Castano, A.; Crawford, T.; Yamazaki, M.; Avula, U. M.; Kalifa, J. *Heart rhythm* **2011**, *8*, 1975.

(15)   Koo Lee, Y. E.; Kopelman, R. *Biomedical Nanoetechnology: Methods and Protocols*; Methods in Molecular Biology Series; Springer: New York, 2011, Vol. *726*, p151.

(16)   Buytaert, E.; Dewaele, M.; Agostinis, P. *Biochim. Biophys. Acta* **2007**, *1776*, 86.

(17)   Hah, H. J.; Kim, G.; Lee, Y. E.; Orringer, D. A.; Sagher, O.; Philbert, M. A.; Kopelman, R. *Macromol. Biosci.* **2011**, *11*, 90.

(18)   Gaumet, M.; Vargas, A.; Gurny, R.; Delie, F. *Eur. J. Pharm. Biopharm.* **2008**, *69*, 1.

(19)   Ward, B.; Bauman, K.; Firth, J. *Cell Tissue Res.* **1988**, *252*, 57.

(20)   Pappano, A. J.; Wier, W. G. In *Cardiovascular Physiology: Mosby Physiology Monograph Series*; 10 ed.; Elsevier Health Sciences: 2012.

(21)   Sarin, H. *J. Angiogenes Res.* **2010**, *2*, 14.

(22)   Veronese, F. M.; Mero, A.; Pasut, G. *Milestones Drug Ther.* **2009**, 11.

(23)   Webster, R.; Elliott, V.; Park, B. K.; Walker, D.; Hankin, M.; Taupin, P. *Milestones Drug Ther.* **2009**, 127.

(24)   Knop, K.; Hoogenboom, R.; Fischer, D.; Schubert, U. S. *Angew. Chem. Int. Ed.* **2010**, *49*, 6288.

(25)   Li, W. J.; Zhan, P.; De Clercq, E.; Lou, H. X.; Liu, X. Y. *Prog. Polym. Sci.* **2013**, *38*, 421.

(26)   Deshmukh, M.; Kutscher, H. L.; Gao, D.; Sunil, V. R.; Malaviya, R.; Vayas, K.; Stein, S.; Laskin, J. D.; Laskin, D. L.; Sinko, P. J. *J. Control. Release* **2012**, *164*, 65.

(27)   Park, J. H.; Moon, Y. H.; Bang, I. S.; Kim, Y. C.; Kim, S. A.; Ahn, S. G.; Yoon, J. H. *Lasers Med. Sci.* **2010**, *25*, 705.

(28)   Park, H.; Na, K. *Biomaterials* **2013**, *34*, 6992.

(29)   Moreno, M. J.; Monson, E.; Reddy, R. G.; Rehemtulla, A.; Ross, B. D.; Philbert, M.; Schneider, R. J.; Kopelman, R. *Sensor Actuat. B-Chem.* **2003**, *90*, 82.

(30)   Kaur, K.; Zarzoso, M.; Ponce-Balbuena, D.; Guerrero-Serna, G.; Hou, L.; Musa, H.; Jalife, J. *PloS one* **2013**, *8*, e55391.

(31)   Bruno, S.; Faggiano, S.; Ronda, L.; Brun, A. *Malvern* **2009**, 1.

(32)   Erickson, H. P. *Biological procedures online* **2009**, *11*, 32.

(33)   Chen, J.; Wasmund, S. L.; Hamdan, M. H. *Pacing Clin. Electrophysiol.* **2006**, *29*, 413.

(34)   Schauerte, P.; Scherlag, B. J.; Pitha, J.; Scherlag, M. A.; Reynolds, D.; Lazzara, R.; Jackman, W. M. *Circulation* **2000**, *102*, 2774.

(35)   Schauerte, P.; Scherlag, B. J.; Patterson, E.; Scherlag, M. A.; Matsudaria, K.; Nakagawa, H.; Lazzara, R.; Jackman, W. M. *J. Cardiovasc. Electr* **2001**, *12*, 592.

(36)   Friedman, P. L.; Stewart, J. R.; Wit, A. L. *Circ. Res.* **1973**, *33*, 612.

CHAPTER 5
CONCLUSIONS & FUTURE DIRECTIONS

5.1 Conclusions

There have been many efforts by scientists in a variety of biomedical fields to develop nanoplatforms for practical biomedical applications. Concerning the first and second highest causes of death (heart and cancer diseases) in the United States, this dissertation presented three different engineered nanomatrixes, aimed at biomedical imaging of cancer and at photodynamic therapy of cancer and of heart arrhythmia.

In Chapter 2, a synthetic method was addressed to prepare human serum albumin (HSA) loaded polyacrylamide (PAA) nanoparticles (NPs) to enhance the stabilization of Indocyanine Green (ICG), which was loaded into NPs through a post-loading modification. The F3 peptide was conjugated onto the NPs with the help of a bi-functional polyethylene glycol (PEG) as a cross-linker. To avoid blockage of the binding site, the bi-functional PEG was conjugated onto the NP surface before the ICG was loaded. The F3 peptide was then conjugated at the other end of bi-functional PEG. Due to the hydrophobic pockets in HSA, which hold the ICG strongly, the degradation rate of ICG was decreased and its thermal- and photo-stability increased compared to ICG in PAA NPs or to free ICG. With regards to the photoacoustic signal, an intense signal was observed at 720 nm, which corresponds to the ICG dimer, because of its lower fluorescence quantum yield (i.e., higher heat production yield) compared to that of the

monomer. In addition, these new protein hybrid PAA NPs showed cell specificity for the 9L glioma cancer cell line, due to the F3 peptide targeting moiety.

In Chapter 3, enhanced reactive oxygen species (ROS) producing Methylene Blue (MB) conjugated PAA NPs and a multiplexed microfluidic device for photodynamic therapy (PDT) analysis were introduced. The long cross-linker, poly(ethylene glycol) dimethacrylate (PEGDMA, $M_n = 550$), was used to increase the distance between the conjugated MB groups; it also provided high oxygen permeability. The MB–PEGDMA PAA NPs advantages are expressed in higher ROS production rate than previously reported NPs, in protecting the loaded MB from bio-enzymes and in keeping the spectral shape of MB consistent at varied sample concentrations. During PDT, the relative total ROS production (k value) and the relative singlet oxygen generation (S value) of MB– PEGDMA PAA NPs with varied MB loading were detected using 9,10-dipropionic acid disodium salt (ADPA) and Singlet Oxygen Sensor Green (SOSG) dyes, respectively. The different trend of the k and S values originates from two distinct ROS producing routes of MB: the MB monomer produces singlet oxygen, whereas the MB dimer produces superoxide. The specially designed microfluidic chip, optimized for *in vitro* PDT efficacy tests, enabled simultaneous multiple measurements on different NP samples. This new microfluidic device helped not only to decrease the experiment time, the required sample amount and the cost, but also allowed a more accurate comparison of PDT efficacy between different photo-drug samples.

In Chapter 4, a selective cardiac ablation for heart arrhythmia was achieved by a cardiac targeting peptide (CTP) targeted Chlorin e6 (Ce6) conjugated 8-arm PEG (Ce6– PEG) nanoplatform. The photosensitizer, Ce6, was conjugated onto an 8–arm PEG

polymeric nanoplatform instead of PAA NPs due to the size limitation of heart tissue fenestrations (pores). During *in vitro* PDT, only myocytes, but not fibroblasts, were killed under the co-cultured condition. In contrast to the PAA NPs, the CTP–Ce6–PEG nanoplatforms are able to penetrate into the endothelial structure of heart, *in vivo*. Thus, in the histology test, the fluorescence of Ce6 was observed from myocyte cells, but not from fibroblast cells. During the *in vivo* PDT test, the left atrial appendage (LAA) electrogram of the local signal amplitude decreased by about 83% for CTP–Ce6–PEG and its targeting ability, after *in vivo* PDT treatment, was also confirmed by histology.

In conclusion, all of these nanomatrices were designed to satisfy the basic requirements of a successful nanomatrix as described in Chapter 1; each was synthesized and engineered with its own advantages, as nanocarriers for multifunctional optical imaging and PDT of cancer, or for photo-ablation of cardiac arrhythmia by PDT.

5.2 Future Directions

In the next decades, heart and cancer diseases stand to benefit from the development of nanotechnology research. Our studies in this thesis demonstrated that PAA NPs and PEG nanoplatforms are promising delivery carriers for contrast agents of biomedical imaging and photo-drugs of PDT. Although these nanoplatforms consist of biocompatible and non-toxic materials, with facile fabrication, they have still a long way to go before they are ready for clinical and industrial applications. In here, a simple direction of strategy to achieve this final goal will be suggested with perspectives.

5.2.1 *In Vivo* Toxicity Tests of Nanoplatforms

The introduced nanoplatforms, PAA NPs and 8-arm PEG, were claimed as biocompatible and non-toxic materials for biomedical applications. For the PAA NPs, an *in vitro* toxicity test was given through CCK-8 assays in Chapter 2; the test was reported to demonstrate its non-toxicity towards several cell lines. Since the changing of chemical structure can cause toxicity to material, the toxicity of modified NPs was also tested after albumin conjugation or dye loading. However, a cellular level toxicity test spanning only $1 - 3$ days is not enough for justifying the safety of the application of such nanomaterials at the clinical level. Although PAA NPs were classified as bio-degradable NPs, due to the ester groups in their cross-linkers, a study reports that, under treatment with 1M NaOH, it took 1000 h to decrease the size of these NPs from 39.4 nm to less than 5 nm. [1] Since most of our body is around pH 7.4, the actual required time for degradation of NPs might be much longer, *i.e.*, most of the PAA NPs may stay in our body for a long time without excretion. [2,3] Furthermore, the extremely small sized nanoplatform could penetrate practically anywhere in the human body, not only into the targeted area; this unwanted wide distribution of the nano-drug could lead to unexpected side effects. [4] To prevent such *in vivo* cytotoxicity, it would be needed to perform further research on the above nanoplatforms through animal testing. After adding various doses of nanoplatforms to an animal, its weight and health status can be checked over the course of several weeks. Then, each organ and tissue of the tested animal has to be analyzed for the amount of residual nanoplatforms, with confirmation of any injury to each organ. Based on the bio-distribution, the nanoplatforms can be applied to various diseases of each organ, and the degradation rate of the nanoplatforms under the specific condition in each organ can be

modified by the design of the biodegradable polymer or its cross-linker, towards fast excretion, which is one of the important factors in removing toxicity. [5] Also, the same test should be applied to large animals, such as pigs, monkeys or sheep. Such long term *in vivo* toxicity tests of nanoplatforms are needed for FDA approval of human clinical trials. Such tests would accelerate the commercialization of the PAA NPs or 8-arm PEG nanoplatforms.

5.2.2 Multifunctional (Theranostic) Modification of Nanoplatform

In Chapter 2, multimodal (photoacoustic and fluorescence) imaging techniques were successfully demonstrated from available ICG loaded NPs. With further development a superior nanoplatform would enable not only the detection of cancer but also treatment of cancer at the same time. It is already known that HSA is used as a delivery tool for chemo-drugs, like doxorubicin, dexamethasone, methimazole and paclitaxel. [6-9] To deliver these chemo-drugs, HSA–PAA NPs can be applied to deliver both imaging contrast agent (ICG) and chemo-drugs, simultaneously. To optimize the loading of dyes, the optimal amount of HSA should be investigated first, by varying the amount of conjugated HSA. Although more HSA might help to load more dyes it also results in increasing the size of the NPs, which is limiting in certain therapeutic condition.

Our group has also studied tumor delineation using Coomassie Blue (CB) loaded PAA NPs. [10,11] During brain cancer surgery, it is very important to visualize the tumor margins and, accordingly, covalently linked CB has been targeted to the tumor by using NPs with the aim of aiding the surgeon's performance. Instead of CB–PAA NPs, which are only useful for delineation, MB–PAA NPs could be applied to both tumor delineation and PDT. In Chapter 3, it was demonstrated that a high amount of MB loading into

PEGDMA PAA NPs results in a very high absorbance and also in a relatively high ROS productivity due to superoxide production. From these results, tumor targeted MB–PAA NPs can be utilized to delineate the tumor boundaries (during surgery), *i.e.*, to visually monitor the blue "painted" tumor due to the accumulation of these blue NPs, when targeted specifically to the tumor cells, and then, only the blue colored area can be treated by PDT to kill the tumor cells. [10-12] Furthermore, the same MB loaded NPs can also be used as sonophoric contrast agents for obtaining the 3-dimensional structure of the "blue" tumor by photoacoustic imaging, as demonstrated previously with CB–PAA NPs. [10] Additionally, these NPs could also serve as nano-regulators by mimicking ROS production during cellular metabolism. The highly localized ROS produced by these NPs could also be used to modulate intracellular signaling pathways, enabling refined and novel methods of cellular research. [13,14] Such "theranostic" modification of the nanoparticles will enable the realization of "multifunctionality" in the true sense of the word, so that several biomedical applications, based on chemotherapy, fluorescence, photoacoustic imaging, visual delineation and PDT will be carried out with a single kind of nanoplatform. This theranostic nanoplatform could be a solution towards decreasing the operational time of imaging and surgery.

5.2.3 Fast Degrading Photosensitizer for Selective Cardiac Ablation.

In Chapter 4, a novel photo-drug (CTP–Ce6–PEG) successfully ablated myocyte cells, both *in vitro* and *in vivo*. However, from the bioluminescence test on CTP–Ce6–PEG in rats, it was found that nanoplatforms accumulated in every organ, including the heart, lung, liver, pancreas, muscle, kidney and skin, (Figure 5-1). While photosensitizer embedded nanoplatforms are chemically non-toxic under dark conditions, they can cause

serious side effects ("sun burns") when accumulated in the skin, and especially in the eyes due to sunlight. The Ce6 is a hydrophobic photosensitizer and known to have pretty high stability in water (slow degradation). Instead of Ce6, MB could be the alternative answer for the photosensitizer. Though MB has a short half-life in the human body due to fast renal excretion and plasma enzyme enhanced reduction/isomerization (turning to leuko MB), conjugating with the bulky 8-arm PEG (40 kDa) could increase the circulation time in the plasma due to prevention of fast renal excretion and enhancement of the MB chemical stability. [15-17] However, the size of the 8-arm PEG (40kDa) is below the upper limit for kidney excretion and the 8-arm PEG cannot protect the MB perfectly from bio-enzymes, in contrast to PAA NPs which 3-dimensionally encapsulate MB. [16] Thus the MB–8-arm PEG may be excreted or reduced to its lueko-MB form, within time periods of appropriate length. Last, so as not to be limited to rats, the *in vivo* study of these new photo-drugs, CTP–Ce6–PEG or CTP–MB–PEG, on larger animals (rabbits or sheep), will be investigated towards human clinical trials. Thus, the heart arrhythmia patient can get treatment with minimal side effects and risk related to the catheter ablation technique, through the use of a highly myocyte selective ablation PDT. Furthermore, based on this, this 8-arm PEG based photo-drug for PDT may be applicable to diseases other than just cardiac arrhythmia.
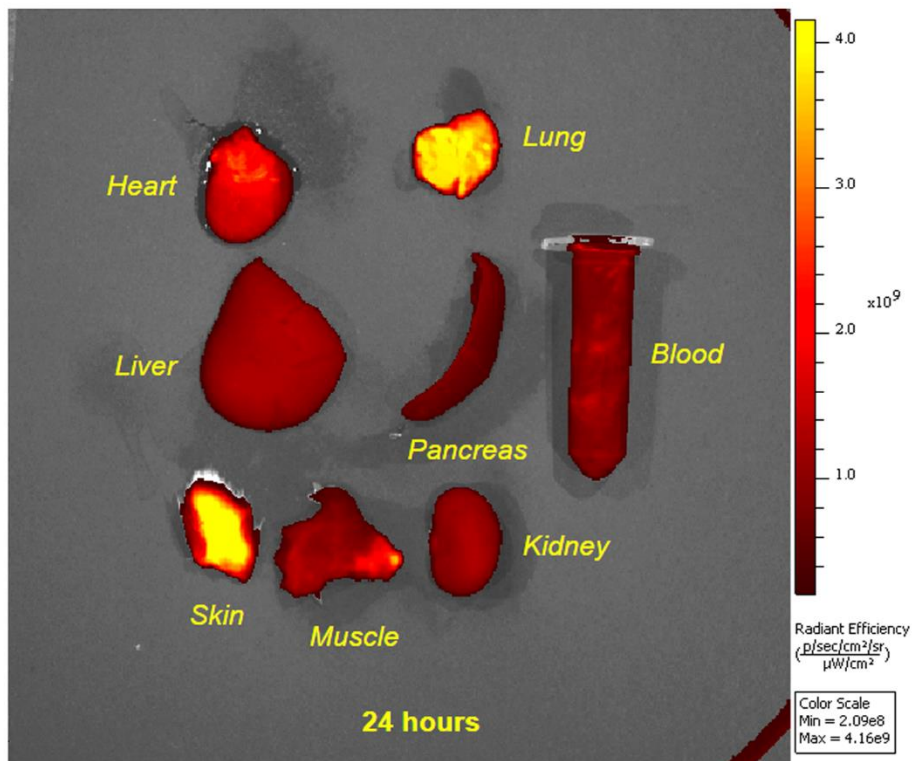
Figure 5-1 *Ex vivo* fluorescence image of each of several organs, from a bioluminescence study. Each organ was excised from a rat, at 24 h post injection of 100 mg of CTP–Ce6–PEG. The fluorescence images were obtained by an IVIS system (λ_{ex} = 640 nm and λ_{em} = 680 nm).

5.3 References

(1)   Wang, S.; Kim, G.; Lee, Y. E.; Hah, H. J.; Ethirajan, M.; Pandey, R. K.; Kopelman, R. *ACS Nano* **2012**, *6*, 6843.

(2)   Koo Lee, Y. E.; Reddy, G. R.; Bhojani, M.; Schneider, R.; Philbert, M. A.; Rehemtulla, A.; Ross, B. D.; Kopelman, R. *Adv. Drug Deliv. Rev.* **2006**, *58*, 1556.

(3)   Wenger, Y.; Schneider, R. J., 2nd; Reddy, G. R.; Kopelman, R.; Jolliet, O.; Philbert, M. A. *Toxicol. Appl. Pharm.* **2011**, *251*, 181.

(4)   Gaumet, M.; Vargas, A.; Gurny, R.; Delie, F. *Eur. J. Pharm. Biopharm.* **2008**, *69*, 1.

(5)   Larson, N.; Ghandehari, H. *Chem. Mater.* **2012**, *24*, 840.

(6)   Bae, S.; Ma, K.; Kim, T. H.; Lee, E. S.; Oh, K. T.; Park, E. S.; Lee, K. C.; Youn, Y. S. *Biomaterials* **2012**, *33*, 1536.

(7)   Naik, P. N.; Chimatadar, S. A.; Nandibewoor, S. T. *J. Photochem. Photobiol. Biology* **2010**, *100*, 147.

(8)   Sułkowska, A. *J. Mol. Struct.* **2002**, *614*, 227.

(9)   Trynda-Lemiesz, L. *Bioorgan. Med. Chem.* **2004**, *12*, 3269.

(10)   Ray, A.; Wang, X. D.; Lee, Y. E. K.; Hah, H. J.; Kim, G.; Chen, T.; Orringer, D. A.; Sagher, O.; Liu, X. J.; Kopelman, R. *Nano Res.* **2011**, *4*, 1163.

(11)   Nie, G.; Hah, H. J.; Kim, G.; Lee, Y. E.; Qin, M.; Ratani, T. S.; Fotiadis, P.; Miller, A.; Kochi, A.; Gao, D.; Chen, T.; Orringer, D. A.; Sagher, O.; Philbert, M. A.; Kopelman, R. *Small* **2012**, *8*, 884.

(12)   Orringer, D. A.; Koo, Y. E.; Chen, T.; Kim, G.; Hah, H. J.; Xu, H.; Wang, S.; Keep, R.; Philbert, M. A.; Kopelman, R.; Sagher, O. *Neurosurgery* **2009**, *64*, 965.

(13)   Finkel, T. *J. Cell Biol.* **2011**, *194*, 7.

(14)   D'Autreaux, B.; Toledano, M. B. *Nat. Rev. Mol. Cell Biol.* **2007**, *8*, 813.

(15)   Veronese, F. M.; Mero, A.; Pasut, G. *Milestones Drug Ther.* **2009**, 11.

(16)   Knop, K.; Hoogenboom, R.; Fischer, D.; Schubert, U. S. *Angew. Chem. Int. Ed.* **2010**, *49*, 6288.

(17)   Li, W. J.; Zhan, P.; De Clercq, E.; Lou, H. X.; Liu, X. Y. *Prog. Polym. Sci.* **2013**, *38*, 421.